Chair of Applied Geophysics

Master's Thesis

Geophysical ore prospection at Straßegg (Breitenau, Styria)

Stefan Biedermann, BSc

September 2023

MONTANUNIVERSITÄT LEOBEN
www.unileoben.ac.at

EIDESSTATTLICHE ERKLÄRUNG

Ich erkläre an Eides statt, dass ich diese Arbeit selbständig verfasst, andere als die angegebenen Quellen und Hilfsmittel nicht benutzt, und mich auch sonst keiner unerlaubten Hilfsmittel bedient habe.

Ich erkläre, dass ich die Richtlinien des Senats der Montanuniversität Leoben zu "Gute wissenschaftliche Praxis" gelesen, verstanden und befolgt habe.

Weiters erkläre ich, dass die elektronische und gedruckte Version der eingereichten wissenschaftlichen Abschlussarbeit formal und inhaltlich identisch sind.

Datum 13.09.2023

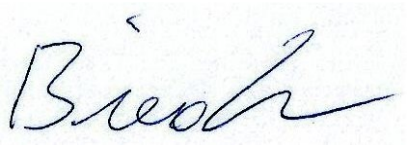

Unterschrift Verfasser/in

Stefan Biedermann

Kurzfassung (German)

Angesichts des wachsenden Bedarfs an Rohstoffen ist es notwendig, kontinuierlich neue Mineralvorkommen zu erschließen. Dies ist mit hohem Zeitaufwand als auch mit hohen Kosten verbunden und geht zum Teil mit einer großen Umweltbelastung einher. Alternative Möglichkeiten zur Deckung des Rohstoffbedarfs gewinnen daher zunehmend an Bedeutung. Beispielsweise können bereits bekannte Vorkommen, welche sich in der Vergangenheit als nicht mehr rentabel erwiesen, mithilfe moderner Technologien erneut auf ihre Eignung als Lagerstätte hin untersucht werden. Eine solche erneute Beurteilung wurde im Bergbaurevier Straßegg in der Nähe von Breitenau am Hochlantsch durchgeführt.

Vom 15. bis zum 19. Jahrhundert wurden dort goldhaltiger Arsenopyrit, Bleiglanz und Pyrit abgebaut, wobei sich der Schwerpunkt der bergbaulichen Tätigkeiten auf den Zuckenhutgraben nördlich von Straßegg beschränkte. Mittels zerstörungsfreier geophysikalischer Methoden wurde die Umgebung des Pramerkogels, einer Fläche von etwa 1 km², auf eine mögliche Fortsetzung der goldführenden Arsenopyrit Vererzung nach Süden und mögliche weitere Vererzungen, welche in Zusammenhang mit Arsenopyrit stehen, untersucht. Weiters sollen diese Untersuchungen Aufschluss über mögliche andere Vererzungstypen geben, um das volle Potential dieses Vorkommens nutzen zu können.

Basierend auf den flächenmäßig angewendeten Verfahren der Geomagnetik und der Eigenpotentialmessungen wurden zwei Teilprofile ausgewählt, welche durch die Anwendung der Geoelektrik näher untersucht wurden. Darüber hinaus wurden paläomagnetische Messungen an Gesteinsproben durchgeführt, um die darin enthaltenen magnetischen Minerale bestimmen zu können. Für die Interpretation der geophysikalischen Anomalien werden einerseits bereits vorhandene geochemische und aeromagnetische Daten und andererseits die Ergebnisse eines Prospektionsprogramms der Firma MINREX verwendet.

Durch den Vergleich der erhobenen geophysikalischen Daten konnten mehrere Anomaliegruppen bestimmt werden, welche sich anhand der physikalischen Eigenschaften voneinander abgrenzen. Die magnetischen Anomalien können hauptsächlich dem im Gestein enthaltenen Pyrrhotin, untergeordnet auch Hämatit und Maghemit, zugeschrieben werden. Durch eine vergleichende Darstellung mit den Ergebnissen aus der Geoelektrik und des Eigenpotentials können dem Pyrrhotin erhöhte Werte der Polarisierbarkeit, spezifische Widerstände bis 400 Ωm sowie Potentiale von bis zu -500 mV zugeschrieben werden. Weiters wurden Unterschiede im Auftreten des Pyrrhotins festgestellt. Neben Kluftvererzungen werden auch stratiforme Einlagerungen angeführt. Das Auftreten von Eigenpotentialanomalien wird neben Pyrrhotin auch mit Grafit und Pyrit in Verbindung gebracht. Vor allem im westlichen Teil des Gebietes werden große Potenzialabfälle von etwa 1000 mV gemessen, welche auf Grafitlinsen zurückgeführt werden. Diese lassen sich auch durch die niedrigen spezifischen Widerstände von unter 10 Ωm und die hohen Werte der Polarisierbarkeit mit Phasenwinkeln von bis zu 70 mrad belegen. Im Osten des Untersuchungsgebietes können mehrere unmagnetische sulfidische Vererzungen lokalisiert werden.

Diese zeigen ähnliche Polarisierbarkeiten wie die Grafitlinsen, unterscheiden sich jedoch durch höhere spezifische Widerstände von bis zu 250 Ωm und generell kleineren Potentialabfällen. Vereinzelt können im Zusammenhang mit diesen Vererzungen Potentialabfälle bis 500 mV und spezifische Widerstände von 10 Ωm auftreten. Dies wird mit Einlagerungen von Grafit erklärt. Anhand der Geoelektrik werden diese Vererzungen als steilstehend interpretiert. Durch den Vergleich mit der in der Literatur beschriebenen Hauptvererzung des goldführenden Arsenopyrit nahe der Formationsgrenze wird ein Zusammenhang mit einer der lokalisierten sulfidischen Vererzungen hergestellt.

Abstract

Due to the growing demand for raw materials, it is necessary to continuously explore new mineral deposits. This is time-consuming and expensive, and in some cases also has a major impact on the environment. Alternative ways of meeting the demand for raw materials are therefore becoming increasingly important. For example, known deposits that proved to be no longer profitable in the past can be reassessed for their suitability as deposits with the aid of modern technologies. Such a reassessment was carried out in the Straßegg mining district near Breitenau am Hochlantsch.

From the 15th to the 19th century, gold-bearing arsenopyrite, galena and pyrite were mined with the focus of the mining activities being restricted to the Zuckenhutgraben north of Straßegg. Using non-destructive geophysical methods, an area of about 1 km² surrounding the Pramerkogel was investigated for a possible continuation of the gold-bearing arsenopyrite mineralization to the south and possible further mineralizations related to arsenopyrite. Furthermore, these investigations should provide information on possible other mineralization types to be able to use the full potential of this deposit.

Based on the areal applied methods of geomagnetics and self-potential measurements, two sub-profiles were selected, which were investigated in more detail by the application of geoelectrics. In addition, paleomagnetic measurements were performed on rock samples to determine the magnetic minerals contained therein. For the interpretation of the geophysical anomalies on the one hand already existing geochemical and aeromagnetic data and on the other hand the results of a prospecting program of the company MINREX are used.

By comparing the collected geophysical data, several anomaly groups could be determined, which can be distinguished from each other based on their physical properties. The magnetic anomalies can be attributed mainly to the pyrrhotite contained in the rock, subordinately also to hematite and maghemite. By a comparative presentation with the results from geoelectrics and the self-potential, increased values of polarizability, specific resistivities up to 400 Ωm and potentials up to -500 mV can be attributed to pyrrhotite. Furthermore, differences in the occurrence of pyrrhotite were found. In addition to vein mineralization, stratiform intercalations are also recognized. The occurrence of self-potential anomalies is, besides pyrrhotite, associated with graphite and pyrite. Large potential drops of about 1000 mV were measured in the western part of the area, which are attributed to graphite lenses. These can also be evidenced by the low resistivity values of lower than 10 Ωm and the high values of polarizability with phase angles of up to 70 mrad. Several non-magnetic sulfidic mineralizations can be located in the east of the survey area. These show similar polarizabilities to the graphite lenses but differ in higher resistivities of up to 250 Ωm and generally smaller potential drops. Potential drops of up to 500 mV and resistivity values of 10 Ωm can occur in association with these mineralizations. This is explained by intercalations of graphite. Based on geoelectrics, these mineralizations are interpreted as steeply inclined. By comparison with the main mineralization of the gold-bearing arsenopyrite near the formation boundary described in the literature, a relation with one of the localized sulfidic mineralizations is established.

Danksagung

An dieser Stelle möchte ich mich bei all jenen bedanken, die mich während der Anfertigung dieser Arbeit und auch während des gesamten Studiums unterstützt haben.

Besonders gilt mein Dank meinem Betreuer Ao. Univ.-Prof. Dr.phil Robert Scholger, welcher mich sowohl bei den Feldmessungen als auch bei der Auswertung betreut hat. Für die hilfreichen Anregungen und die konstruktive Kritik bei der Erstellung dieser Arbeit bedanke ich mich ebenso.

Weiters möchte ich mich bei Herrn Thomas Brunner für die Möglichkeit bedanken, diese interessante Masterarbeit anfertigen zu dürfen. Außerdem bedanke ich mich aber auch für seine tatkräftige Unterstützung während den Feldmessungen und die vielen absolvierten Höhenmeter.

Bei Frau Christiane Pretzenbacher möchte ich mich bedanken für die Unterstützung während meines gesamten Studiums. Nur durch sie konnte ich viele organisatorische Hürden überwinden.

Weiters möchte ich meiner Freundin Franziska dafür danken, dass sie mich immer unterstützt und motiviert hat.

Mein besonderer Dank gilt meiner Familie, die mich im Lauf meines Studiums in jeder Hinsicht unterstützt hat.

Abschließend möchte ich mich auch bei meinen Studienkollegen allen voran Daniel, Alex, Mutsch und David für die unvergessliche Zeit in Leoben bedanken.

Table of content

1 Introduction

The aim of this work is to apply geophysical methods for the prospection of possible mineralizations in the former mining district of Straßegg, which is located 34 km north-east of Leoben (Figure 1) at an elevation between 900 and 1200 m. a. s. l. Geologically, the area of Straßegg lies in the Paleozoic of Graz, more precisely in the Schöckel nappe system. Gold bearing arsenopyrite, pyrite and galena were mainly mined between the 15th and 19th century. While the northern area of Straßegg is already quite well known because of the numerous small mines, in the southern area not much information about mineralizations is available. Therefore, this project is more focused on the south around the Pramerkogel. In close cooperation with Mr. Thomas Brunner, CEO of Aurex Biomining AG, geomagnetic, self-potential and geoelectric data was collected in the field during September 2022 and March 2023. In addition, samples were taken for paleomagnetic analysis. In total sixteen geomagnetic and eight self-potential profiles with an average length of about 1.1 km were measured. Based on this data, the location of two geoelectric profiles were chosen. By comparing the processed results of the different applied geophysical methods and in addition also geochemical data, a deeper understanding about mineralizations of the area should be gained.

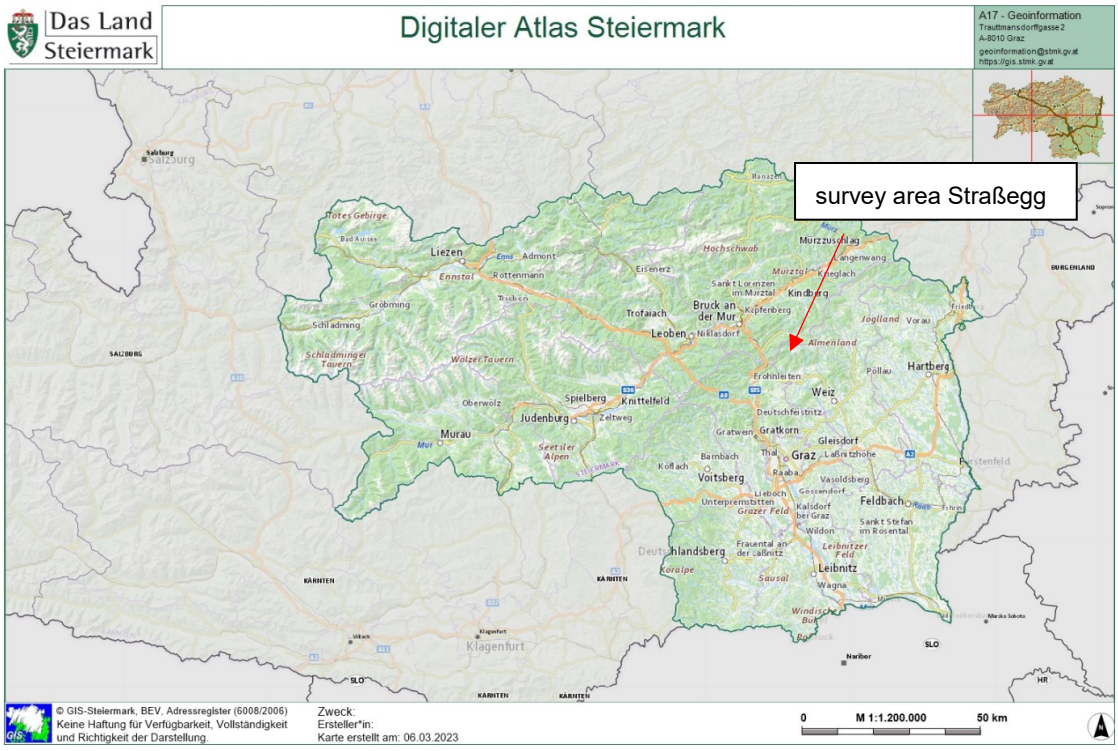

Figure 1: Geographical overview of the survey area (GIS Steiermark, 2023).

2 Geological overview

2.1 Paleozoic of Graz

The Paleozoic of Graz is a 30 x 50 km sized nappe complex and consists mainly of low-grade metamorphosed sediments and metavolcanic rocks of late Silurian to Carboniferous age (Figure 2). Together with other Paleozoic sedimentary units, it builds up large parts of the upper Austroalpine units of the Eastern Alps (Bojar et al., 2001; Gasser et al., 2010). It is confined by higher grade metamorphosed units, including the Koralm Crystalline to the west and the Gleinalm complex to the north-west, which are representing the middle Austroalpine units. The Strahlegg Crystalline restricts the Paleozoic of Graz to the north-east and belongs to the lower Austroalpine units. In the south, it is overlain by Tertiary sediments of the Styrian Basin (Bojar et al., 2001; Ebner et al., 2001). To the south-west the Kainacher Gosau is discordant and transgressive overlaying the Paleozoic of Graz (Ebner & Rantitsch, 2000). In the Paleozoic of Graz five sedimentary facies associations, namely the Rannach, Hochlantsch, Laufnitzdorf, Kalkschiefer and Schöckel facies, are present. Each facies is assigned to one tectonic nappe and, due to similarities in tectonic position and metamorphic overprint, they form three nappe systems (Fritz & Neubauer, 1988; Gasser et al., 2010). The Schöckel nappe system represents the lowest one. The intermediate nappe system comprises of the Kalkschiefer and Laufnitzdorf nappes. The uppermost nappe system is built up by the Rannach and the Hochlantsch nappe (Ebner et al, 2000; Fritz et al.,1992; Krenn et al., 2007;). Figure 2b shows the internal structure and the surrounding tectonic units of the Paleozoic of Graz. The main formations in each nappe and the corresponding age can be found in Figure 3.

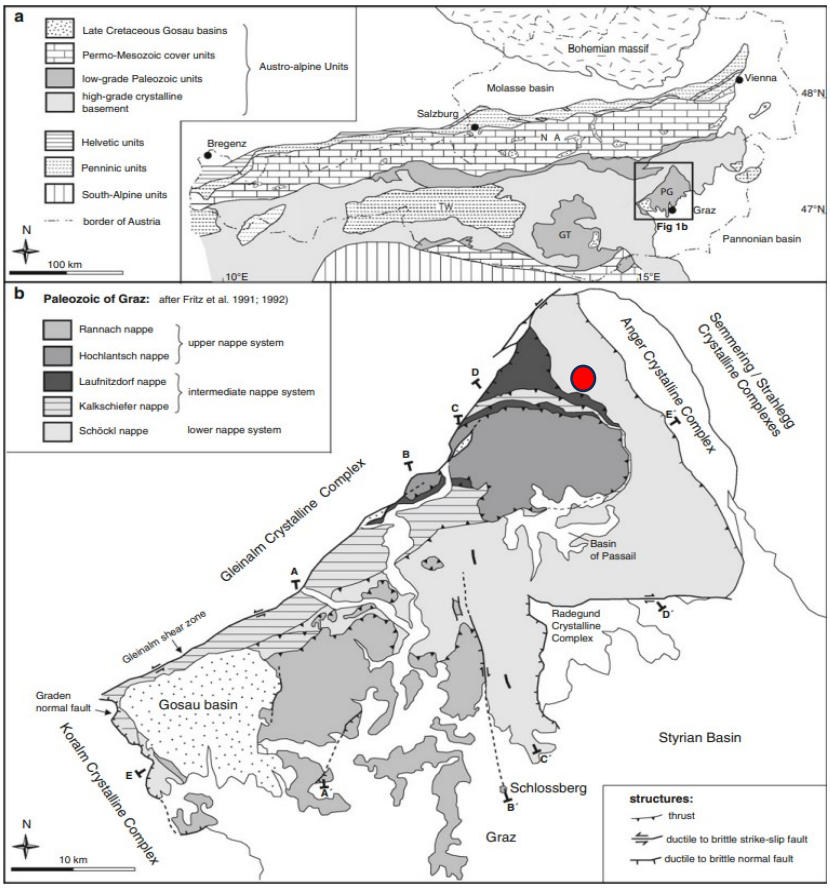

Figure 2: a) Geological overview of the tectonic units of the Eastern Alps. b) Geological overview of the Paleozoic of Graz after Gasser et al. (2010). The red dot is marking the location of the survey area.

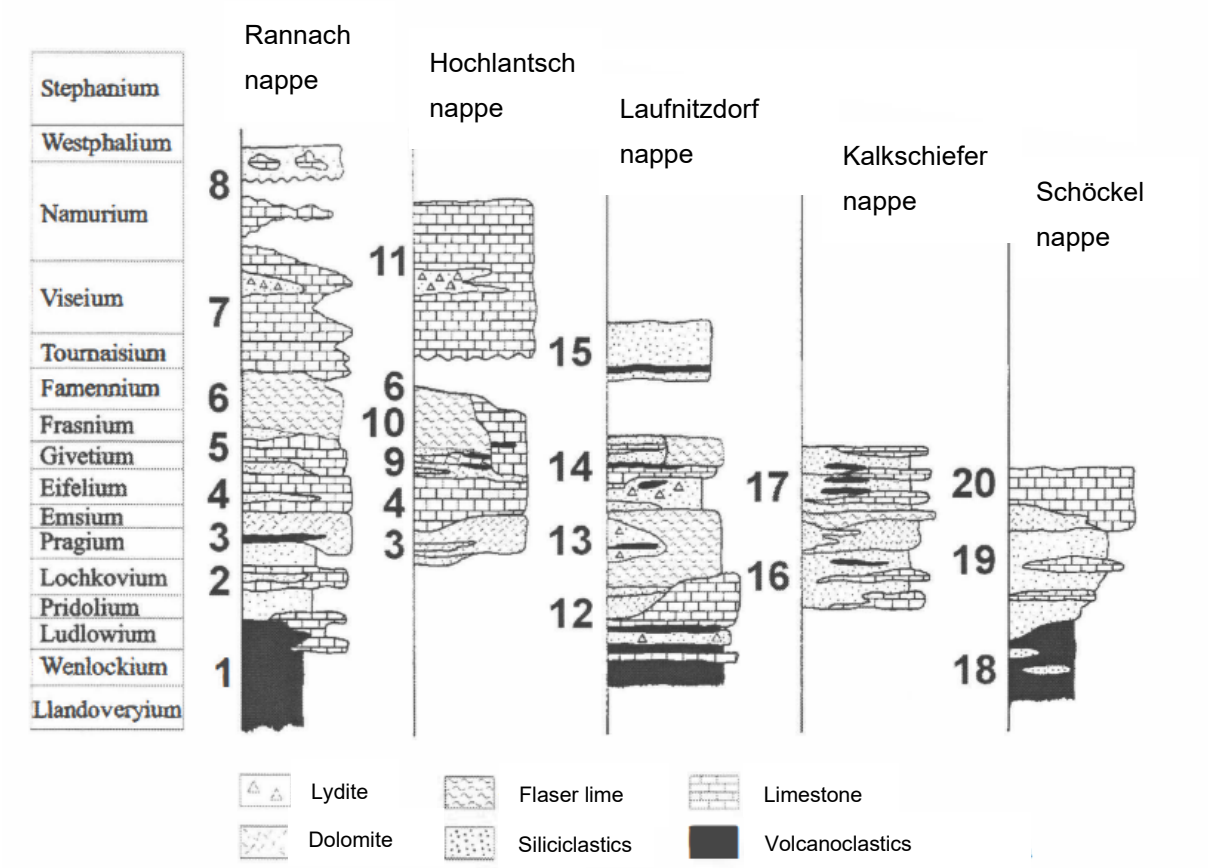

Figure 3: Stratigraphic overview of the nappes in the Paleozoic of Graz. 1.Kehr-Formation, Kötschberg-Formation; 2.Parmasegg-Formation; 3.Flösserkogel-Formation, Bameder-Formation; 4.Barrandei limestone; 5.Kollerkogel-Formation; 6.Steinberg-Formation; 7.Sanzenkogel-Formation; 8.Höchkogel-Formation, Hahngraben-Formation; 9.Tyrnaueralm-Formation; 10.Zachenspitz-Formation, Hochlantsch-Formation; 11.Bärenschütz-Formation; 12.Hackensteiner-Formation; 13 Harrberger-Formation; 14.St.Jakob-Formation; 15.Donerkogel-Formation; 16.Kogler-Formation; 17.Hubenhalt-Formation; 18.Taschen-Formation; 19.Schönberg-Formation; 20.Schöckel-Formation, Hochschlag-Formation. Modified after Ebner et al. (2000).

After Gasser et al. (2010), the Paleozoic of Graz can be subdivided, not according to the classical facies concept into three nappe systems, but rather in two systems. In this formulation, the lower system consists of the Schöckel facies, the Kalkschiefer and the Laufnitzdorf facies. Rannach and Hochlantsch facies belong therefore to the upper nappe system which is separated by the Rannach thrust from the lower system. This division should simplify the differentiation of sedimentary and tectonic units.

2.1.1 Geodynamics, tectonics and metamorphism

The Paleozoic of Graz reflects the development of a passive continental margin, from a rifting stadium with intracontinental volcanism in Silurian to a progressive carbonate production due to decreasing subsidence in the early Devonian (Fritz & Neubauer, 1988). The basal low alkaline volcaniclastics are defined as products of the intracontinental volcanism, which is related to extension and an initial rift stadium in Silurian (Ebner et al., 2001). Until the lower Devonian, fine grained siliciclastics and carbonates are sedimented in basins with varying water depths, where an enhancement of the carbonate production can be seen in the Devonian.

This is most likely related to a heating phase due to the equatorial position of the Paleozoic of Graz (Ebner et al., 2000; Fritz & Neubauer, 1988). From the upper middle Devonian on, a pelagic distal sedimentation took place, which is related to a sea level rise (Hubmann, 1993). In the late Devonian and early Carboniferous, erosion and carstification occurred (Gasser et al., 2010). Paleo-geographically, Rannach and Hochlantsch facies are in a proximal position and the Laufnitzdorf facies is the most distal one. Schöckel and Kalkschiefer facies are in an intermediate position (Fritz et al., 1992). The age of the internal deformation of the Paleozoic of Graz is still under discussion. Both, variscian and eo-alpine events, could influence the internal structure (Gasser et al., 2010), where only in the Schöckel nappe evidence for a variscian deformation can be seen (Ebner et al., 2001). The nappe stacking itself is, after Ebner (2001), lower Cretaceous in age. In the upper Cretaceous, the uplift of the Gleinalm complex leads to extension and the development of basins. As a result of the extension and uplift, the Paleozoic of Graz gets separated from the crystalline basement (Ebner et al., 2001). Furthermore, the borders of the Paleozoic of Graz got deformed due to the exhumation (Gasser et al., 2010). In the nappes, a clear increase of metamorphism can be seen from west to east and from the hanging to the foot wall (Hasenhüttl & Russegger, 1992), where in the Schöckel nappe system metamorphism grades up to amphibolite facies are possible (Neubauer, 1981). In the eastern lower nappes, indications for a variscian metamorphism are present (Ebner et al., 2001). Therefore, a two-stage metamorphism, variscian and alpidic, is discussed for the Paleozoic of Graz.

2.2 Geology of the survey area

In the area of Straßegg only the Schöckel nappe system is present, which is dominated by greenschist facies volcanic and siliciclastic rocks. The age can be assigned to the late Silurian and early Devonian, whereby carbonate platform sediments show a middle Devonian age (Krenn et al., 2007). The deformation in the nappe system is high, compared to the upper nappe systems, and the overfold construction style complex (Ebner et al., 2001; Gasser et al., 2010). A penetrative foliation with a pronounced and asymmetric east to west stretching can be seen in the rocks (Gasser et al., 2010). The nappe system is divided into the Peggau and the Passail group (Flügel & Hubmann, 2000). Both groups can be found in the area, where the main formations, from the foot wall to the hanging wall, are the Heilbrunner phyllite formation, the Schönberg formation and the Hochschlag formation. The Pramerkogel complex can be seen as part of the Heilbrunner phyllite formation (Figure 4). A summary of the formations and the associated mineralogy can be found in Table 1.

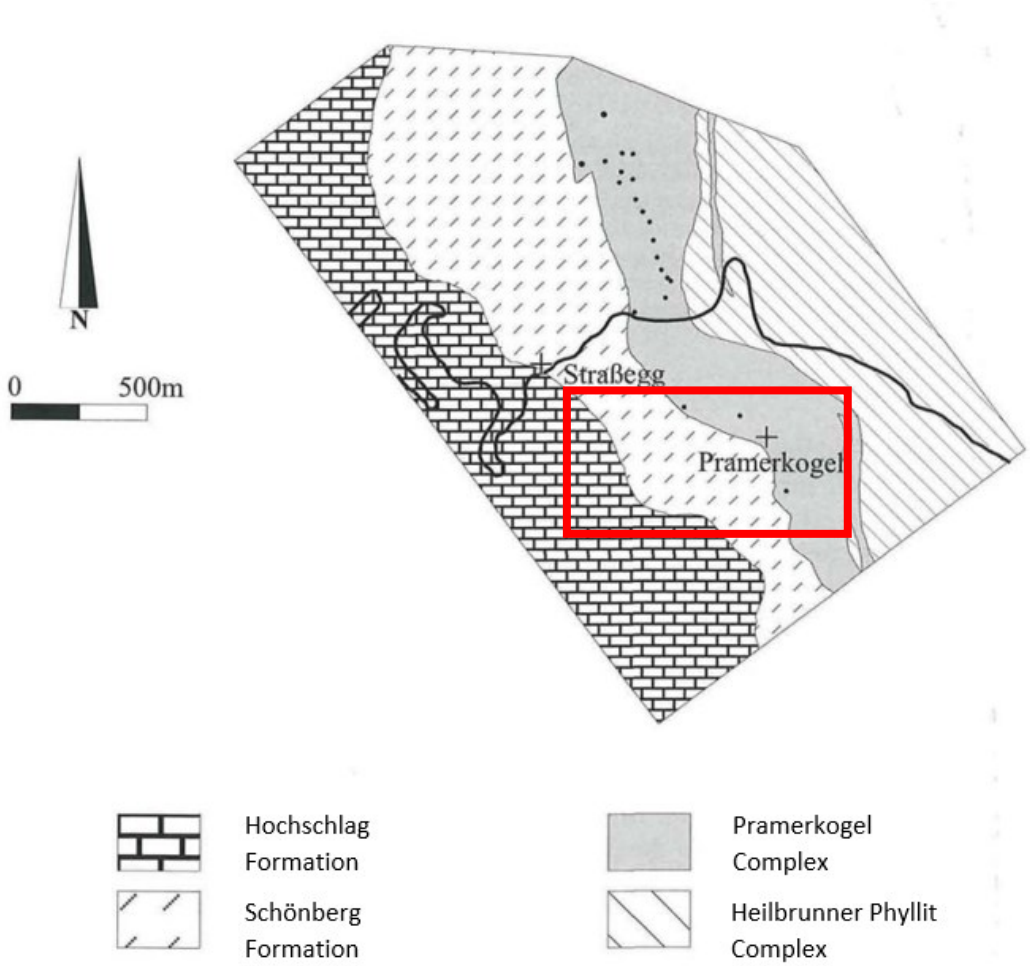

Figure 4: Geological formations around Straßegg. The red rectangle represents the survey area and the black dots indicate former mining activities. Modified after Bojar et al. (1998).

2.2.1 Passail group

For the Passail group, which could be pre-Devonian in age, prevailing rocks are sericite phyllites with intercalations of chlorite schists. The group can be lithologically further divided into three main formations with a total thickness of a few hundred meters. (Ebner et al., 2001). In the survey area one main formation, namely the Heilbrunner phyllite formation, is present.

Heilbrunner phyllite formation

After Gsellmann (1987), the formation in Straßegg can be subdivided into two different complexes. The Heilbrunner phyllite complex and the hanging Pramerkogel complex. The first mentioned complex is dominated by quartz phyllites, garnet-biotite phyllites and epidote-chlorite schists (Antes, 1998; Gsellmann, 1987). The Pramerkogel complex comprises of metavolcanites. Albite-biotite-chlorite phyllites and garnet-biotite-chlorite phyllites associations prevail, where the protoliths are tuffs and basaltic effusiva (Antes, 1998; Bojar et al, 2001). The formation overlays the Crystallin of Birkfeld. In this complex, arsenopyrite mineralizations can be found.

2.2.2 Peggau group

The lower units of the Paleozoic of Graz are mostly described through the Peggau group, which shows a thickness of more than 1000 m. It can be further divided into three lithostratigraphic units. In the foot wall position, a volcanogenic evolution can be seen followed by an euxinic and a carbonate evolution (Flügel & Hubmann, 2000). The evidence of a volcanogenic evolution can be seen through the occurrence of alkaline metavolcanites, like greenschists and metabasalts. Black shales and carbonates represent the middle euxenic volcanogenic evolution (Ebner et al., 2001). The Peggau group is divided into six formations. In the locality of Straßegg, the Hochschlag and the Schönberg formations are present.

Schönberg formation

The Schönberg formation is represented through the Weitzbauer member, where black shales are prevailing. Intercalations with dark limestones and lydites are common, which are rich in graphite, organics and pyrite. The formation is Devonian in age and has a thickness of about 200 to 300 meters (Bojar et al., 2001; Flügel & Hubmann, 2000).

Hochschlag formation

The Hochschlag formation overlays the Weitzbauer member and consists mainly of carbonates with thin intercalations of black shales, metavolcanites and dolomites. The thickness is around 200 m, where the rocks are Eifelium or Givetium in age (Flügel & Hubmann, 2000).

Table 1:Overview of the formations and the corresponding mineralogy in the survey area.

Group	Formation	Subdivision	Description	Mineralogy
Peggau	Hochschlag		carbonates with small amount of black shales and metavolcanites	carbonates
	Schönberg	Weitzbauer member	black shales with intercalations of dark limestone and lydites	organics, pyrite, graphite, sericite-chlorite, carbonates
Passail	Heilbrunner phyllite	Pramerkogel complex	metavolcanic rocks with arsenopyrite mineralizations	albite-biotite-chlorite phyllites and garnet-biotite-chlorite phyllites
		Heilbrunner phyllite complex	quartz phyllites	garnet-biotite phyllites and epidote-chlorite schists

To simplify comparability with literature such as Bojar et al. (2001), in the following the terms Hochschlag, Weitzbauer, Pramerkogel and Heilbrunner formation will be used.

3 Mining district Straßegg

3.1 Mining history

The former mining area is located between the Zuckenhutgraben and the northern part of the Pramerkogel. The first recorded mining activities in Straßegg are dated to the 15th century, but most likely, the mining history goes back to the 14th century (Weber, 1990). Gold bearing arsenopyrite, galena and pyrite were mined within a 1.8 km long and 300 m wide north-west to south-east aligned corridor, which is fully related to the Pramerkogel formation (Modl et al., 2022). The mining activity stopped in the 19th century, but remainings of the historic mining activities, like waste dumps and mouth holes, can be still seen in the field.

3.2 Previous prospection activities

3.2.1 The magnetic anomaly

In an aeromagnetic survey done by the Geological Survey of Austria in 1992, a positive magnetic anomaly has been found around Straßegg (Figure 5). The anomaly shows two centers of high intensities. One is in the north-west of Straßegg with a total magnetic intensity of 450 nT and one in the south-west of the Pramerkogel with values up to 400 nT. The center of the latter one is in the western part of the survey area. After Antes (1998), the anomaly originates from magnetite and pyrrhotite rich metavolcanic rocks of the Pramerkogel formation in a depth of 500 m below surface.

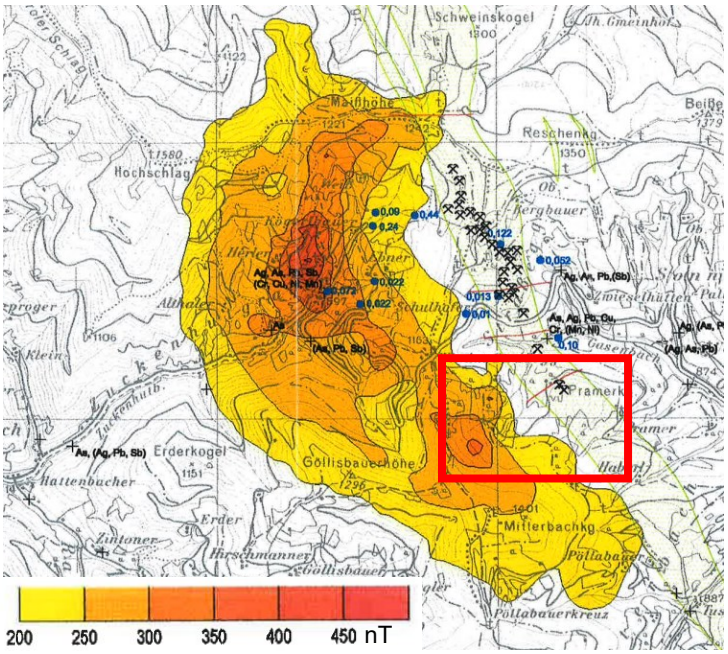

Figure 5: The magnetic anomaly of Straßegg in a map with an extent of 6 x 6 km. The plot shows the reduced anomalies of the total magnetic intensities. The red rectangle indicates the survey area and the greenish zone going from north-west to south-east indicates the area for possible Au-mineralizations after Antes (1998). Old mining activities are also marked on the map (Antes, 1998, Beilage 2).

3.2.2 Ore prospection of Minrex in 1986

During the prospection program of Minrex in 1986, two main trenches and several smaller ones were done in the survey area (Figure 6). Both trenches are located in the greenschists of the Pramerkogel formation, where one is in the north of the Pramerkogel (Trench 6) and one in the south (Trench 7). In Trench 6, two mineralized quartz veins with a thickness of about 0.3 m were detected, where one is discordant and the other one concordant. The concentration of arsenic in the mineralized zones exceeded 4000 ppm. Along with high arsenic concentrations, gold concentrations are also increased up to 40 ppm. Additional trenches in the south-east of the main trench confirm the results. Trench 7 shows no anomalies in gold or arsenic concentrations, but in a side trench (S28) normal to the main one, again high gold concentrations up to 19 ppm, could be detected. At both locations, the mineralizations show a dip of 80 to 90 ° (Minrex, 1987).

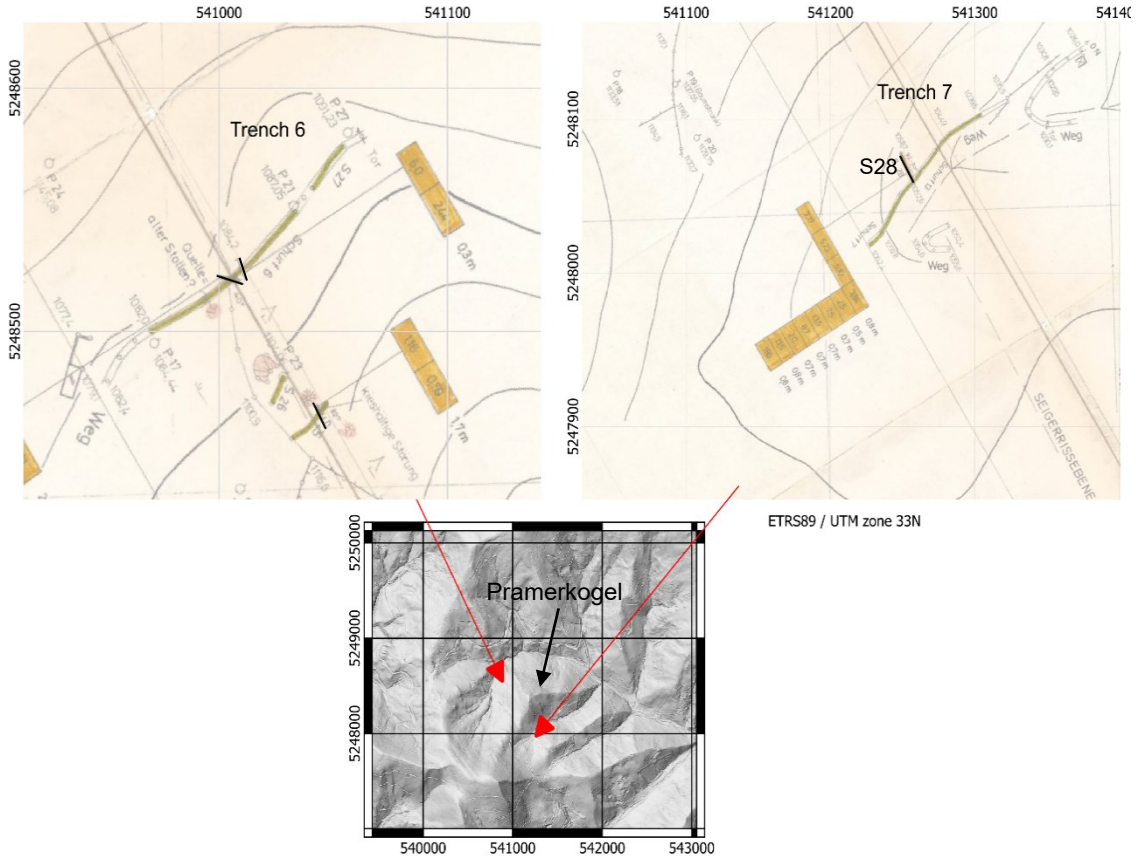

Figure 6:Trenches from the prospection program of Minrex in 1986 north and south of the Pramerkogel. In both trenches, arsenopyrite mineralizations were observed (black lines). The gold concentrations measured in the field are written in orange boxes (Minrex, 1987). The overview map shows an elevation relief taken from basemap.at (2023).

3.3 Arsenopyrite-gold mineralization

The gold bearing arsenopyrite mineralizations are in the hanging wall of the greenschists of the Pramerkogel formation close to the black shale of the Weitzbauer formation (Bojar et al., 2001; Weber, 1990). Two different types of arsenopyrite mineralization could be identified due to the prospection phase from Minrex (Figure 7).

On the one hand, vein mineralization and on the other hand mineralizations with tuberous and plated massive sulfides. The latter ones are parallel to the foliation, where the area of mineralization can reach up to 2.5 m (Minrex, 1987).

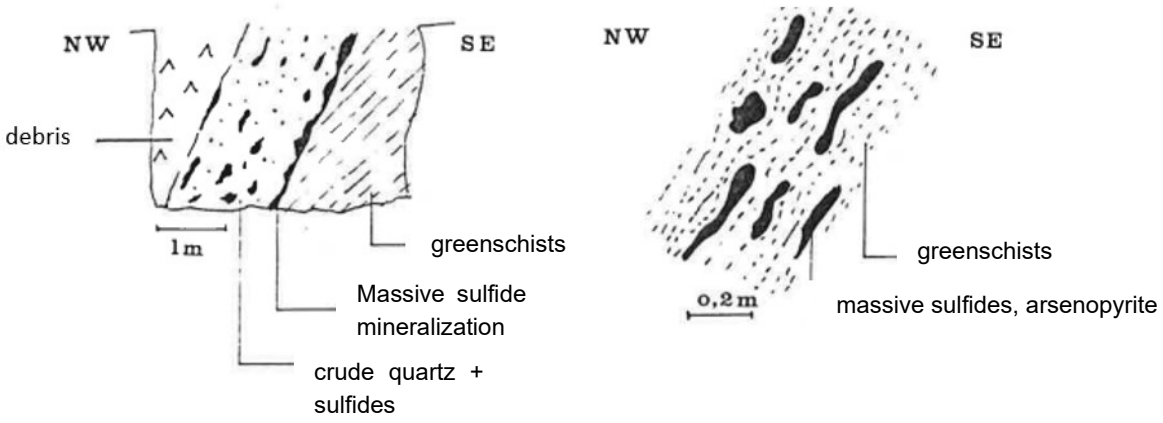

Figure 7:The two gold bearing arsenopyrite mineralization types found in Straßegg (Minrex, 1987).

After Bojar et al. (1998), the ore paragenesis of the vein type mineralization shows two stages. In the first stage, arsenopyrite and pyrite are dominant. Galena, boulangerite, jamesonite, tetrahedrite, bournonite, chalcopyrite and meneghinite are prevailing in the second phase. This second stage minerals overgrow and fill cracks within minerals of the first stage (Bojar et al., 1998; 2001). Gold is associated mainly with stage one minerals, where the gold concentrations range between 2 and 185 ppb and become higher near veins (Minrex, 1987).

3.4 Deposit genesis

After Czermak & Schadler (1933) the deposit character is an epigenetic vein one, because of the discordant mineralized quartz veins. Mineralizations are restricted to one lithological horizon, therefore the first theory of genesis was rejected by Gsellmann (1987), Minrex (1987) and Weber (1990), who believe in a syn-sedimentary genesis. The discordant quartz veins are interpreted as mobilizations of the primary mineralizations. Due to the fact, that the sulfidic mineralizations are not in the black shales, what would be expected in a syngenetic deposit and, furthermore, due to the special host rock type of the gold, arsenopyrite, Bojar et al. (1998) do not support the theory of sedimentary mineralizations. A structure bound mineralization type is assumed, where the mineralizations are restricted to a mylonite horizon. After an analysis of the stable isotopes and mineralogical data, Bojar et al. (2001) concluded that ore mineralization and veins were formed in a rock buffered regime due to local processes and precipitation from meteoric water, which was in equilibrium with the rock. Furthermore, Bojar et al. (2001) point out that the gold mineralization was most likely related to fracturing, depressurization, and cooling from peak metamorphic conditions. Gold mineralizations were precipitated in discordant veins and later folded by a deformation event, which is related to the late Cretaceous extension.

4 Case Studies in literature

Sulfidic, as well as graphitic mineralizations can be detected by many different geophysical methods, depending on the mineral content of the mineralizations itself and the surrounding host rock. Different studies from Austria, but also from other countries, which deal with the prospection of such mineralizations, are presented in this chapter.

An electrical resistivity tomography (ERT) survey was conducted in the Yongjang mine in Korea by Park et al. (2009). Three mineralized quartz veins, surrounded by black shales and hornfelsic shales, are known from this area. The veins show a thickness of 2-40 cm and bear gold, silver and sulfides. The target was to clarify the location of these veins using ground and borehole ERT measurements. In the surface survey, a Dipole-Dipole array was chosen where the different profiles were orientated perpendicular to the strike direction of the quartz veins. After a 3D inversion, the data is presented in different depth slices (Figure 8). In general shales show a broad variety in the resistivity values from 20 to 2000 Ωm and hornfels is represented through higher values (> 8000 Ωm). Low resistivity anomalies could be observed in almost all depth slices, which correspond partly to the estimated location of the mineralized quartz veins (A, B). The third known mineralization is too close to another one, so a distinction cannot be made between them. Since the resolution decreases to greater depths, the continuity of the veins is not so prominent anymore. In addition, a fault line (D) with low resistivities was detected. The positions of the low resistivity anomalies were also confirmed by borehole to surface measurements, which have a higher resolution. In these measurements, an almost vertical alignment of the veins can be seen.

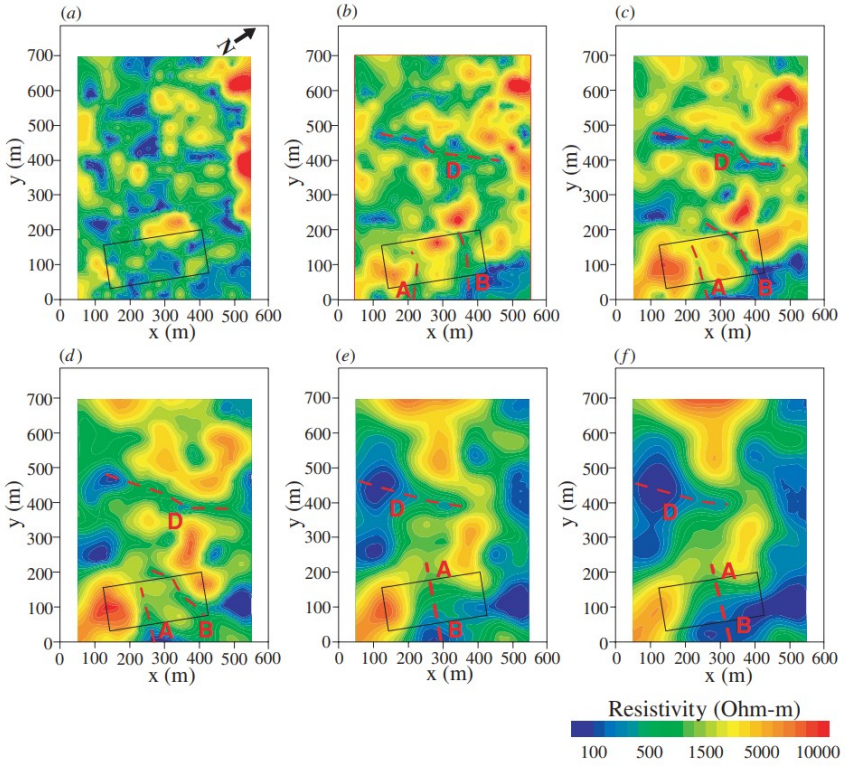

Figure 8: Resistivity planes after 3D inversion at different depths. (a) 5m, (b) 18 m, (c) 35 m, (d) 58 m, (e) 85 m, (f) 118 m. Label A and B indicate the position of the mineralized veins and D represents a fault line (Park et al., 2009, Fig. 6).

Another Study from South Korea, done by Han et al. (2016), was using ERT and induced polarization (IP) to locate mineralization and silicification boundaries of low sulfidation epithermal Au-Ag deposits. The subvertical veins are enveloped by alteration zones and consist mainly of quartz with pyrite, galena, chalcopyrite, Ag and Au rich telluride minerals. For the survey, four profiles with an electrode spacing of 20 m were measured in a Dipole-Dipole array. The authors could define the boundary to the silicified zone at high resistivities greater than 600 Ωm, where the mineralized veins show chargeability values greater than 3 mVV^{-1} (Figure 9c). If the mineralization is not in a silicified zone, it shows low resistivity values smaller than 100 Ωm (Figure 9d).

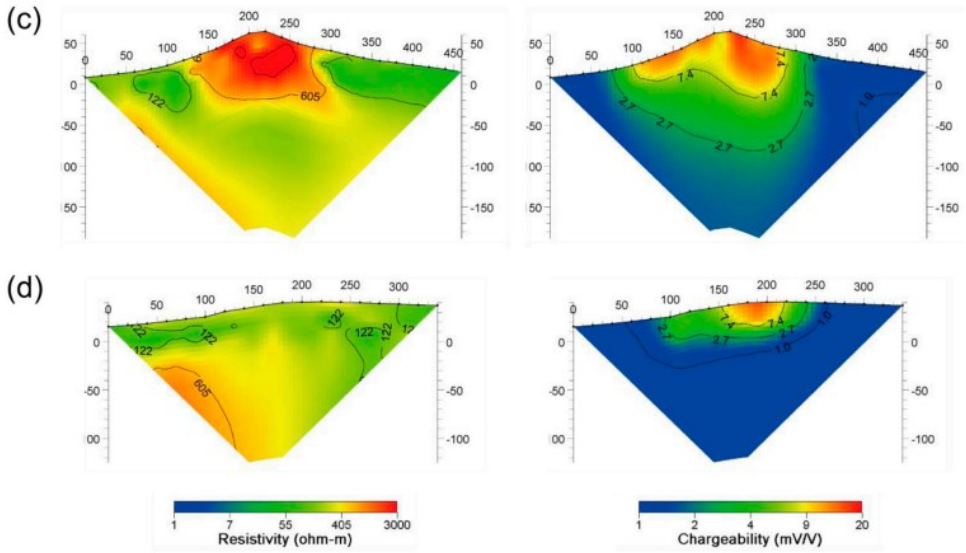

Figure 9: 2D resistivity and chargeability results from two different survey lines. (c) survey line 3 (d) survey line 4 (Han et al., 2016, Fig. 4).

A combination of ERT and Self-potential (SP) measurement was used to locate potential mineralized zones in the North Singhbhum Mobile Belt, India. In the survey area, a volcano sedimentary series is present, which comprises mainly of quartz-mica schists and cherty quartzite. Among others, gold, pyrite, magnetite, pyrrhotite and arsenopyrite can be found in mineralized quartz reefs within the metasedimentary host rock. The ERT measurements were conducted in different electrode arrays. In the Wenner and the Wenner-Schlumberger array, low resistivity anomalies at the surface could be detected. In the Dipole-Dipole array, an additional low resistivity body in a depth of 30 to 50 m could be observed. After a combined inversion of all arrays, three low resistivity zones are visible (Figure 10). Zones JL1 and JL2 are most likely not related to mineralized zones, but rather zones of weathering. The low resistivity zone (JL3) with values of < 100 Ωm is surrounded by high resistivities > 10.000 Ωm and correlates very well with the SP data, which shows an anomaly of about -90 mV. Horo et al. (2020) interpreted this zone as sulfide mineral rich deposit (quartz reef) which is surrounded by metasedimentary rocks.

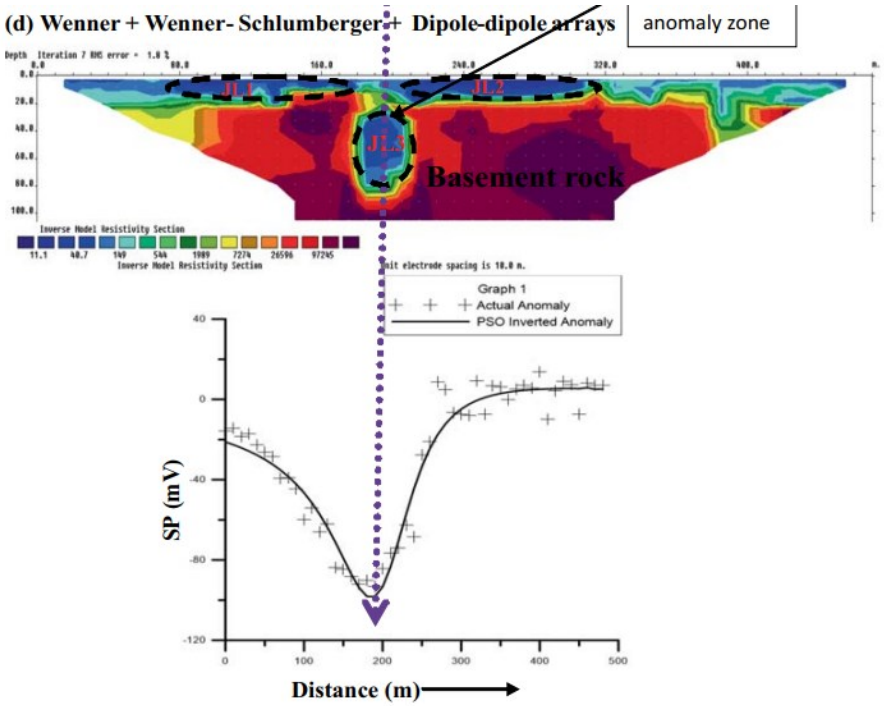

Figure 10: Joint inversion section of Wenner, Wenner-Schlumberger and Dipole-Dipole array and the corresponding SP anomaly curve. Anomaly zone JL3 indicates a possible mineralized zone (Horo et al., 2020, Fig. 3).

The oxidization potential of the Potentsialnoe polymetallic deposit in Russia was measured by applying the SP method. The data collected by Semenov (1975) was re-interpreted by Eppelbaum (2021). Sulfide ores and sulfide impregnations are interbedded in chlorite-sericite schists. Several thin ore bodies are close to the surface in a steep position, which was confirmed due to boreholes. The observed SP anomaly shows values of about -120 mV. The dip of the ore bodies can be seen in the anomaly due to the asymmetry (Figure 11). From several other datasets, which were re-interpreted by Eppelbaum (2021), typical SP values for polymetallic ore bodies range between -60 mV and -500 mV.

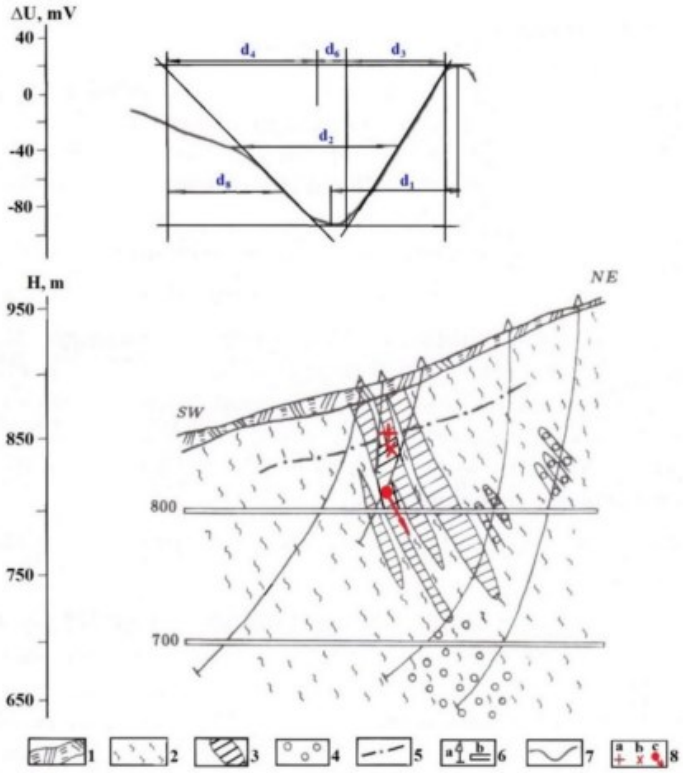

Figure 11: Observed SP anomaly and the related geological model in the Potentsialnoe deposit, Russia.(1) Soil-vegetative layer; (2) chlorite-sericite schists; (3) sulfide ores; (4) sulfide impregnation, pyritization; (5) level of ground water; (6) drilling wells; (7) SP plot; (8) interpretation using characteristic tangent method (Eppelbaum, 2021, Fig. 10).

In the area of Pusterwald, Austria, geophysical and geochemical studies were conducted by Weber et al. (1984) and Stoll & Gurk (2014). Geologically, the area is like the area of Straßegg, with mica schists, quartzite and limestone. The main mineralizations comprise of Au bearing arsenopyrite, pyrrhotite, pyrite and chalcopyrite and are restricted by a mylonite horizon. Additional to the main mineralization, thin Au bearing arsenopyrite mineralizations can also be found. Several geophysical methods were used to locate possible ore mineralizations. In the geomagnetic data several magnetic anomalies could be observed, where the values range from 800 to -2400 nT. On the one hand, smaller anomalies were related to pyrrhotite which is in close contact to the Au bearing arsenopyrite, and on the other hand, larger anomalies with more than 1000 nT were related to an amphibolite complex. SP anomalies with values of -1000 mV were observed at the mylonite zone. This was explained by the occurrence of graphite at shear surfaces, which also correlates with very low specific resistivity values (< 10 Ωm). Due to this low value, a meaningful interpretation of IP measurements was not possible. However, it cannot be ruled out that further mineralizations also contribute to this low SP values.

Numerous different studies concluded that graphite bodies are in general less resistive than the surrounding rock, show a higher chargeability and a negative self-potential anomaly. Jalete (1997) defined graphite bodies in Gara-Gedemsa, Ethiopia, as bodies with resistivity values lower than 10 Ωm and 40 to 70 ms of chargeability. Graphite bodies in Lofoten, Norway, were studied by Ronning (2017). Resistivity values below 20 Ωm and SP anomalies greater -100 mV could be observed. In a study from Madagascar done by Heritiana (2019), SP, ERT and IP methods were used for the identification of graphite bodies. Where graphitic contents were higher than 5 %, negative SP anomalies, low resistivity and high chargeability values were observed. In contrast to the above-mentioned studies, Gautneb et al. (2020) could not confirm a clear correlation between graphite bodies and the IP results, while SP and ERT data verified the location of the mineralized graphite bodies. Exemplary for the localization of graphite mineralizations, Figure 12 represents a SP and ERT survey from Madhusudan et al. (1990) done in Orissa, India. An asymmetric SP anomaly can be observed in an area of low apparent resistivities (< 100 Ωm). These indications for a graphitic mineralization also fit well to the simplified geological model.

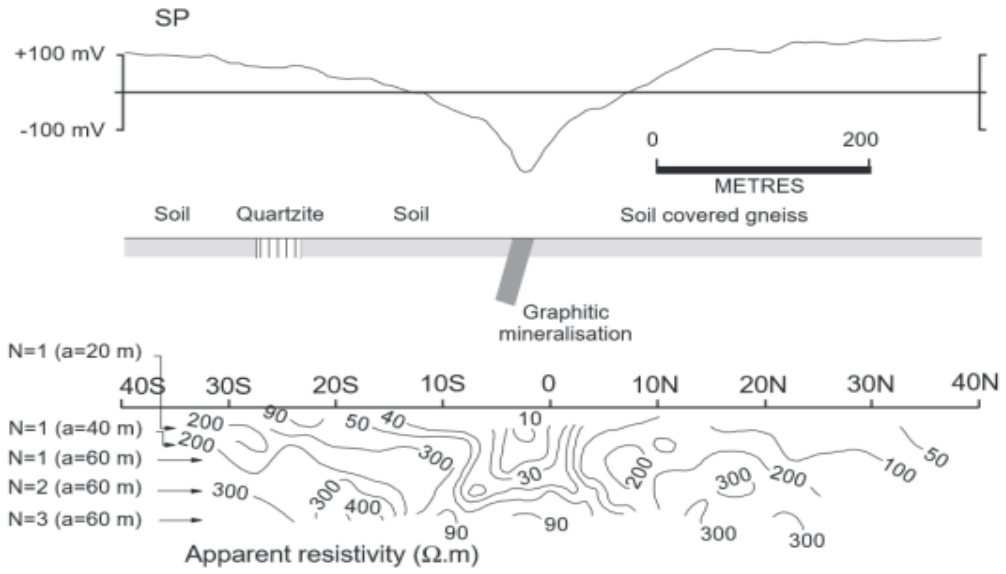

Figure 12: SP plot, the simplified geological model and results of an ERT survey done in Orissa, India (Barrett & Dentith, 2003; Fig. 16).

5 Basic Principles

5.1 Geomagnetism

The geomagnetic field is a potential field and, for every point on the Earth, it can be described through its strength and orientation. For the orientation of the field vector, declination, which describes the deviation of magnetic to geographic north, and inclination, the dip angle of the field, are used (Figure 13). The geomagnetic field consists of three components. The main field, a fluctuating and an anomaly field. The main field is slowly changing and overlain by a fast-changing field coming from outside of the earth. In addition, these global components are overlain by a relatively constant local anomaly field, which origins from the upper crustal part of the earth. Geological structures with ferromagnetic minerals or magnetic materials in waste deposits could lead to such a local anomaly, where the detection of this is the goal of the magnetic method (Knödel et al., 1997). The response of a magnetic body in the subsurface depends on the location on Earth, the size, the depth and the susceptibility. At middle northern latitudes, the measured signal is a dipole one with a minimum in the north and a maximum in the south. The shallower the magnetic body or the higher the susceptibility, the stronger is the magnetic response. However, the strength of the magnetic field is measured using magnetometers as total magnetic intensity (TMI), which describes the sum of the three field components. Therefore, the main and the fluctuating field must be removed to receive the anomaly field, which can be further used for the interpretation of magnetic anomalies in the subsurface.

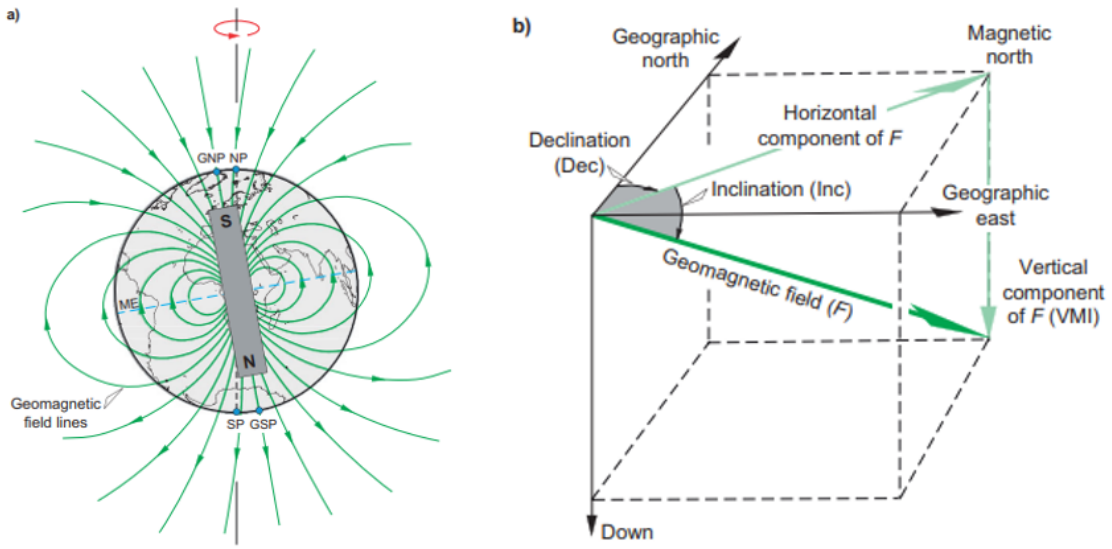

Figure 13: (a) Approximated geomagnetic field, GNP/GSP: geomagnetic north/south pole, NP/SP north/south geographic pole, ME: magnetic equator, (b) Geomagnetic field vector (Dentith & Mudge, 2014, Fig. 3.20).

Types of Magnetometers

Different systems of measuring the magnetic field are available. Total magnetic intensity magnetometers like the Overhauser, Cesium or Proton precession magnetometer are most common. In addition, vector magnetometers like the Fluxgate magnetometer can also be used to characterize the magnetic field. These types of magnetometers are more often used in downhole magnetometry for inclination and declination measurements. The Proton precession magnetometer is working in 4 steps. In a first step a current passing through the sensor polarizes protons of a proton rich liquid like kerosene. Subsequently, a short pulse deflects the magnetization of the protons into a plane of precession. The following pause causes a slow decay of the precession signal and electrical transients can be removed. The remaining proton precession frequency can be measured and converted, to get the total magnetic intensity (GSM-19 v7.0 Instruction Manual). The precision of Proton magnetometers is in a range of 0.1 nT with a measurement rate of about 1 second. An Overhauser magnetometer can achieve the same precision, but measuring rates are ten times higher. For airborne measurements, the Cesium magnetometer is used with a continuous measurement rate and a higher precision.

5.2 Paleomagnetism

The anomaly field of a magnetic body in the subsurface can be created by two types of magnetism. A remanent and an induced magnetism, where minerals can show both, one or none of the before mentioned magnetization types (Dentith & Mudge, 2014). The type of magnetization is thereby closely related to the magnetic structure of minerals.

5.2.1 Magnetic structures

Magnetic structures in a material can be grouped into three types. Dia, Para and Ferromagnetism. Most of the earth's crust is diamagnetic, which means that electron spins are aligned opposite to an external field resulting in a weak negative susceptibility. These materials can be therefore seen as nonmagnetic. If the electron spins are aligned with the external field, they produce a weak positive susceptibility and are paramagnetic. Both types can only show induced magnetism (Dentith & Mudge, 2014). However, the target of the magnetic method are ferromagnetic materials. Here, atomic dipoles are magnetically coupled in many ways (Figure 14). Ferromagnetic minerals are among others magnetite, hematite and pyrrhotite.

Ferromagnetism

Domains represent volumes of the lattice, where the magnetic vectors are aligned parallel. The higher the number of domains, which are aligned parallel with an external field, the higher is the magnetism. Therefore, ferromagnetic materials can have high susceptibilities and strong magnetism. Another type of Ferromagnetism is called Antiferromagnetism, where the domains are parallel and antiparallel aligned. Canted-antiferromagnetism describes not perfectly aligned dipoles, which can lead to a small remanent magnetization.

High positive susceptibilities can be reached due to Ferrimagnetism. Here, domains are aligned parallel and antiparallel, but one domain shows a higher magnetization than the other one (Butler, 1992; Dentith & Mudge, 2014).

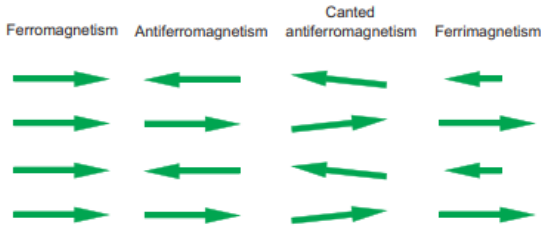

Figure 14: Types of ferromagnetism (Dentith & Mudge, 2014, Fig. 3.7).

5.2.2 Induced magnetism

The strength of the induced magnetism is proportional to an applied external field, where the induced field is parallel to the external field. The higher the applied magnetic field, or the higher the magnetic susceptibility, the higher is the induced field strength (Dentith & Mudge, 2014).

$$J_{induced} = \frac{B}{\mu_0} * \kappa$$

$J_{induced}$ …induced magnetism [A/m]
B…external field [T]
μ_0 ...magnetic permeability of vacuum [H/m]
κ…susceptibility [1]

Magnetic susceptibility, which is the main driver of the strength of the induced magnetization, describes the degree of the probability of a material to get magnetized. It is dependent on magnetic permeability, which describes how easily a magnetic field can exist in a material. For nonmagnetic minerals, the magnetic permeability of the material and the magnetic permeability in vacuum are approximal the same (Dentith & Mudge, 2014).

$$\kappa = \frac{\mu}{\mu_0} - 1$$

μ…magnetic permeability [H/m]

5.2.3 Natural remanent magnetism (NRM)

In some materials, an external magnetic field applied during the formation can cause irreversible changes to the magnetic properties of the material. This means that the magnetic properties do not change if the external field is removed. This primary remanence is caused through thermoremanent, chemical and detrital processes.

In addition, secondary remanence components derived through isothermal or viscous processes can also enhance the remanence. The vector sum of these various remanent magnetisms is called Natural Remanent Magnetism (Butler, 1992). Like the induced magnetic field, the remanent magnetic field is also aligned parallel to an external field.

$$J_{remanent} = \frac{B_{paleo}}{\mu_0} * \kappa$$

$J_{remanent}$ …remanent magnetism [A/m]

B_{paleo} …external field at formation [T]

Processes of remanent magnetization

The occurrence of remanent magnetism can have different origins. However, independent of the process, ferromagnetic minerals must be present to generate the magnetic field. One of the most common processes is thermoremanent magnetization. Here, the ferromagnetic minerals cool down below the mineral specific Curie temperature, where the transition between ferro and paramagnetism takes place. As a result, the prevailing external magnetic field at that moment will be stored in the mineral. This could happen due to volcanism or metamorphism. A chemical remanent magnetism occurs due to recrystallization of ferromagnetic minerals. Weathering or metamorphism could lead to such a recrystallization, where the external magnetic field at that moment will be stored. Another type of magnetism is the detrital remanent magnetism, which can occur during deposition and lithification of sedimentary rocks (Butler, 1992). Due to a lightning strike, isothermal remanent magnetization could take place. An overprint with a long applied magnetic field causes a viscose remanent magnetism. As an indication, if remanent or induced magnetism prevails, the Königsberger ratio Q can be calculated. A ratio above 1 means remanent magnetism is prevailing and below 1 induced magnetism is more representative.

$$Q = \frac{J_{remanent}}{J_{induced}}$$

Q…Königsberger ratio [1]

5.2.4 Magnetic mineral classification

Based on the magnetic susceptibility, the natural remanent magnetism, Curie temperature and the isothermal remanent magnetism, conclusions about magnetic minerals in a rock can be drawn. These informations can be gained by laboratory measurements.

Curie temperature

The interaction between molecules in a material is temperature dependent. At higher temperatures, the spacing of atoms in the crystal lattice gets greater and therefore the intermolecular interaction of a material gets weaker.

This results in a smaller magnetic moment. At the Curie temperature, the intermolecular interactions collapse and the magnetic moments are randomly distributed in the material. As a result, above this temperature, ferromagnetic materials behave like paramagnetic materials. Cooling down the material again below the Curie temperature leads to a reorganization of the electron pairs. The Curie point is therefore a material specific value and can be used for the classification of a material (Butler, 1992).

Isothermal remanent magnetization (IRM)

Other parameters to distinguish between materials can be derived from the induction of an artificial magnetic field in a certain direction. The material, which is exposed to this artificial field, gets a stepwise magnetization till a saturation is reached. To determine also the remanent coercive force, a magnetization in the opposite direction as before is applied. This is done stepwise until the already induced magnetization is degraded. The half value of the saturation and the remanent coercive force are mineral specific values and can be used for a classification.

5.3 Geoelectric methods

Unlike geomagnetic, geoelectric methods are active methods, which means that an artificial electric field is necessary. One can distinguish between electrical and electromagnetic measurements. In purely electrical measurements, direct or alternating currents are induced to excite the subsurface, whereas in electromagnetic measurements periodic or pulse-like excitations are used (Knödel et al., 1997). Electrical resistivity tomography and induced polarization are the main methods of purely electrical measurements.

5.3.1 Electrical resistivity tomography (ERT)

The goal of the electrical resistivity tomography (ERT) is to determine the distribution of the specific resistivity in the subsurface. Therefore, electrical conductivity in the subsurface is necessary, what is achieved by ionic or matrix conductivity. Ionic conductivity depends on the properties of the pore fluids. The mobility of ions, the volume of fluid, temperature and concentration of the electrolyte are the controlling factors. Furthermore, the formation factor, which describes the complexity of the current flow paths, is also influencing the ionic conductivity. The matrix conductivity depends on conductive minerals in the subsurface. Since most minerals are electric insulators, the matrix conductivity is less prominent than ionic conductivity. However, if conductive minerals are present, the conductivity could be significantly high. In addition, clay minerals can also result in a high conductivity, depending on the clay type, grain size and distribution (Dentith & Mudge, 2014). Typical minerals, which can have high conductivity values are graphite, sulfides and oxides.

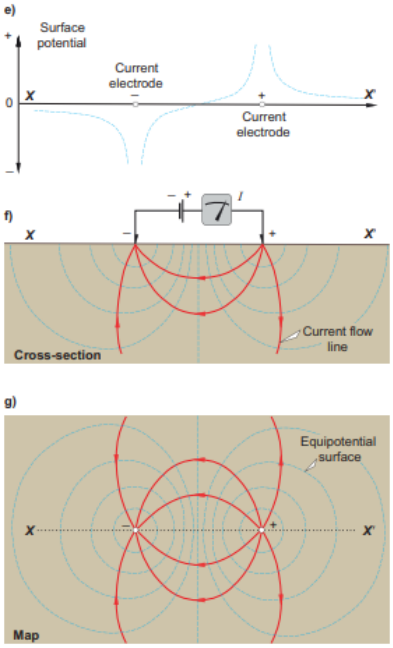

Figure 15: Theoretical representation of a geoelectric resistivity measurement (e) Current dipole (f) Cross sections of a measurement profile (g) Top view of a measurement profile (Dentith & Mudge, 2014, Fig. 5.34).

The artificial electric field, generated by a battery or a generator, is conducted into the ground via electrodes called current electrodes. This results in the formation of a spatial potential field, which is influenced by changes in the conductivity in the subsurface. Differences in the electrical potential are measured by a second pair of electrodes on the surface, the potential electrodes. The arrangement of two current and two potential electrodes is called a four-point arrangement. By measuring the potential curve, the spatial distribution of conductivity and resistivity can be determined (Knödel et al., 1997). Figure 15 shows the propagation of current flow lines and equipotential lines along a measured profile X-X'. Both, the current flow lines and the equipotential lines, are spatially extended and not limited to the direct subsurface below the profile.

The fundamental relationship for direct current geoelectric is the linear relationship between current, voltage and resistance. This is described by Ohm's law:

$$R = \frac{V}{I}$$

R....resistance [Ω]
I.....current [A]
V....voltage [V]

Electrical resistance is independent of the geometry of a conductor. However, the specific resistivity ρ involves the geometry of a conductor.

$$\rho = R * \frac{A}{l}$$

A... cross section of the conductor [m²]
l.... length of the conductor [m]
ρ....specific resistivity [Ωm].

To be able to determine the specific resistivity of a homogeneous half-space, the potential difference ΔV between the potential electrodes is calculated from the superposition of the individual potentials according to the superposition principle (Knödel et al.,1997; Dentith & Mudge, 2014). In Figure 16, electrode A represents the anode and electrode B represents the cathode. Furthermore, electrodes M and N are defined as potential electrodes. The distances between the electrodes are denoted by X.

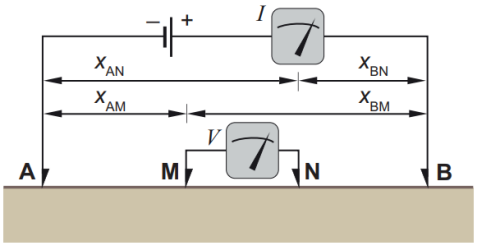

Figure 16: Electrode configuration in a four point array. AB representing current electrodes, MN potential electrodes (Dentith & Mudge, 2014, Fig. 5.36).

$$\Delta V = \rho * I * \left[\frac{1}{2\pi} * \left(\frac{1}{X_{AM}} - \frac{1}{X_{BM}} - \frac{1}{X_{AN}} + \frac{1}{X_{BN}}\right)\right]$$

If one introduces the term $\frac{1}{K}$ and thus, replaces the term in the brackets from the above-mentioned formula for ΔV, it results, according to Knödel et al. (1997), in the specific resistivity of a homogeneous half-space.

$$\rho = \frac{\Delta V}{I} * K$$

K…geometric factor [m]

Because the geological subsurface is usually inhomogeneous, the calculated resistivity is interpreted as the apparent resistivity (Knödel et al., 1997).

Electrode arrangement

Different arrangements of electrodes can be used in a geoelectric survey. These different arrays have different advantages and disadvantages. Among others, the resolution and the depth of penetration are influenced by the choice of the array. In the following, the two used electrode configurations are more closely explained.

Pole-Dipole array

The Pole-Dipole arrangement is an asymmetric array. In difference to the Dipole-Dipole array, it uses a remote electrode for current injection. Therefore, the depth of penetration is high compared to other arrays. The throwback in this setting is the small M-N spacing compared to the large A-B spacing. This results in a poor signal to noise ratio and must be compensated by using higher currents. As shown in Figure 17, the current electrode B and the potential dipole M-N are separated from each other by a factor of nX. As an estimation for the depth of penetration Z, the formula in Figure 17 can be used.

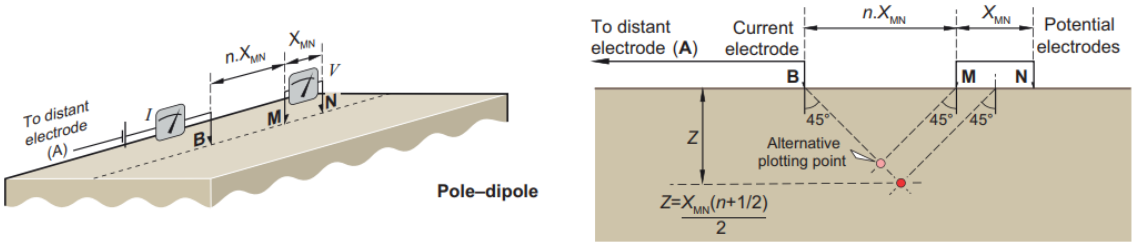

Figure 17: Schematic illustration of a Pole-Dipole array (Dentith & Mudge, 2014, Fig. 5.40).

Wenner array

The Wenner array is characterized by a symmetrical setup geometry. Here, a high layer resolution of horizontally layered underground is achieved. Compared to the asymmetric arrangements, like the Dipole-Dipole arrangement, a lower lateral resolution can be expected (Knödel et al.,1997). The signal to noise ratio is very good since higher potentials can be measured due to the large distances between the potential electrodes. Figure 18 shows the electrode arrangement. The dipole length X between the electrodes is constant. Furthermore, the electrodes are arranged in the form A-M-N-B in contrast to the Pole-Dipole arrangement A-B-M-N.

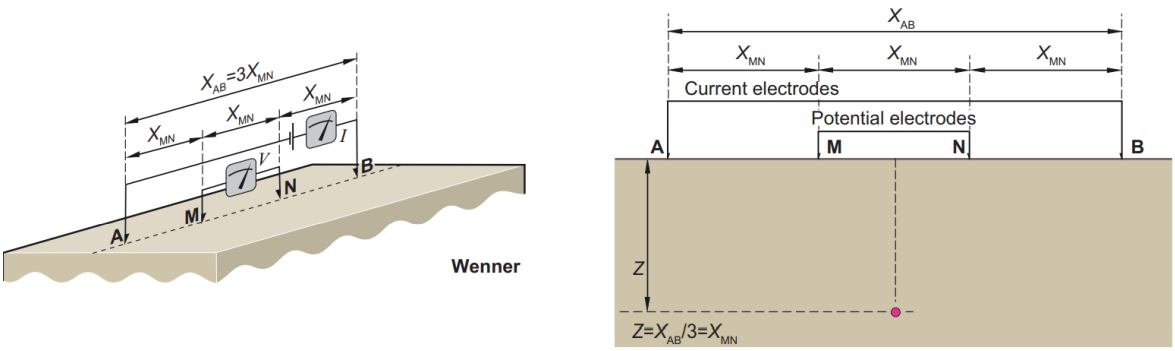

Figure 18: Schematic illustration of a Wenner array (Dentith & Mudge, 2014, Fig. 5.40).

5.3.2 Induced polarization (IP)

The IP measurement is based on the artificial polarization of minerals in the subsurface by applying voltage. Sulfidic minerals like pyrite and chalcopyrite are typical representatives for high chargeability, whereby malachite and hematite show almost no chargeability. The measurement can be conducted in time or in frequency domain, where the two main processes leading to a polarization are the membrane and the grain polarization.

Membrane polarization

A membrane polarization can be created due to narrow porethroats or due to clay and fibrous minerals in the subsurface. Both processes are based on the fact that in most minerals negative surface charges occur. If these minerals build up the pore walls, electrons get repelled and positively charged ions from the pore fluid are attracted. When, additionally, the pore space gets narrower, these thin layers (membranes) of protons can form a barrier and hinder electrons from passing by. On one side of the barrier an electron enhancement and on the other side, a lack of electrons leads to electrical polarization (Figure 19b). Due to strong surface charges of clay minerals, a cloud of positive ions can be concentrated around the mineral and hinders electrons to flow (Figure 19c). During the period where a potential is applied, ions with the same polarity are gathered and others are repelled away (Dentith & Mudge, 2014). In the moment, where the potential is turned off, the ions balance again. In difference to the grain polarization, this effect can also be measured with the self-potential method, without applying voltage.

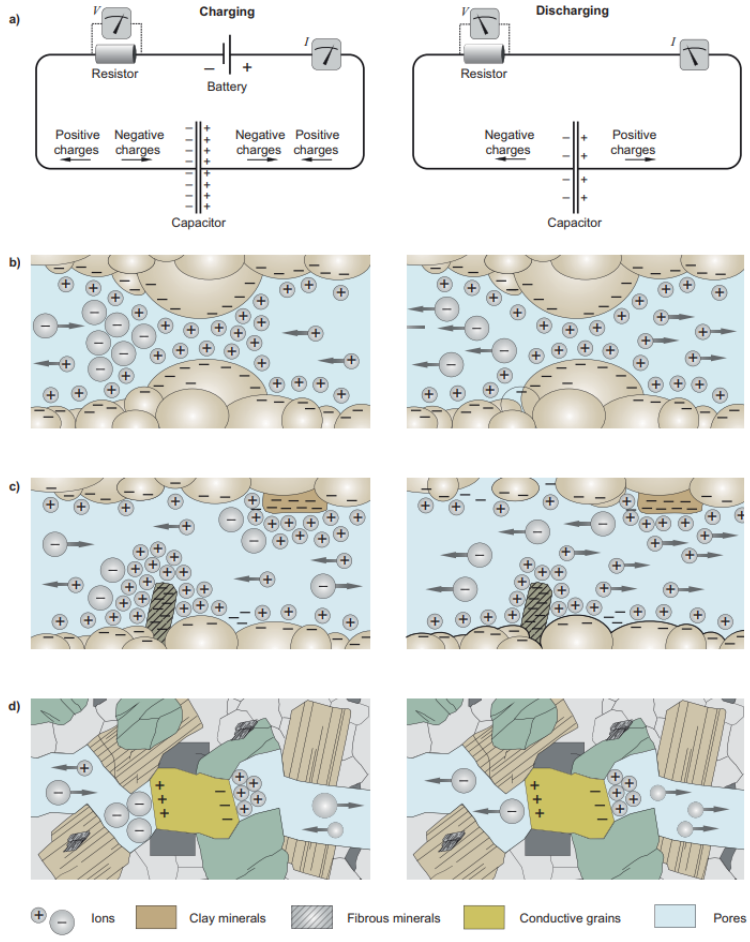

Figure 19: Types of polarization of the ground due to charging and discharging (a) Capacitor principle (b) membrane polarization due to narrow porethroats (c) membrane polarization due to clay and fibrous minerals (d) grain polarization (Dentith & Mudge, 2014, Fig. 5.19).

Grain polarization

The effect of the interaction of ions in the solution and a conductive grain is known as grain polarization (Figure 19d). It can occur when conductive sulfides, oxides or graphite are present. If a voltage is applied, a current flow and therefore a flow of ions in the pore fluid takes place. When a conductive grain hinders the ions to flow, they are electrically interacting with the grain and exchange electrons to provide a current flow. Due to the exchange of electrons the grain gets polarized because of the attraction of opposite charges on the opposite sides of the grain. If the applied potential is turned off, the potential difference will decrease to zero again (Dentith & Mudge, 2014).

Time domain measurement

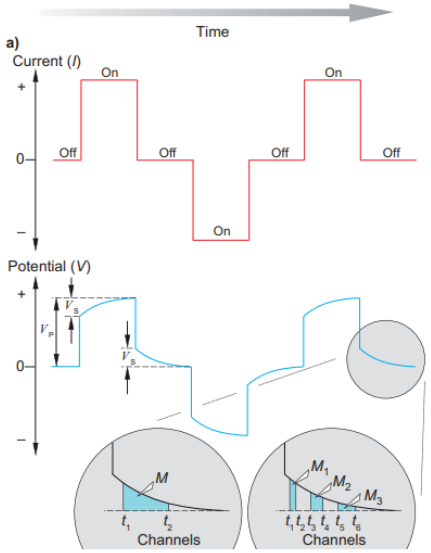

Figure 20:Time domain IP measurement showing a square wave signal and the corresponding potential curve. The enlarged sections showing different time intervals dt (Dentith & Mudge 2014, Fig. 5.37).

In time domain measurements, a steady current is alternately turned on and off, where the polarity changes after each cycle (Figure 20a). The time the current is switched on must be long enough to fully polarize the subsurface and is usually a few seconds. The reached stable voltage value is called primary voltage. This voltage can be used to calculate the apparent resistivity. The measurement itself is happening in the off period. After the current is switched off, a sharp drop of the voltage followed by a gradual decay can be observed (Figure 20b). The voltage value, where the gradual decay begins is called secondary voltage. The measurement of the decay in predefined time intervals and a normalization of the voltage to the primary voltage results in chargeability M.

$$M = \frac{1}{V_p}\int_{t_1}^{t_2} V(t)dt$$

M..Chargeability [ms]
Vp..primary voltage [V]
V(t)..voltage at time t [V]

Frequency domain measurement

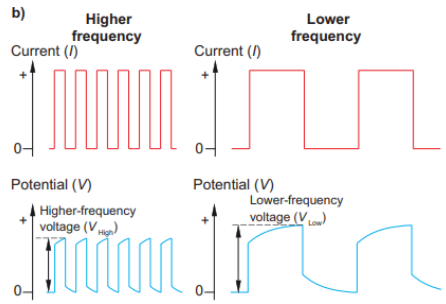

Figure 21: Frequency domain IP measurement with two different input frequencies and the corresponding potential curve (Dentith & Mudge, 2014, Fig. 5.37).

In the frequency domain, different frequencies are used for the measurement. At high frequencies, the primary voltage cannot be reached because the time for fully polarizing the subsurface is too short. On the other hand, at low frequencies, the ground can be more polarized and the primary voltage is higher (Figure 21b). Therefore, the primary voltage of the low frequency measurements is used for the calculation of the apparent resistivity of the ground. Both resistivity values, from high and low frequencies, are used to calculate the induced polarization parameter called percentage frequency effect (PFE).

$$PEF = \frac{\rho_{low} - \rho_{high}}{\rho_{high}} * 100$$

PEF..percentage frequency effect [%]
ρ_{low}...apparent resistivity at low frequency [Ωm]
$\rho_{high...}$apparent resistivity at high frequency [Ωm]

The PFE normalized by the resistivity of the low frequency is known as the metal factor, what can be used as an indicator for the metal content in the subsurface. Another parameter for the induced polarization is the relative phase shift (RPS), which describes the phase shift between the input signal and the measured voltage.

$$RPS = \phi_{low} - \phi_{high}$$

RPS…relative phase shift [°]
ϕ_{low}…. phase shift at low frequencies [°]
ϕ_{high}…. phase shift at high frequencies [°]

5.4 Self-potential (SP)

The Self-potential method is one of the simplest and most inexpensive methods in geophysics. The system consists of two non-polarizable electrodes, a connecting cable and a multimeter. Due to an incomplete understanding of the causes of natural potentials and due to the limited penetration depth, the method is not often used in mineral exploration. However, a direct detection of metal sulfides, metal oxides and carbonaceous mineralization is possible. The SP method is a passive method, which measures changes in the natural occurring electric potential due to spontaneous polarization without applying any current. These electrical potentials can arise due to electrochemical or electrokinetic processes in non-mineralized as well as in mineralized zones. Electrochemical processes lead to Redox reactions, membrane and diffusion potentials. Electro filtration and flow potentials are generated by the movement of water in the subsurface. Due to water flow across boundaries between materials with different electrical properties, a potential anomaly can occur. Furthermore, the interaction of ions in the groundwater with different concentrations and mobility could lead to an anomalous potential (Dentith & Mudge, 2014; Knödel et al., 1997). Larger anomalies with a few hundred millivolts are caused by mineralized sources (Figure 22a) which is best described after the model of Sato and Mooney (1960). A conductive ore body (Figure 22b) is partly below and above the water table. Below the water table an anodic half-cell reaction takes place, where ions of the solution get oxidized when in contact with the ore body. Above the water table, the opposite, a reduction takes place. Due to the oxidization, electrons become free and move upwards to the reduction zone, where electrons are needed. As a result, a negative potential is generated on the shallow outer part, relative to the deeper outer part.

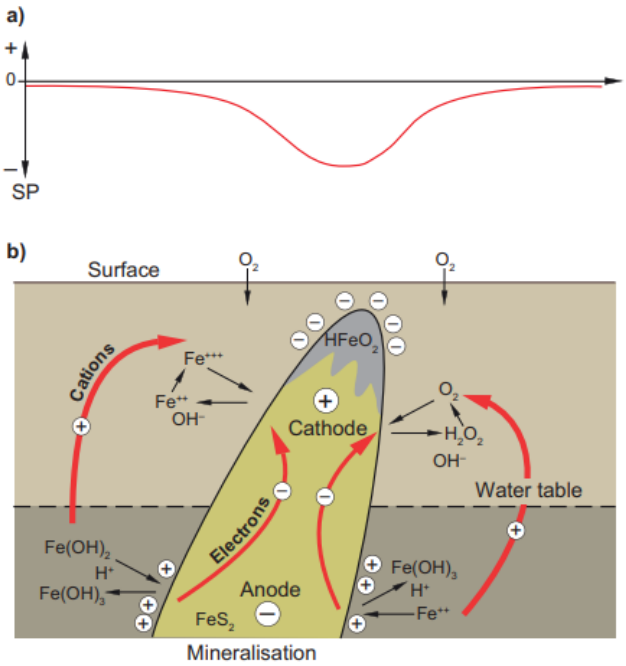

Figure 22: (a) Illustration of an iron sulfide ore body (b) corresponding signal, measured with the SP method (Dentith & Mudge, 2014, Fig. 5.27).

In nature, reduction environments are less common than oxidization ones, therefore in most surveys one would detect a negative potential anomaly. A positive anomaly could be caused by organic decay on a landfill.

Electrode arrangement

The SP method can be done in two different arrays. In a fixed base setup (Figure 23a), where just one electrode is moving and in a gradient array (Figure 23b), where both electrodes are moving along the profile. The fixed base station array is in general preferred because the errors of the individual measurements do not sum up.

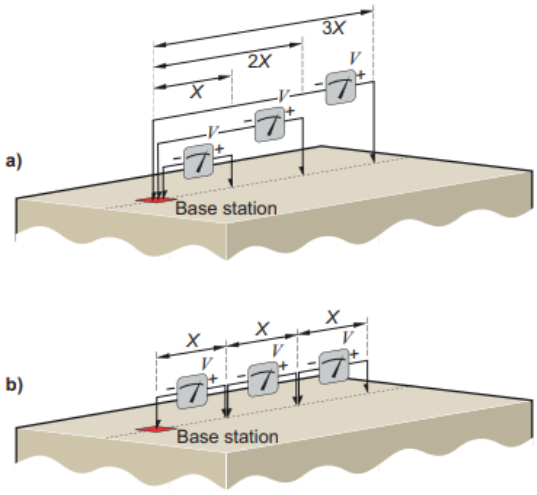

Figure 23: SP electrode configuration (a) fixed base array (b) gradient method (Dentith & Mudge, 2014, Fig. 5.28).

6 Field work

The field measurements were carried out between September 2022 and March 2023 and in total 16 profiles were measured (Figure 24). The profiles are aligned west to east, to be roughly perpendicular to the general strike of the geological formations, which is north-east to south-west. The average length of the profiles is 1100 m and a profile spacing of 50 m was realized. Due to the higher time demand of SP measurements compared to magnetic ones, only every second profile was measured. This results in a profile spacing of 100 m for the SP measurements. The sampling interval was varying between 5 and 10 m for SP and magnetic and every point was recorded with a GPS. In areas where the measured values deviated strongly, the sampling distance was decreased. In addition, two geoelectrical profiles were conducted to confirm anomalies seen in the magnetic and SP measurements. Data from field workshops organized by the Montanuniversität Leoben will be used as additional information. Profile fw01 and fw02 consists of ERT, magnetic, self-potential and geochemical data, which were collected in April 2022. Data from profile fw03 were collected in October 2022 and includes besides the above-mentioned data also seismic data. The susceptibility was measured on outcrops, especially along the trenches.

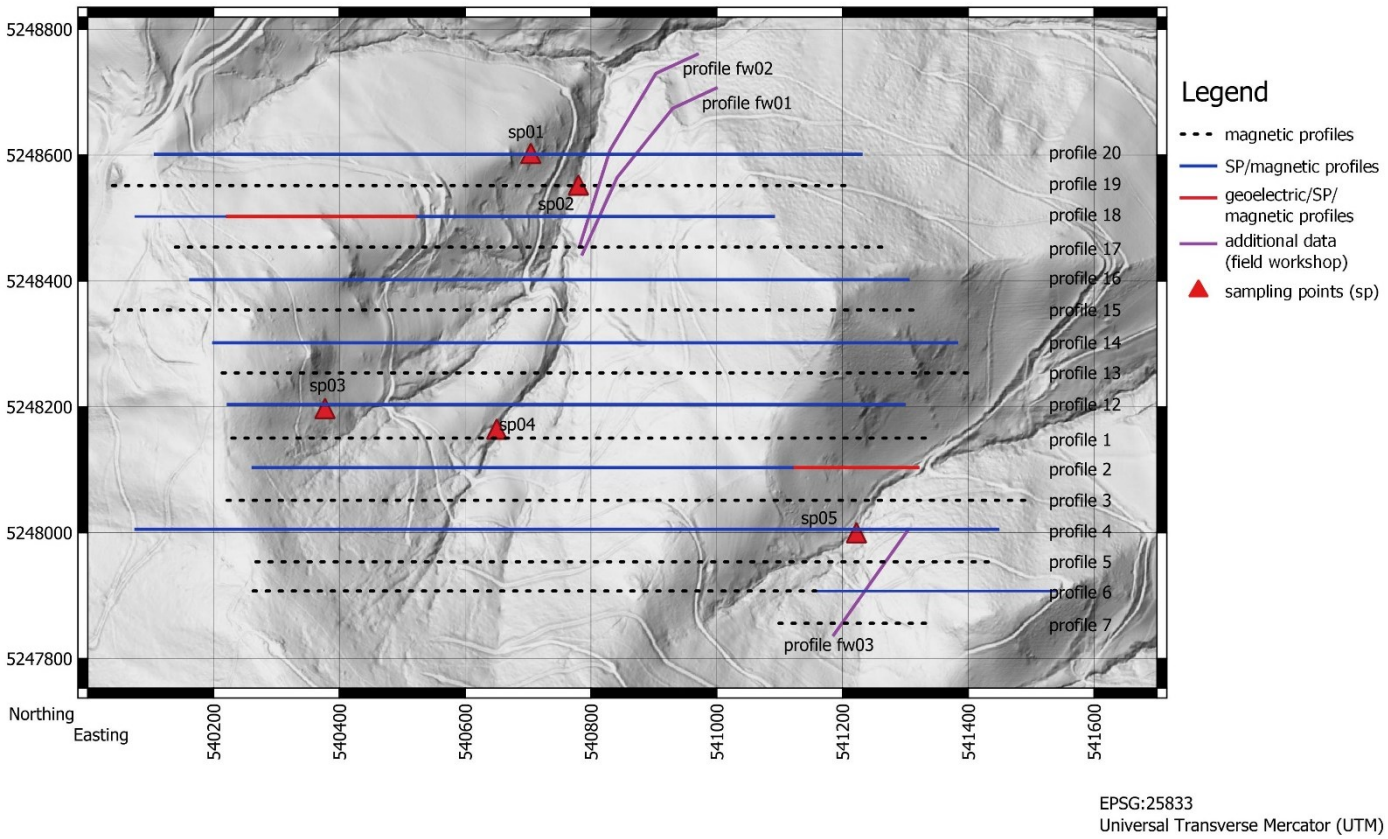

Figure 24: Overview of all data, which will be used to characterize the survey area. Background: elevation relief (basemap.at, 2023).

6.1 GPS measurements

For the positioning of the profiles, two different GNSS systems were used. The handheld Garmin GPSMAP 64s with an accuracy of about 3 m and a Trimble R8s antenna with a Trimble TSC5 Controller and a precision of a few centimeters. A built-in SIM card in the Trimble device ensures that Real Time Corrections (RTK) can also be used to get highly accurate data, which is of special importance for geoelectric measurements. It must be mentioned that large parts of the profiles are in the forest, where both systems show high variation in accuracy. This is due to the high scattering of the signal because of trees.

6.2 Magnetic measurements

For the magnetic field measurement, a Proton precession magnetometer model GSM-19T from GEM Systems was used. The positions of the two sensors T1 and T2 were 1 m and 2 m above the surface (Figure 25) and the sensors are connected to the control unit, which is carried by the operator. The “Gradiometer”-setting was the operating mode for this acquisition, where the total field strength at 1 m and the gradient between the two sensors are recorded. The device also records the time (in UTM) and the quality of each measurement. The quality is described by two values, the first for the noise to signal ratio, the second indicates the duration of the precession recording. During the survey, the quality and gradient values were observed and if one of them showed an unusual behavior, the point measurement was repeated. In areas of a trench, no data was collected, because the high relief could distort the results. It was renounced to use an additional base station to measure the diurnal field variation. On the one hand this is because of the spatial closeness to the Conrad Observatory (65 km), and on the other hand a Bachelor thesis done in the survey area confirmed that the differences are neglectable (pers. Com., R. Scholger,11. October 2022)

Figure 25: Proton precession magnetometer GSM-19T from GEM Systems. The two sensors filled with kerosene are 1 m and 2 m above the ground.

6.2.1 Susceptibility

The susceptibility was measured with a Kappameter Exploranium KT9. Here, a small hemisphere with a radius of five centimeters is measured to get the susceptibility of this volume. The measurement was done along trenches and on accessible outcrops. Along the outcrop of sampling point 5 (Figure 24, sp 5), 3 profiles were recorded with a length of 70 cm.

6.3 Self-potential measurement

Self-potential measurements (Figure 26) were carried out with two non-polarizable electrodes. These electrodes were made by the Montanuniversität Leoben and consist of a casing with a wire made of copper in the center. The wire is surrounded by a Copper sulphate solution, which penetrates through a piece of wood slightly into the ground. Therefore, the wire is not in direct contact with the ground and the electrode can be seen as non-polarizable. The connection between the two electrodes is realized by a 300 m long cable. For the measurement of the potential, a FLUKE 76 true rms multimeter was used. The fixed station gradient was chosen, which means that the location of the base station was only shifted every 300 m. Due to the fact, that this method measures a relative potential, a common zero had to be introduced and all profiles should be connected to that zero point. The point should be in an undisturbed area with some distance to anomalies. By measuring always from a new profile to another already measured one, a relation was introduced and all potentials of the new profile are shifted according to this difference. In this survey, the zero point is located at the western end of profile 20.

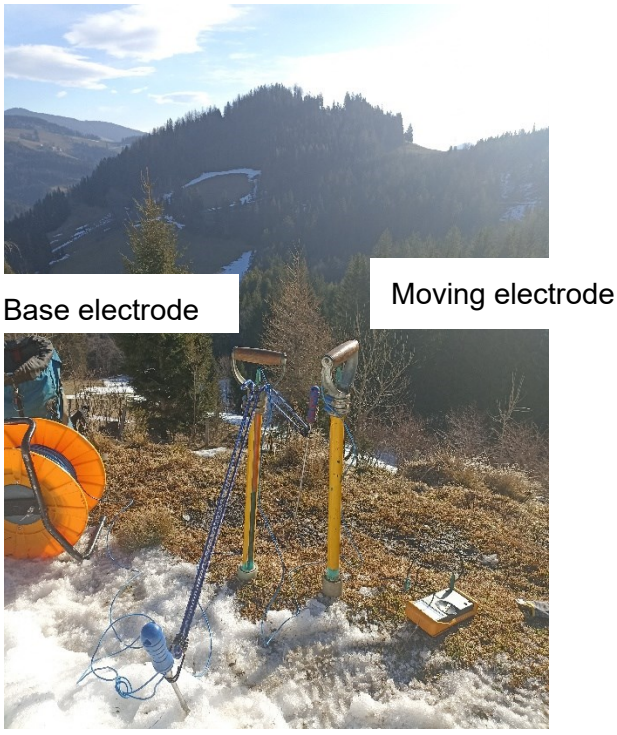

Figure 26: SP Base station with one fixed electrode as base and one moving electrode.

6.4 Geoelectric measurements

The system 4Point light 10W from Lippmann was used for the ERT and IP measurements (Figure 27a), where the current is injected as low frequency alternating current with a maximum amplitude of 100 mA. Up to 20 electrodes with a maximum spacing of 5 m can be connected to one cable segment, which results in a maximum length of 95 m per cable. The device was powered up by a 12 V battery and, to enhance the signal, a signal amplifier with a small build in battery was used. This amplifier was placed in the middle part of the profile between two cable segments. A ground electrode was placed at a distance of 10 m perpendicular to the profile. During the project, two profiles were measured in Wenner and Pole-Dipole arrays. For the Pole-Dipole array the remote electrode was placed at a distance of 300 m to the profile. All measurements are summarized in Tables 2 to 4. Because at every measurement also IP information should be gathered, the default system parameters for IP measurements were chosen. In difference to the standard setting, current electrodes which were part of the actual measurement are not used for the next ones. As a result, they have some time after the measurement to depolarize. Furthermore, for IP measurements, non-polarizable electrodes should be used. Like the SP electrodes, these electrodes contain copper sulphate to prevent polarization. However, due to the limited number of them, normal steel electrodes were in use and additionally a profile was done with both types of electrodes at the same position (Figure 27b), to verify the application of the normal electrodes. A lower measurement frequency should give the ground more time to charge up and results therefore in better signal quality. Because of the high time demand of low frequency measurements, a shorter profile was measured with 4 Hz and 1 Hz, to verify the application of 4 Hz. To get an accurate profile position, all electrodes were measured with the Trimble GNSS.

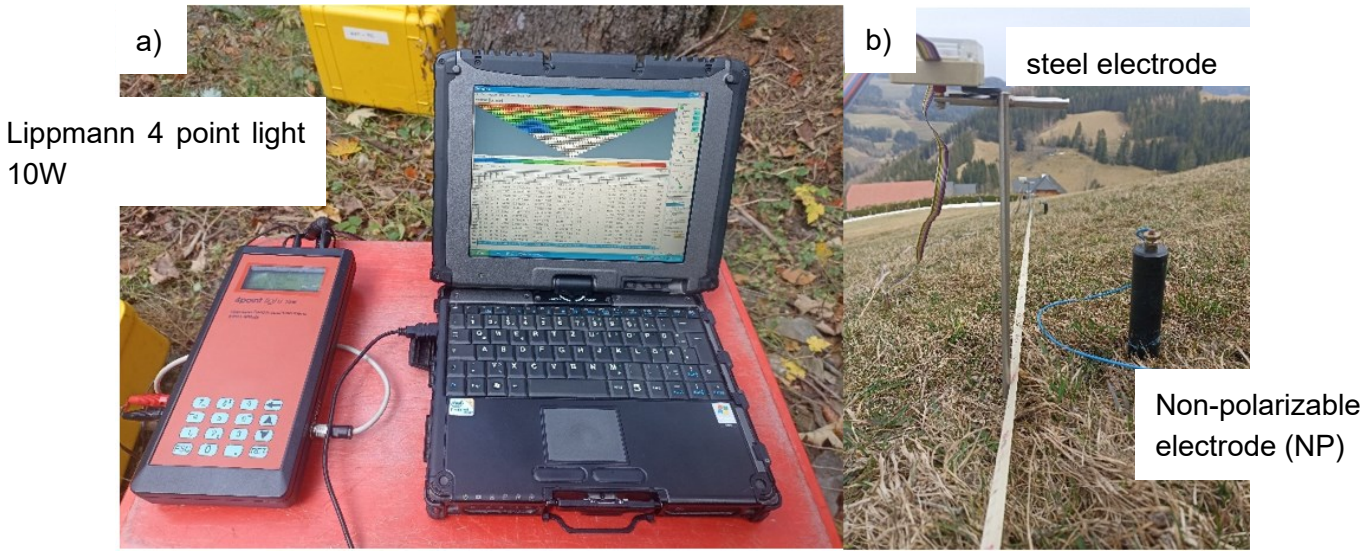

Figure 27: (a) ERT system Lippmann 4 point light 10W (b) steel electrodes connected to the system via cables and non-polarizable electrodes nearby.

Table 2:Settings of geoelectric profile 1

profile 1, south-east, 10.03.2023			
Measurement	w1_4ls	w2_1ss	pDp_4ls
Array	Wenner	Wenner	Pole-Dipole
Frequency [Hz]	4.16	1.04	4.16
Electrode spacing [m]	2	2	2
Profile length [m]	198	78	198
Contact resistance [kΩ]	1.4-12.2	1.8-12.2	1.3-12.1
Comment			Remote electrode at -300 m

Table 3: Settings of geoelectric profile 2

profile 2, north-west, 24.03.2023				
Measurement	w3_4ln	w4_4sn	w5_4sn	w6_1sn
Array	Wenner	Wenner	Wenner	Wenner
Frequency [Hz]	4.16	4.16	4.16	1.02
Electrode spacing [m]	3	3	3	3
Profile length [m]	297	117	102	102
Contact resistance [kΩ]	2.5-17.4	2.2-11.2	2-8	2.2-8
Comment			NP electrodes	NP electrodes

Table 4: Settings of geoelectric profiles from additional data sets

Field workshop profiles			
Profile	fw01	fw03	fw03
Date	11.04.22	14.10.22	14.10.23
Measurement	w7_add	w8_add	DpDp_add
Array	Wenner	Wenner	Dipole-Dipole
Frequency [Hz]	4.16	4.16	4.16
Electrode spacing [m]	4	1.5	1.5
Profile length [m]	316	109.5	109.5
Contact resistance [kΩ]	0.5-25.7	1-27.9	-
Comment			aborted

6.5 Sampling

For the “ground proof” of some anomalies, samples were taken for further analysis in the laboratory. A geological compass was used to measure the dip and azimuth of the sample, whenever it was possible. To preserve the orientation, lines at the edges of the compass and arrows, indicating the dip direction, were drawn on the sample (Figure 28).

Figure 28: Taking samples for a petrophysical analysis in the laboratory. Using a geological compass, the orientation of the sample can be transferred to the laboratory.

7 Paleomagnetic measurements

7.1 Sample preparation

The Paleomagnetic measurements were carried out in the laboratory of the Montanuniversität Leoben in Gams. For the analysis, samples taken in the field were cut into cubes with 2 x 2 cm. At each sampling point, between two and four samples were taken, and on average 10 cubes, called specimen, were made from each sample. This results in about 100 specimens, which were further analyzed in the laboratory. Additionally, for every sampling point at least one specimen, or small parts of it, were pulverized. These pulverized samples were then taken for the analysis of the Curie temperature and IRM analysis. The weight was measured from all specimens and from all pulverized samples. In Figure 29 specimens of some samples can be seen.

Figure 29: Specimens (2x2 cm) from different sampling points and pulverized samples in small bags.

In Table 5 the samples and the associated sampling points can be seen. Sampling point sp06 is not in the survey area but was taken from a known arsenopyrite mineralization close to the area to get information about the susceptibility.

Table 5:Overview of the taken samples and the corresponding sampling point.

Sampling point	Sample ID	Nr. of Samples	Nr. of Specimens
sp01	8	1	5
sp02	5,6,11,16	4	34
sp03	9,14	2	9
sp04	10,13	2	10
sp05	1,2,3,4	4	33
sp06	12	1	7

7.2 Susceptibility and Curie temperature

For the measurement of the susceptibility and for the determination of the Curie temperature the multi-function Kappabridge MFK1-FA from AGICO was used (Figure 30). Three susceptibility measurements per specimen were done to obtain representative results. For the Curie temperature, the pulverized samples were heated up to 720 °C with a heating rate of about 14°C per minute. After reaching the maximum temperature, the sample was cooled down to 40 °C, again with around 14 °C per minute. The operating frequency was set to 976 Hz and after each heating or cooling phase, the specimens susceptibility was measured. To ensure that included organics or carbonated samples do not burn at high temperatures, measurements were performed in Argon atmosphere.

Figure 30: Kappabridge MFK1-FA from Agico for measuring the susceptibility and the curie temperature.

7.3 Remanence

For the measurement of the orientation and strength of the remanent magnetism, the 2G SQUID (Superconducting Quantum Interference Device) Cryogenic magnetometer was used (Figure 31). By using liquid Helium inside a container sheathed with μ metal, magnetic moments with an accuracy of 10^{-10} Am^2 can be measured. The natural remanent magnetism was measured at almost all specimens. Only specimens, which were too large for the holder of the Cryogenic magnetometer or specimens with an uneven surface were not measured. If the specimens are orientated, the specimens were inserted in the Cryogenic magnetometer in a way that the top in the field is also the top in the device and the dip direction is parallel to the axis of the device. In addition, the isothermal remanent magnetism was measured on some pulverized samples. The artificial magnetic field needed for this measurement was applied by a Walker Scientific Inc. saturation magnet. The magnetization was done in steps up to a maximum field strength of 1450 mT. After each field increment, the sample was measured in the Cryogenic magnetometer. For the backfield measurement, the same steps were used but the magnetization was done in opposite direction, till the applied magnetization degraded.

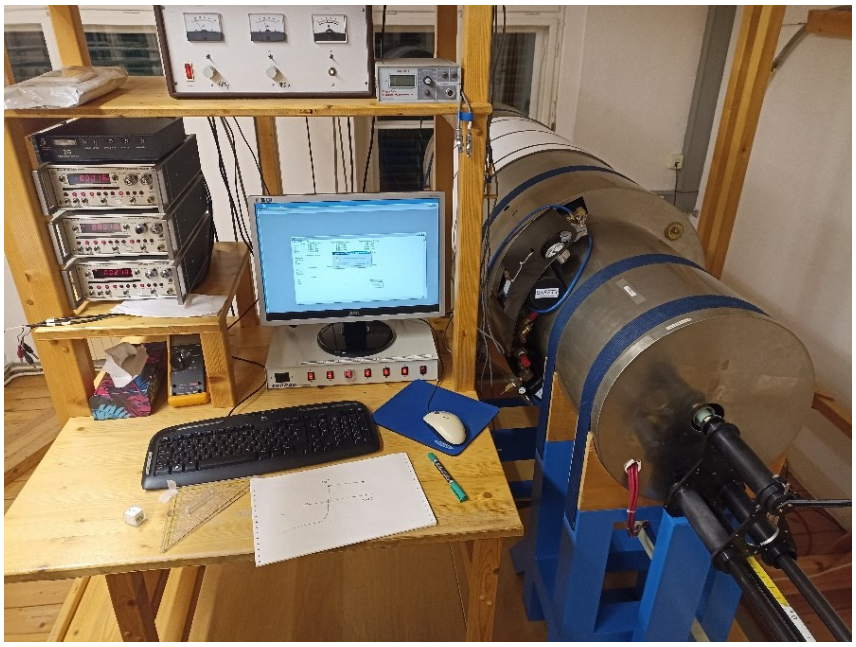

Figure 31: Cryogenic magnetometer 2G SQUID.

8 Data preparation, processing and results

8.1 Geomagnetic measurements

To interpret magnetic data, several reductions and corrections must be applied. The workflow for processing the magnetic data is shown in Figure 32. All correction steps were applied to the measured values of sensor T2.

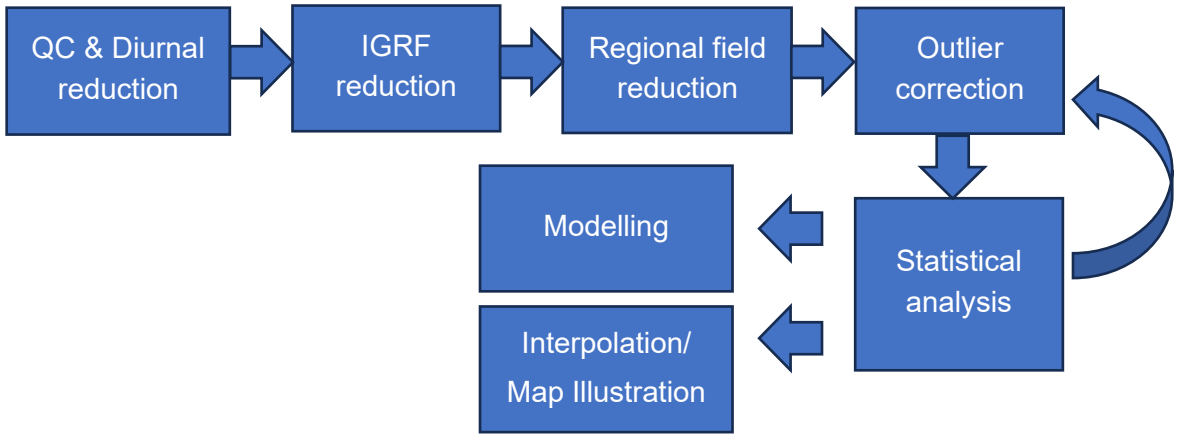

Figure 32: Workflow for the processing of magnetic data.

To obtain representative results, a quality control was done before the reduction steps. Measurements with a quality value lower than 6-6 were removed from the dataset. Furthermore, measured points with a gradient higher 1000 nT are clearly outliers and were also directly removed. This was true for 0.2 % of the data, what indicates a very good quality. Since magnetic measurements are absolute measurements, the diurnal variations must be subtracted. This was done by using the records of the magnetic base field from the Conrad observatory. The reduction was done in GEMlink, where the observed data was reduced by the corresponding base field value. After the reduction, the average base field for the corresponding time period of the measurement was added. In addition, to obtain the anomaly field, the regional field must be subtracted, which was done in two steps. First, the International Geomagnetic Reference Field (IGRF), which is a calculated representation of the regional field in a specific area, was used. These values were taken from the online ZAMG declination-inclination calculator, which calculates the total field strength for a specific day and location by using the IGRF model. For the calculation of these values, each profile was considered separately. In a second step, the values were imported to the software POTENT, where a more precise removal of the regional field can be done based on the measured data. This was necessary, because the regional effect is very strong in the western part of the area compared to the eastern part. Using a mathematical surface, one can remove the background values and thus the remaining regional field. After trying different surfaces, a first order polynomial surface was chosen. The necessary control points for the alignment of the surface were set on undisturbed data points in the east and west of the survey area. The steps of receiving the corrected values are summarized in the following equation.

Corrected Value = Measurement value - base value + datum - IGRF – regional field

In POTENT every profile was checked for outliers. This was done by comparing the magnetic intensity, as well as the gradient values of a data point with neighboring data points. Furthermore, field observations were used to identify possible faulty data points. Especially profile 18, which is partly located close to farm buildings, was showing a high number of outliers in this area. Also, data points close to huts, metal pipes or below power cables were identified as faulty measurements. In total, 2% of the data was removed during this outlier detection process, which is a good result. To verify, if most of the faulty measurements are deleted, a boxplot analysis was carried out (Figure 33). Overall, the variability of the data within the profiles is small and the median value is close to zero. If more data points are outside the Whiskers but close to each other, it is most likely due to a strong anomaly and they can be seen as correct measurements. This can be observed at profiles 2, 3 and 5, where values above 1000 nT, which are occur in positive and negative, can be explained by strong anomalies and are not related to faulty measurements. Still some stand-alone outliers, like in profile 20 and 18 occur, but after rechecking these values again in POTENT, they represent peak values from anomalies and are therefore also correct measurements.

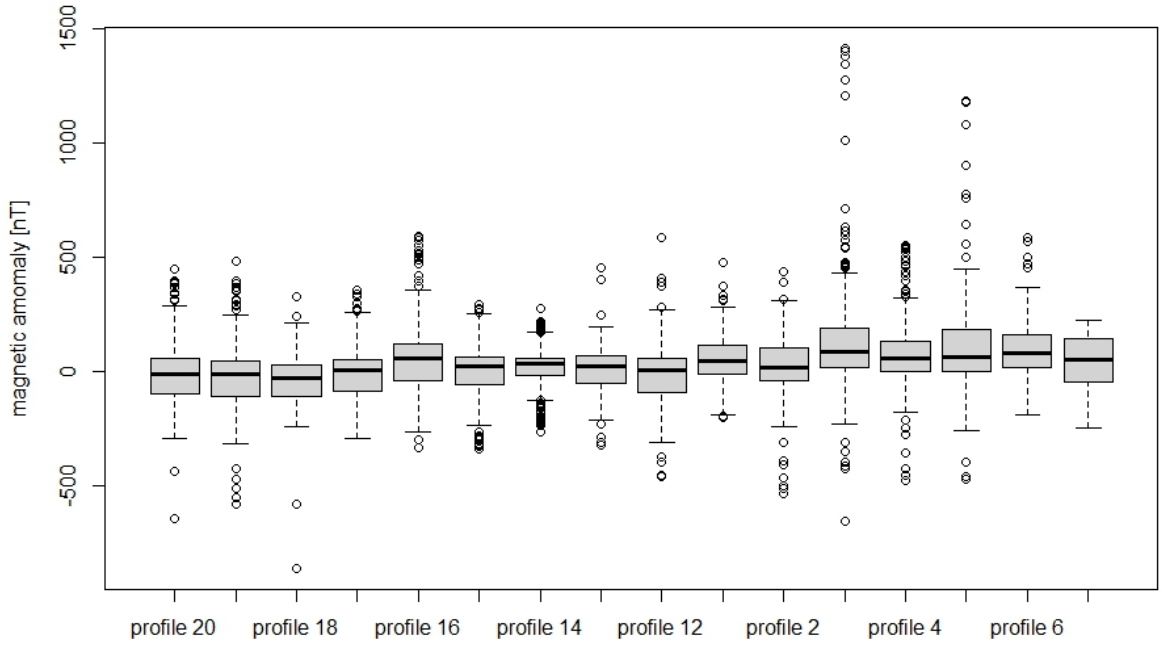

Figure 33: Boxplot diagram of the individual magnetic profiles.

To also evaluate the success of the regional field subtraction, the gradient was plotted against the magnetic anomaly (Figure 34). If the intercept value would be zero, the regional effect is completely gone. The corrected data shows an intercept value of -2.76, which is close to zero and therefore the regional field can be seen as removed.

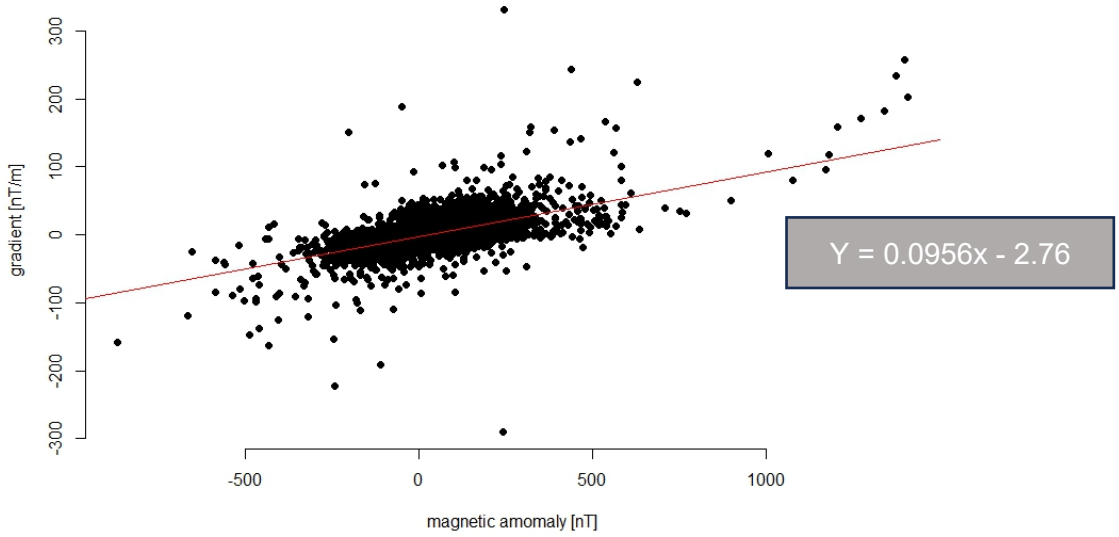

Figure 34: Scatter Plot of the gradient against the magnetic anomaly field to verify the reduction of the regional field. A linear trend line is shown in red with the corresponding equation.

The interpolation of the corrected magnetic data was done in the Software SURFER. Several gridding methods like Kriging, Inverse Distance to a power and Radial Base function, were used to get the best result, which is also geologically meaningful. Within the different griding methods, several parameters like the search radius and anisotropy values were tested. Due to the strong topography in the survey area, magnetic anomalies which are clearly related to each other, are showing very different magnetic intensities in the different profiles. As a result, a geological meaningful interpolation map could not be created. Therefore, the corrected values were plotted in QGIS in a para view plot. In general, magnetic anomalies show values between plus and minus 1000 nT. Just in some rare cases, the anomalies exceed these values. In the very east of the survey area, only very small changes in the magnetic anomaly field occur. Towards the west, roughly from the hanging wall of the Pramerkogel formation, the magnetic anomaly field is strongly increasing before it flattens out again in the carbonates of the Hochschlag formation. The main magnetic anomaly zones are therefore in the Weitzbauer formation. However, there are some isolated anomalies, but also some anomalies that can be tracked across multiple profiles like in the south-east of the survey area. Figure 35 represents the reduced magnetic anomalies as curves but also as color coded points. For better visualization, the curves were limited to plus and minus 800 nT. The color subdivision was chosen according to the data distribution.

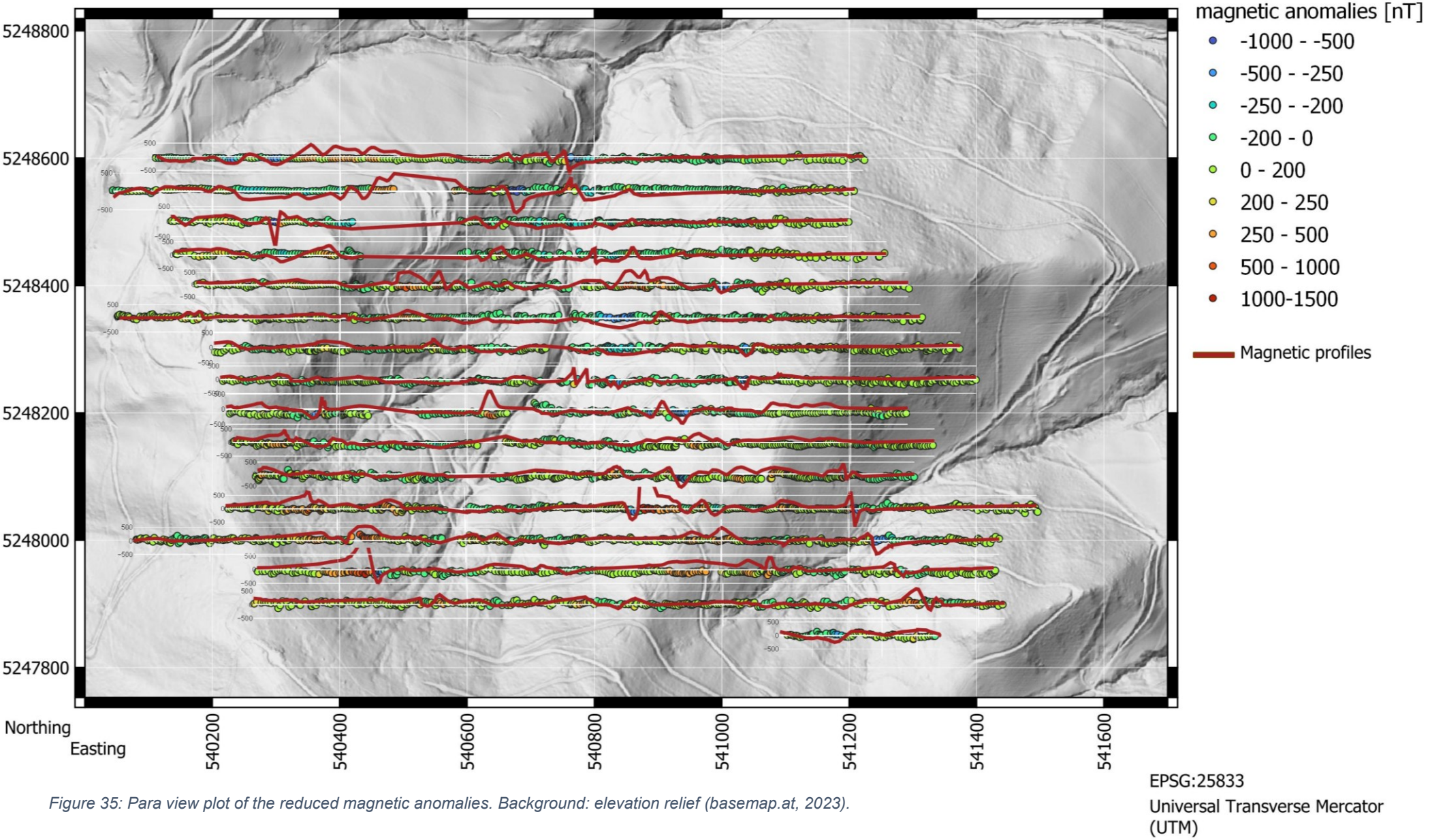

Figure 35: Para view plot of the reduced magnetic anomalies. Background: elevation relief (basemap.at, 2023).

The modelling of the magnetic bodies was realized in the software POTENT. Different bodies like dykes, prisms, lenses and cylinders were used to explain the measured anomalies. In a first step, the profiles were considered separately and small bodies were created for each anomaly in a profile. Later, these small bodies were extended and connected, if possible. Figure 36 illustrates a magnetic body which describes the measured anomaly.

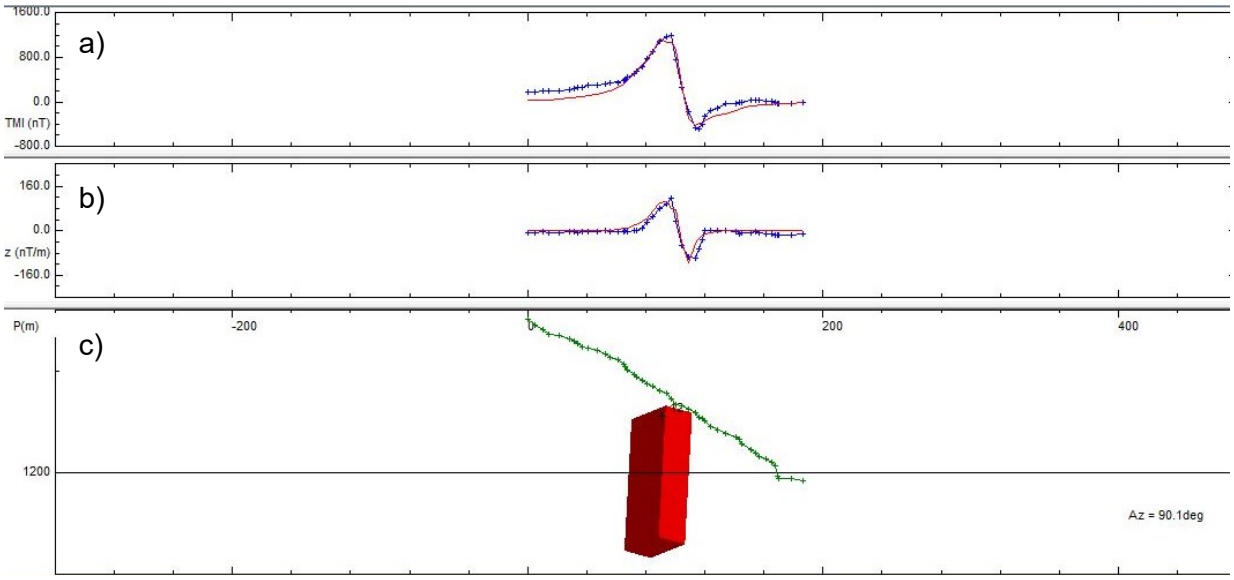

Figure 36: Model of a magnetic body in POTENT. The blue line represents the measured data and the red line the response of the magnetic body (a) reduced magnetic anomaly (b) magnetic gradient (c) modelled magnetic body with topography points (green).

8.2 SP measurements

The data preparation for the SP method is relatively simple, because the first quality control was already done during the measurement. If measured points were differing significantly from neighboring points, another measurement was done to confirm or to overwrite the point. If the value was confirmed but differed strongly from the last measured point, an intermediate point was measured to increase the resolution. After the digitalization of the measured values, some corrections must be applied to get to the final result. When the two electrodes are just a few centimeters apart, a zero potential should be measured. This was mostly not the case, but up to 10 mV base drift, which was the case for all base station readings, it was seen as neglectable, because the measured anomalies are mostly a few hundred millivolts. Only the base drift of the first station was removed to get a starting value of zero mV. Afterwards the measured difference to the zero point must be added. Since the base station was always on the new profile and the moving electrode was located on the already measured profile, the sign of the zero point difference must be changed. After moving the base station, additionally the measured value between the two base stations must be added. This procedure can also be seen in Figure 37 with an example.

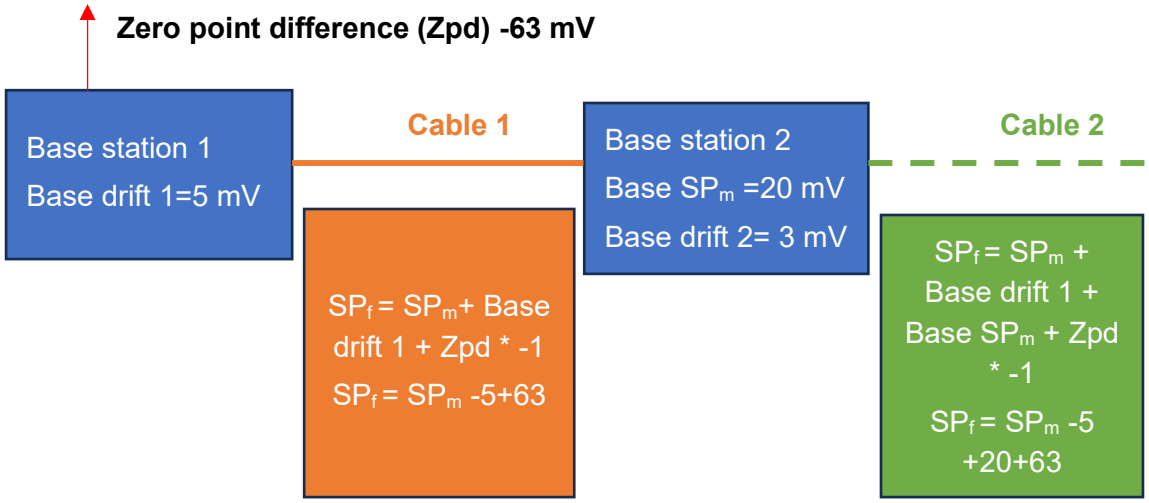

Figure 37: Processing workflow with example for the SP data. SP_f = SP value final, SP_m = SP value measured, Zpd = zero point difference.

After the processing of the SP data, a statistical analysis was carried out to verify the quality of the corrected values, what was done using a boxplot diagram (Figure 38). The individual profiles show that the median is generally close to zero, what indicates that the selected zero point does not fully reflect the actual zero potential. Nevertheless, it is also not far away from the real zero potential and can be used further. The profiles do not differ much from each other in terms of variability and median. Outliers in the Boxplot diagram are due to narrowly defined anomalies and not related to erroneous measurements. This was already proven in the field. After the corrections, the values were plotted according to their coordinates again in a Para view plot done in QGIS.

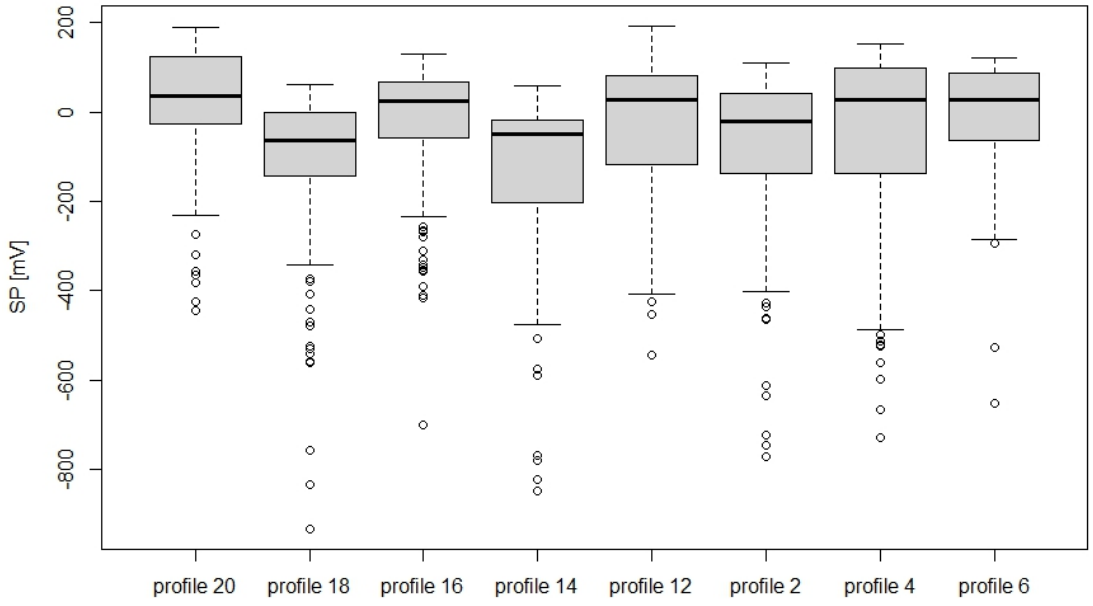

Figure 38: Boxplot diagram of the corrected SP data for the individual profiles.

In the results of the self-potential survey, several anomalies can be seen in the survey area. Anomalies with a great potential drop can be observed more in the western part of the area, whereas in the eastern part mostly smaller ones occur. In the western part, the anomalies show an expansion of around 50 m in the east-west direction and are separated by 50 to 100 m. They are in general following a north-west to south-east trend and therefore also following roughly the geological strike. After a sequence of five to six strong anomalies with up to -1000 mV, the potential values are more stable again in most of the profiles. Only in the southern profiles, high potential drops can also be seen till the eastern end. Even if the anomalies towards the east are smaller compared to the before mentioned ones, they still can reach up to -250 mV. Up to six anomalies can be identified in this zone, where the orientation is similar to the big anomalies in the west. After some thinner anomalies, in the very east a broad anomaly can be identified with an extension of around 100 m in the east-west direction. Figure 39 shows the measurement result as curves and as crosses with color coding. The potential values which are positive relative to the zero point, were summarized to one single color.

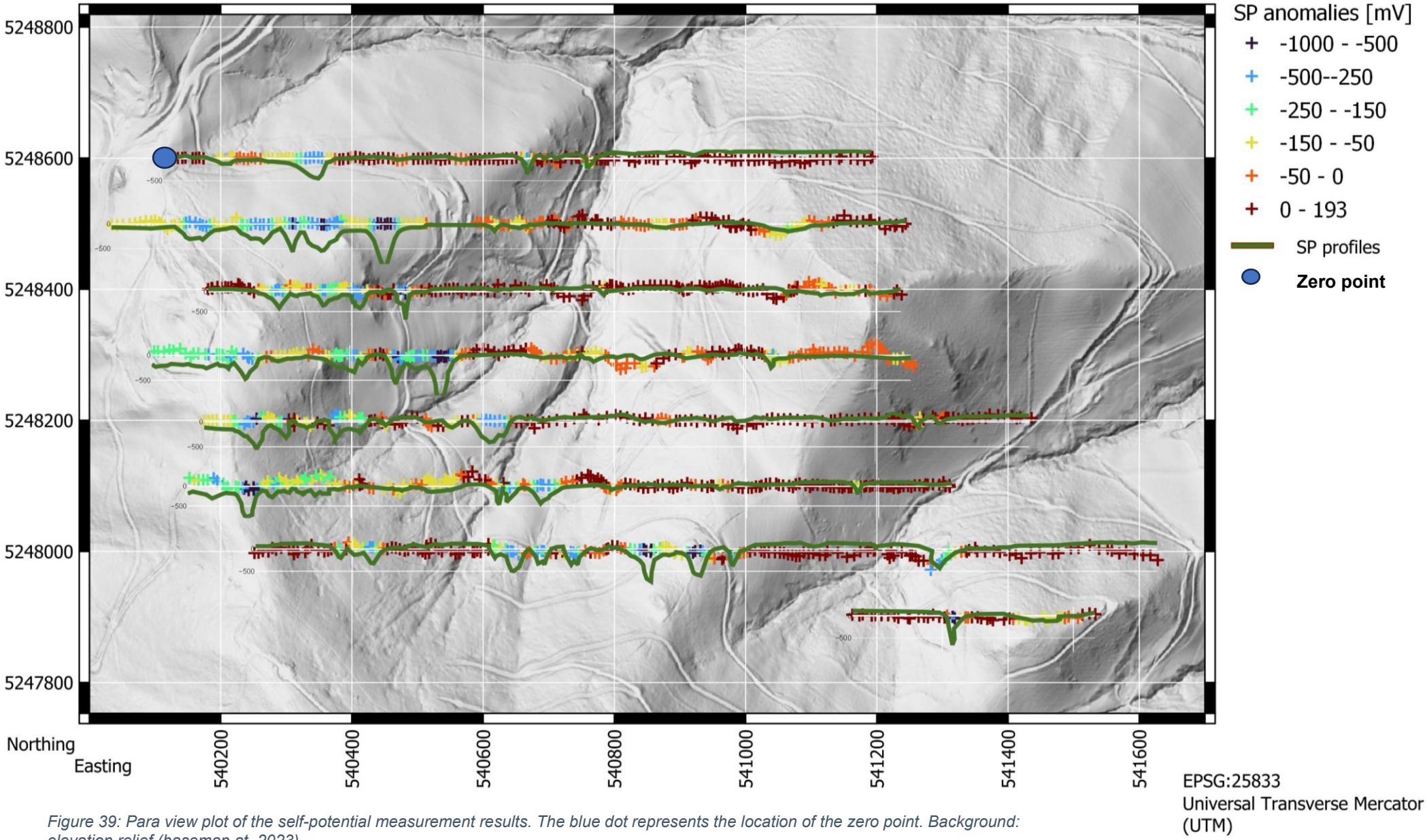

Figure 39: Para view plot of the self-potential measurement results. The blue dot represents the location of the zero point. Background: elevation relief (basemap.at, 2023).

8.3 Geoelectric measurements

For the evaluation and interpretation of the results, some processing steps are needed as shown in Figure 40. After a raw data analysis, topography information must be added to the data file, which is then imported in RES2dINV. In the software, another quality control was done before the inversion, which was repeated after removing outliers according to the Root Mean Square (RMS) error statistics to optimize the result.

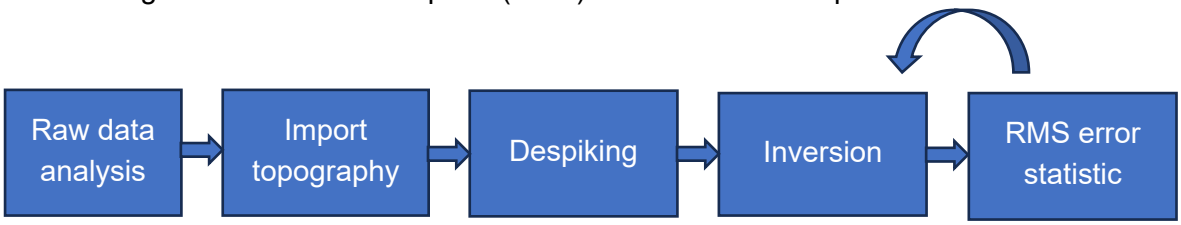

Figure 40: Workflow for processing geoelectric data.

In the raw data analysis, the quality of the data must be assessed and outliers removed, if necessary, as these could falsify the results. Measurement points with an error dU of more than 2 % were defined as poor quality data. This error dU is calculated directly by the instrument from the standard deviation, the average value of the apparent resistivity and the number of repeated measurements. Each individual measurement is repeated between three and six times, depending on the quality of the data. Table 6 summarizes the number of erroneous measurements, where data points with high dU and negative resistivity values were removed. Negative values from the IP measurement were set to zero, but not deleted completely because the resistivity measurements can still be used. Measurement w1_4ls is the only one which shows negative resistivity values. This appeared most likely due to an erroneous cable connection between the last segments. If electrodes B and N are in this section, the results are partly not reliable. Interestingly, after this first measurement, the problem was solved without changing the last segments. However, in all measurements, less than 6 % of the data were removed what can be considered as a good result.

Table 6:Number of erroneous measurements from the ERT.

Measurement	Nr.Datapoints	dU > 2 [%]	Rho < 0 [Ωm]	Phi < 0 [mrad]	Removed [%]
w1_4ls	1617	20	55	15	4.64
w2_1ss	247	0	0	11	0
pDp_4ls	2450	44	0	6	1.80
w3_4ln	1617	86	0	25	5.32
w4_4sn	124	2	0	1	1.61
w5_4sn	187	5	0	0	2.67
w6_1sn	187	2	0	10	1.07

After the removal of the erroneous data points, a boxplot diagram was created for the apparent resistivity and induced polarization values of every measurement (Figure 41).

For measurements within the same profile and same length, the distribution of the apparent resistivity values is very similar. The shorter measurements were carried out above anomaly zones and therefore gave different values than the longer measurements. From measurement w3_4ln, it can be already concluded that the overall resistivities of profile 2 are much lower compared to profile 1. A significant difference between resistivity measurements using non-polarizable electrodes with a frequency of 1 Hz and 4 Hz (w5_4sn & w6_1sn) and the measurement using normal steel electrodes and 4 Hz (w4_4sn) cannot be seen. In the boxplot diagram of the phase angle, some outliers appear, especially in the longer profiles. This can be related to the higher amount of data and the larger distances of the dipoles compared to the shorter measurements. The variability of the data is still in a very narrow range and the occurring outliers will be removed later using the Root mean square statistics (RMS) after the inversion. In profile 2, higher polarization values can be observed compared to profile 1. Comparing again the measurements with and without NP electrodes, the median does not differ significantly. However, the phase angles are slightly higher at a lower frequency.

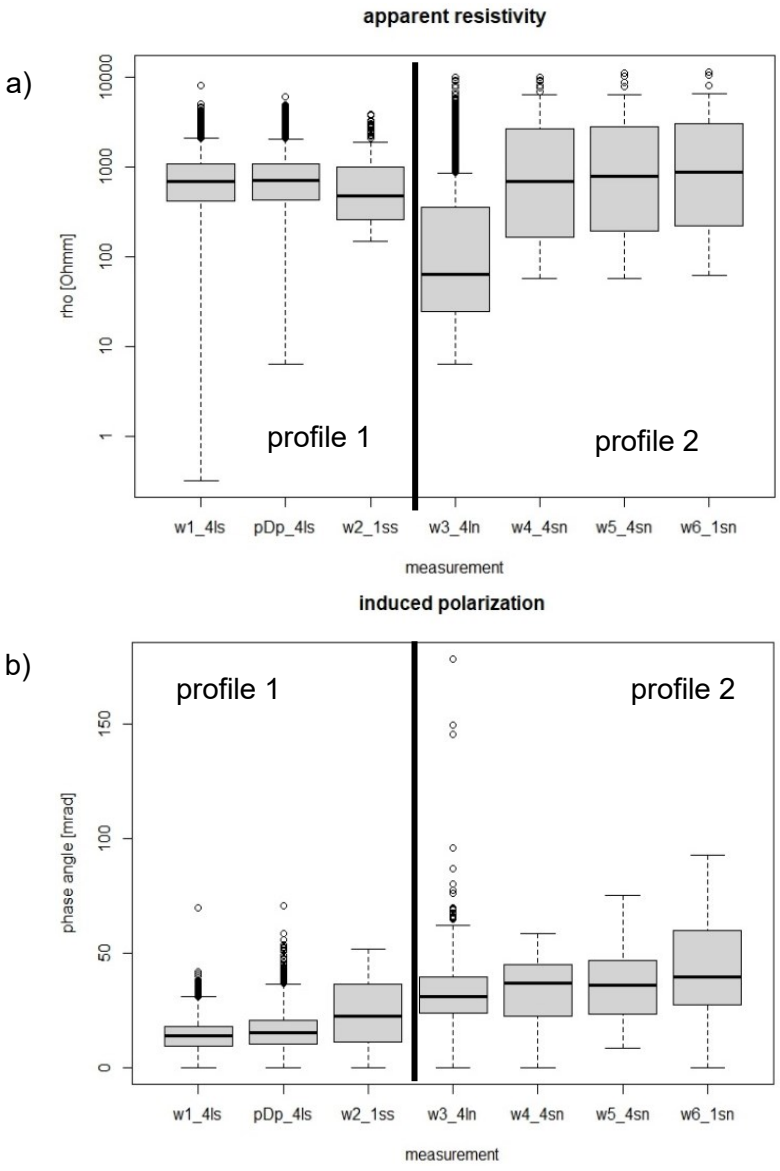

Figure 41: Boxplot diagram of the corrected values from the geoelectric measurements. (a) apparent resistivity (b) phase angle.

The corrected datasets with additional topography information from the GPS measurements were then imported into the software RES2dINV, in which the further processing and inversion was done. Before the inversion, the data were checked for spikes. These spikes are defined as apparent resistivity values, which do not fit to the neighboring points, what would again lead to an erroneous model. All data showed no, or just a few spikes, which were removed directly in the software. In the next step a first inversion was carried out with the default inversion parameters. These parameters were then refined to obtain a better result with a lower iteration error, which describes the difference between the measured and computed values. Therefore, the root mean square error statistic was also used after the inversion to remove possible outliers directly. In addition, the geological plausibility of the model was reviewed. The final model was calculated using finite elements, which is more suitable for models with topography included. The electrode spacing was set to half of the real spacing, to get a more detailed inversion result and side effects, which can occur on the borders of the model, were slightly reduced. These effects could appear due to two reasons. Firstly, a real anomalous body is close to the border of the model, or secondly it is an artifact which is needed to describe above laying values in the model. To differentiate between these two cases, models were calculated with and without extension. Bodies which can be seen also in the extended model are most likely real anomalies. Due to the higher amount of information, the extended models were preferred. It must be mentioned that the extension area is purely calculated and does not show measured values. All inversion parameters can be found in Appendix A1. Figure 42 shows a complete inversion result of measurement w3_4In without topography. The top section describes the measured apparent resistivity followed by the second section with the calculated resistivity values. Both sections are pseudo sections which do not represent the true depth. In the third section the resulting inversion model in true depth can be seen. The last section represents the inversion result for an extended model. In difference to the model without extension, the bottom area of the model is described by only values below 10 Ωm. This is geologically questionable and therefore, for this measurement, the model without extension will be used for further interpretation. For a better illustration of the inversion model, it was exported to the software SURFER. Here a grid file is needed to interpolate the inversion model. This was done with the gridding method Triangulation with linear interpolation. To get a smooth result, the number of nodes suggested by SURFER were multiplied by 10. For better comparability, a common color scheme was used for all inversion models, using a logarithmic scale for the division of the resistivity values and a linear scale for the phase angles. The inversion models from the comparison of the IP measurements with the different frequencies and electrode types can be found in Appendix A2. In addition, the inversion models from the measurements conducted during the geophysical field workshop can be found in Appendix A3 and A4.

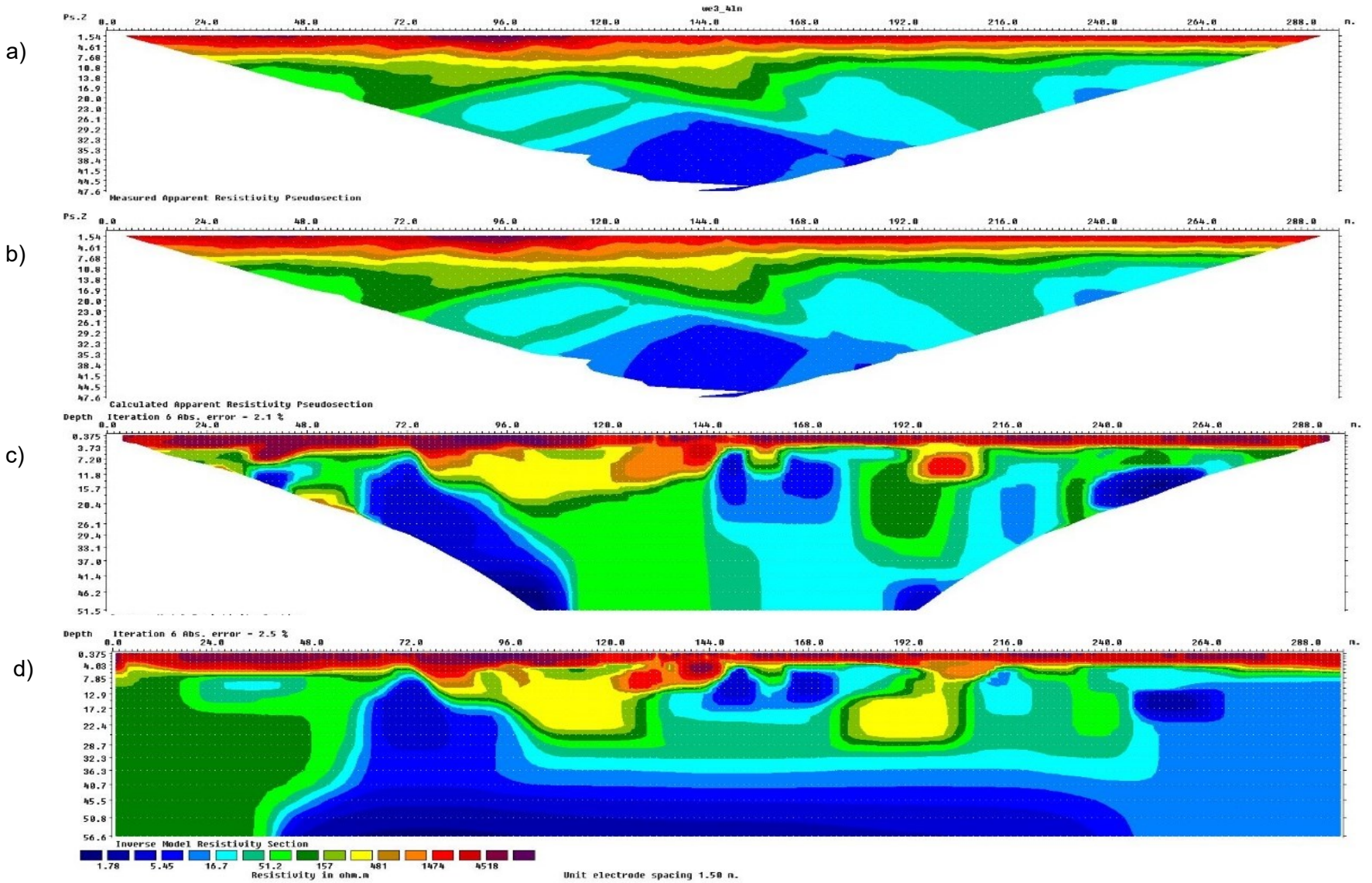

Figure 42: Full inversion result of measurement w3_4ln. (a) measured apparent resistivity values. (b) calculated apparent resistivity values (c) final inversion model (d) final model with model extension.

8.3.1 Inversion model of profile 1

After 6 iterations, the final model for the Wenner measurement of the southern profile was obtained with an iteration error of 3.2 % for the resistivity and 1.8 % for the phase angle (Figure 43). In general, most resistivity values range between 1000 Ωm and 3000 Ωm. Only close to the surface, the resistivities exceed 5000 Ωm. These high values can be related to the weathering zone of the soil. The lower resistivities, which interrupt this weathering zone between profile distance 90 m and 116 m, can be explained, due to field observations, by surface water. A few low resistivity anomalies with values lower than 100 Ωm can be seen, where most of them show an overburden of 20 m. Only in the western part of the profile, a low resistivity anomaly is reaching almost to the surface. Further west, towards the end of the profile, the resistivity values are lower compared to the east. Overall, the borders between low and high resistivities are very sharp and almost vertical. Low phase angles prevail in the profile, where towards west a slight increase can be observed. Only one lense shaped anomaly can be identified around profile distance 155 m. Here, phase angles up to 70 mrad could be measured close to the surface. The location of this anomaly is in arrangement with the low resistivity zone at 155 m.

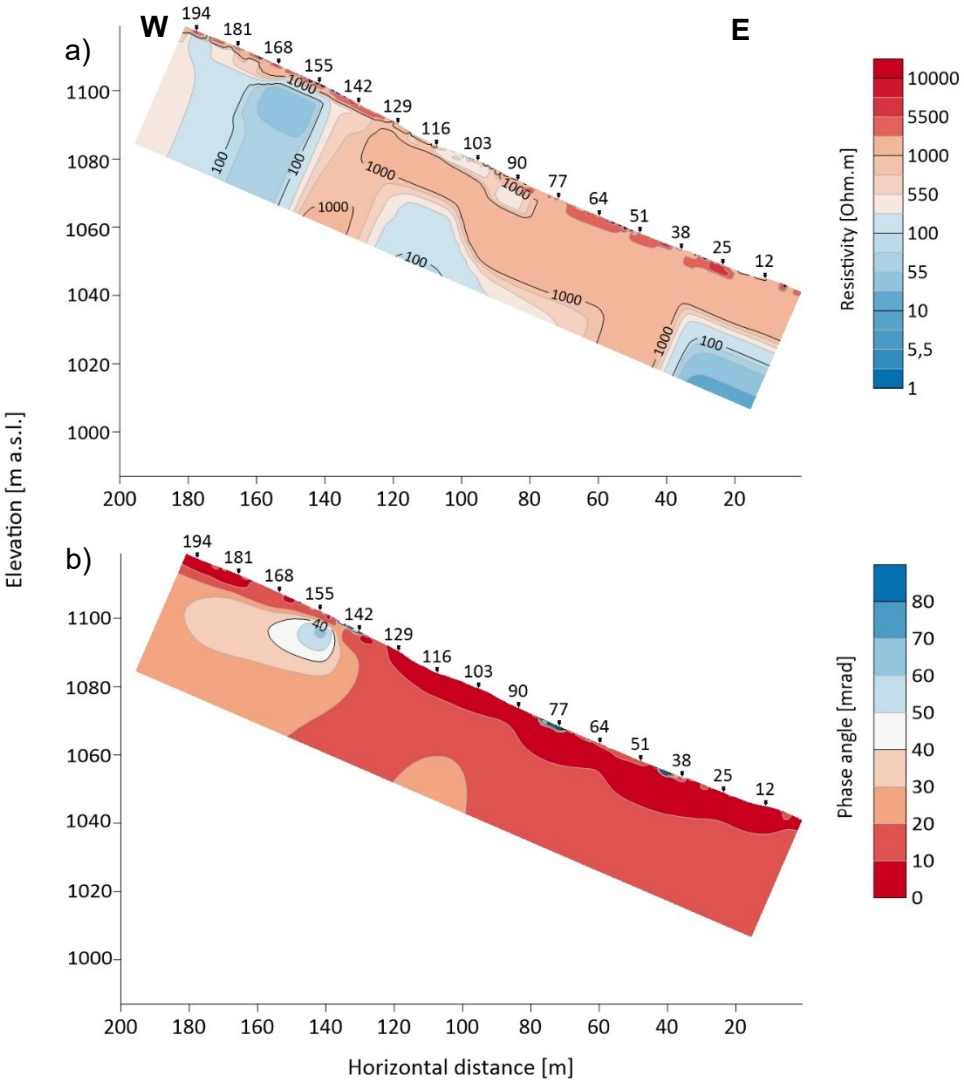

Figure 43: Inversion results of geoelectric profile 1. (a) Resistivity model of measurement w1_4ls (b) IP model of measurement w1_4ls. The profile distance is plotted on top of the models.

A penetration depth of 60 m could be reached with the Pole-Dipole measurement and therefore more depth information could be gathered compared to the Wenner measurement. After six iterations, the error of iteration was 2.4 % for the resistivity and 2.5 % for the phase angle. The already described zones of low resistivities can also be observed in the model of this measurement (Figure 44). Between profile distance 105 m and 130 m, a zone of higher resistivities can be seen, where the highest values were measured in greater depths. The measured phase angles show two areas of enhanced values. Around profile distance 155 m, the already mentioned anomaly and another anomaly at profile distance 60 m. This anomaly shows phase angles up to 40 mrad, an overburden of about 25 m and is also located in a zone of lower resistivities. One must mention that deep data points in the model must be treated with caution. Due to the low injection current, deep IP values can be faulty. Depending on the inversion parameters, size, strength, and location of the anomaly vary significantly.

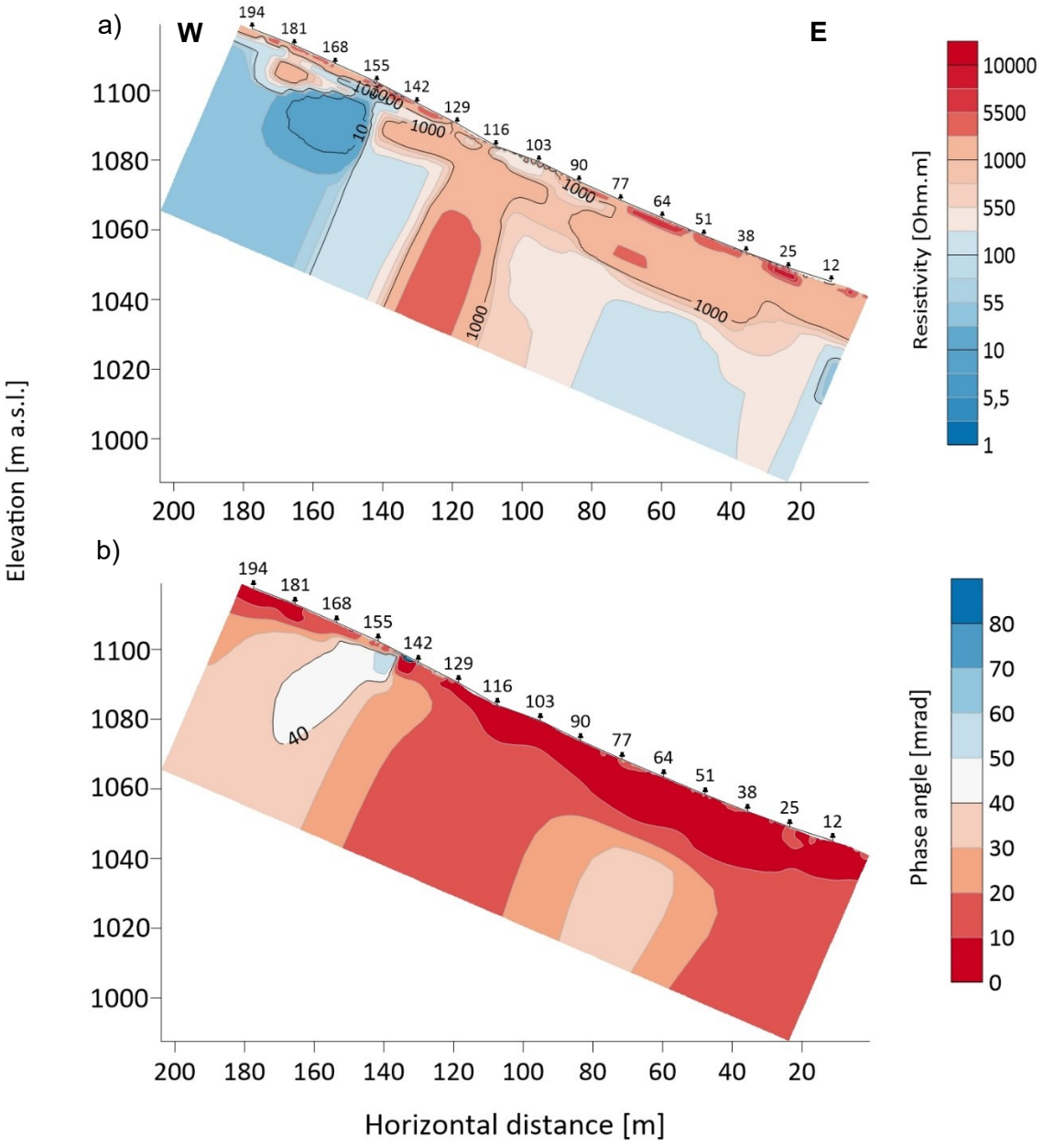

Figure 44: Inversion results of geoelectric profile 1. (a) Resistivity model of measurement pDp_4ls (b) IP model of measurement pDp_4ls. The profile distance is plotted on top of the models.

8.3.2 Inversion model of profile 2

The final model could be calculated with six iterations, where the iteration error for the resistivity is 2.5 % and for the phase angle 5.8 % (Figure 45). In general, the resistivity values of profile 2 are low, where mostly the uppermost meters in depth showing resistivities higher 1000 Ωm. This high resistivity layer can be observed along the whole profile and is again related to the weathering zone of the soil. Below this layer, resistivities lower than 100 Ωm prevail. Along the profile, three anomaly zones of very low resistivities can be found, which show values lower than 10 Ωm. The largest anomaly is in the eastern part of the profile. Here values below 10 Ωm can be seen not only close to the surface, but also in greater depths. Another anomaly is in the middle part of the profile between 135 m and 195 m. This zone shows two centers of low resistivities which are close to the surface. To the west and to the east of the anomaly, two zones of higher resistivities appear. Here resistivities higher 100 Ωm reaching in a depth of 25 m. A small rectangular shaped low resistivity anomaly is in the western part at profile distance 252 m in a depth of 12 m. In the model of the phase angle, a few lense shaped anomalies could be detected. All of them are close to the surface and show two centers of maximum polarization. At the beginning of the profile the largest zone appears, which can be followed to a depth of 30 m. Between 150 and 190 m another very shallow anomaly could be measured. After a small area without significant phase angles, again an IP anomaly appears with two independent centers. The last zone of enhanced phase angles is at the western edge of the model. In general, high IP anomalies are in areas of low resistivities, zones of almost no polarization are located in areas of higher resistivities.

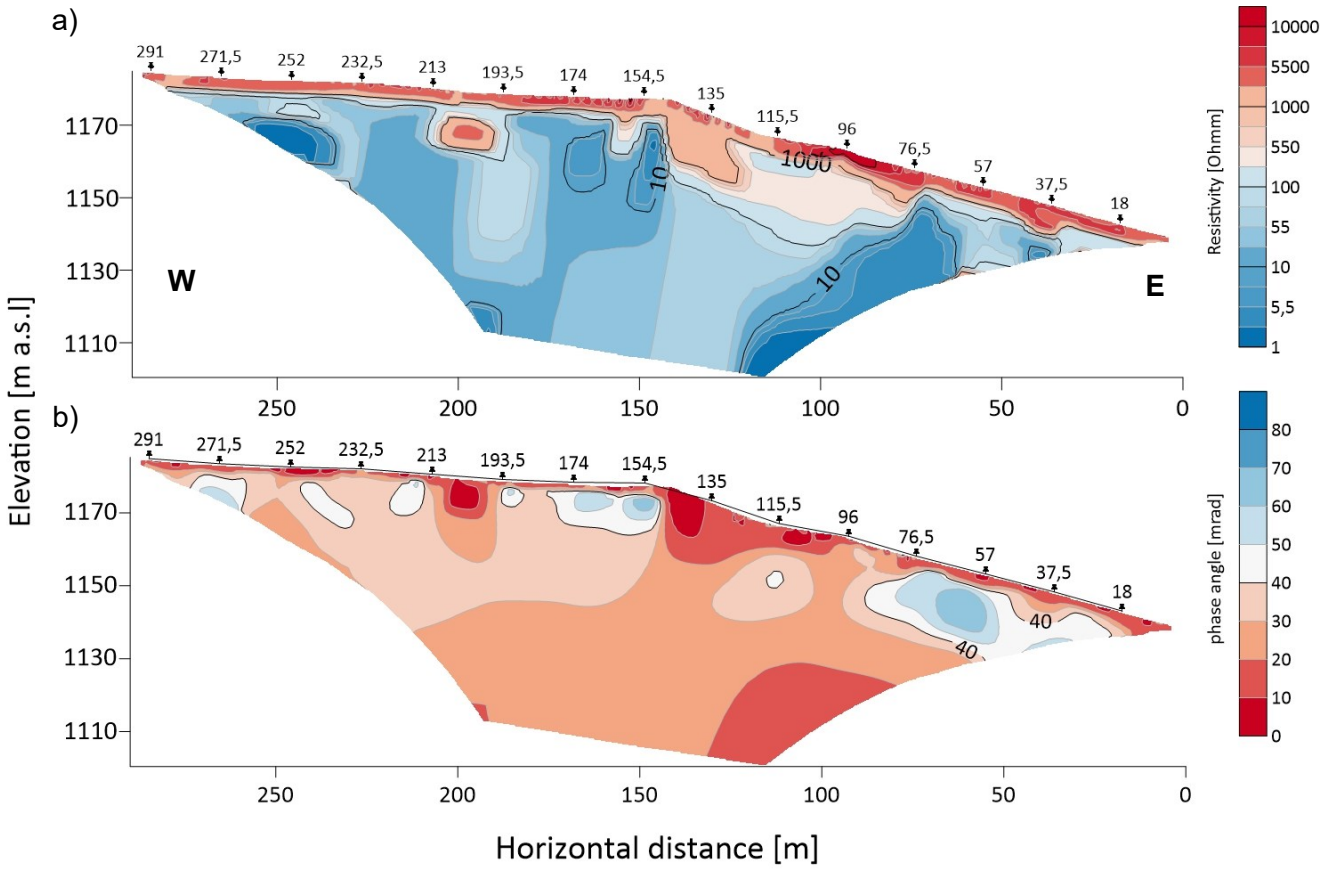

Figure 45: Inversion Results of geoelectric profile 2. (a) Resistivity model of measurement w3_4ln (b) IP model of measurement W3_4ln. The profile distance is plotted on top of the models.

8.4 Paleomagnetic measurements

8.4.1 Susceptibility

The three measured susceptibility values per specimen were averaged. Since the measured values were related to a volume of 10 cm^3, a recalculation by using the sample weights and the average crustal density (2.63 g/cm^3) was needed, because the specimens differ from 10 cm^3. The variability and median values of the susceptibility from the samples can be seen in the boxplot diagram (Figure 46). The mean values can be found in Table 7. In difference to sampling point 2, which shows a high variability, the others show a low variability and no outliers. The highest susceptibility values could be found in specimens from sampling point 5 followed by sampling point 4.

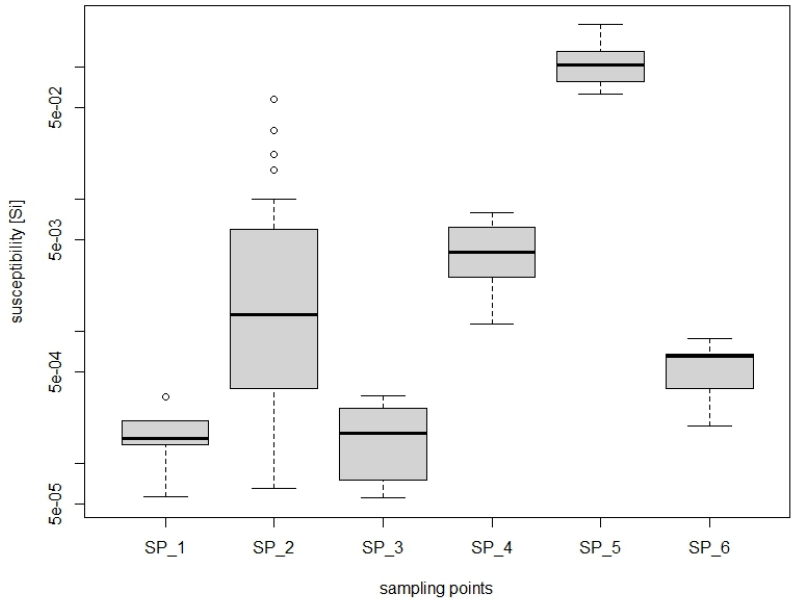

Figure 46: Box plot diagram of the bulk susceptibility in a logarithmic scale of all taken samples grouped according to the sampling point.

8.4.2 Natural remanent magnetism (NRM)

Using the Software REMASOFT 3.0 from AGICO, the gathered remanence data was plotted in a Wulff net (Figure 47) for illustrating the declination and inclination directions. In addition, the mean value and the statistical alpha 95 value are also plotted in the net (pink circles). For sampling point 1, an inclination of 137 ° and a declination of -7 ° could be defined with an alpha 95 value of 5.9 °. An inclination of 313 ° and a declination of 37 ° with an alpha 95 of 8.9 ° was observed for sampling point 5. For sampling point 2 no preferred orientation of the NRM was observed.

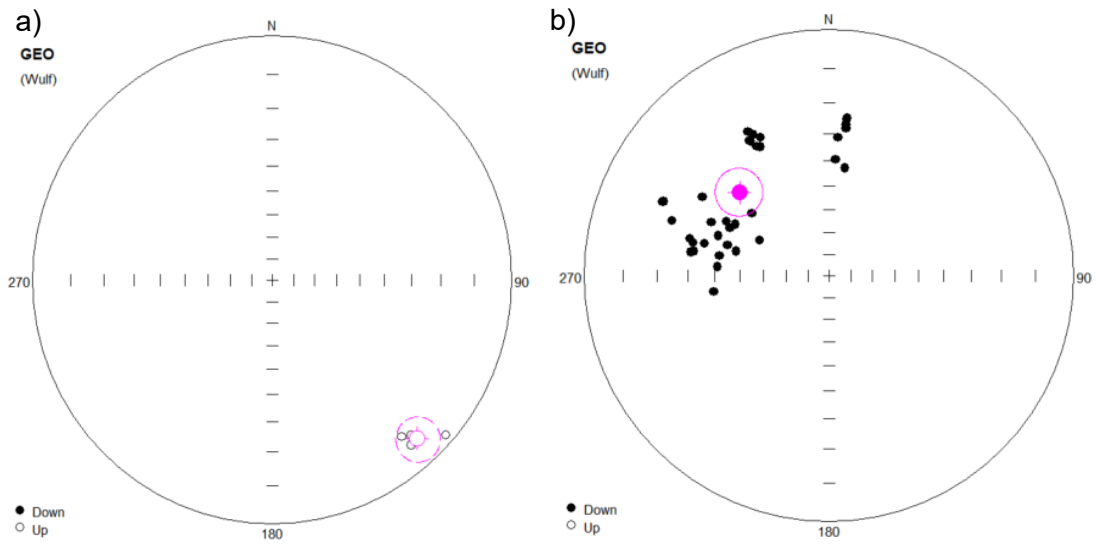

Figure 47: Result of the NRM analysis from (a) sampling point 1 (b) sampling point 5. Data points are marked in black and mean (inner circle) and alpha 95 (outer circle) are marked in pink.

The natural remanent intensity was measured on almost all specimens and averaged for every sampling point (Table 7). A detailed table for every specimen can be found in Appendix B1.

Table 7:Summary of the sampling points and the corresponding bulk susceptibility and magnitude of the natural remanent magnetism.

Sample point	SP_01	SP_02	SP_03	SP_04	SP_05	SP_06
Bulk susceptibility mean [E^-3]	0.18	5.63	0.17	4.7	116.73	0.55
Magnitude NRM mean [A/m]	0.0064	0.21	0.0025	0.3	1.32	0.0005

8.4.3 Curie temperature

For the analysis of the Curie temperature, the Software CUREVAL 8 from AGICO was used. By plotting the measured temperature against the bulk susceptibility at this temperature, one can determine the Curie point of the specimen. Two methods called tangent method and Curie Weiss method exist for this determination. In the tangent method, Curie temperatures are often overestimated and therefore, the Curie Weiss method was preferred. Nevertheless, for some specimens the Curie Weiss method was not reliable, and the tangent method was used. In difference to the tangent method, the Curie Weiss method uses the reciprocal value of susceptibility. A linear rise from the horizontal (ferromagnetism) indicates the transition to paramagnetism and therefore the Curie temperature. Figure 48a shows the principle of the Curie Weiss method, where at the crossing of the black line with the zero line the Curie point can be found, which is at 620 °C for this example. The tangent method can be seen in Figure 48b.

The susceptibility of the ferromagnetic minerals is heading to zero if the Curie temperature is reached. By using a tangent and fitting it to the observed heating curve, the Curie point can be found at the crossing from the tangent with the x axis. In this example the Curie point is at a temperature of 610 °C. Both methods deliver a suitable result and can be applied for this specimen. The determined Curie points of all measured specimens can be found in Table 8.

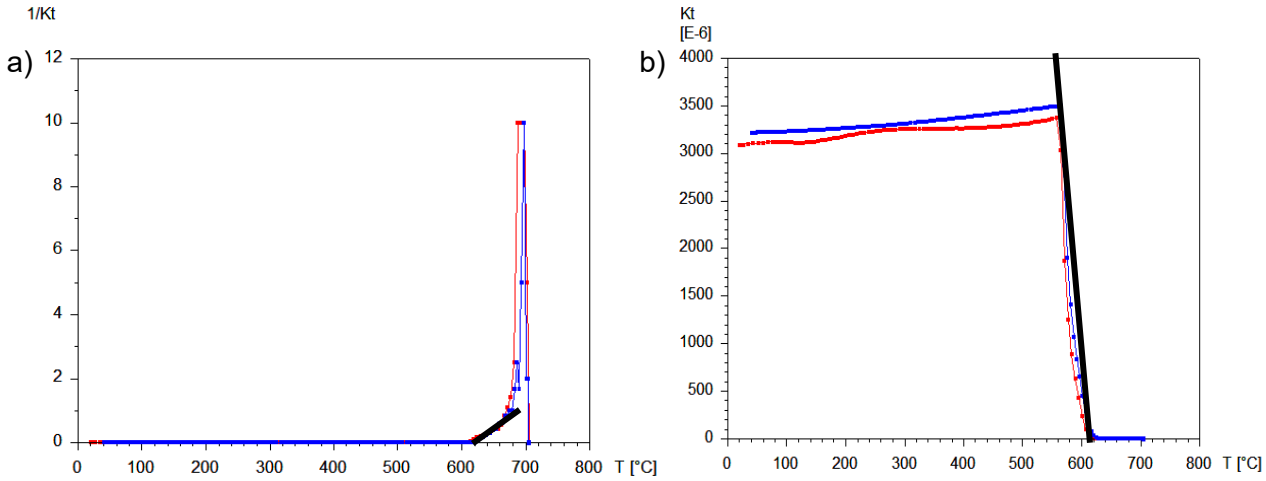

Figure 48: Determination of the Curie point with different methods in the Software CUREVAL 8 from the specimen P04_2. (a) Curie Weiss method (b) Tangent method. The red line represents the heating and the blue line the cooling curve. The black line indicates the tangent for determining the Curie point.

8.4.4 Induced remanent magnetism (IRM)

For the evaluation of the IRM results, an excel sheet named IRM-CLG 1.0 from Kruiver et al. (2001) was used. As input data, the applied field strength and the measured magnitude of the remanent magnetism were used. By adjusting the saturated IRM value (SIRM), the mean coercivity and the half width of the distribution, a fitting curve can be designed, which describes the measured data. Up to six different components are supported in this sheet. Furthermore, three different fitting curves are available (Figure 49), which should support each other. The Linear Acquisition Plot LAP, the Gradient Acquisition Plot GAP and the Standardized Acquisition Plot SAP are available, whereby the focus during the fitting procedure was on the Linear Acquisition Curve. In addition, statistics like F test and T test can be used to refine the result. In most of the specimens only one low coercivity mineral component can be detected with coercivity forces $B_{1/2}$ lower 50 mT. However, in specimens P08_1 and P14_4, additionally a second component, which shows high coercivity forces, higher than 1000 mT, is present. The backfield remanence was only enhanced in specimen P14_4. The results are presented in Table 8.

a)

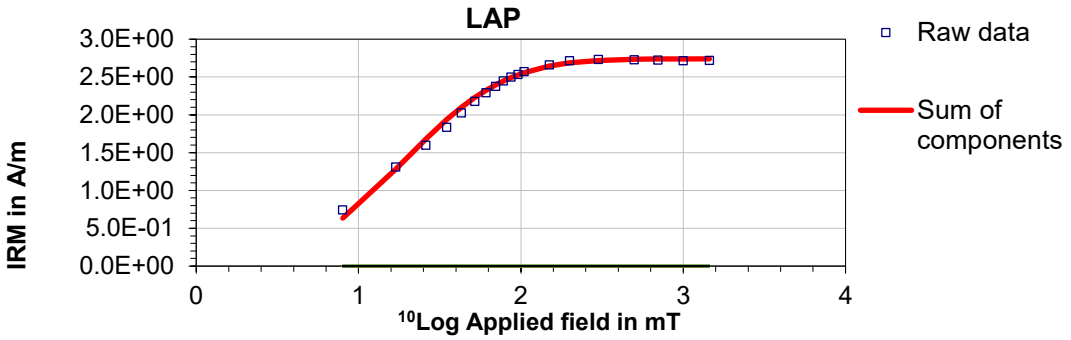

b)

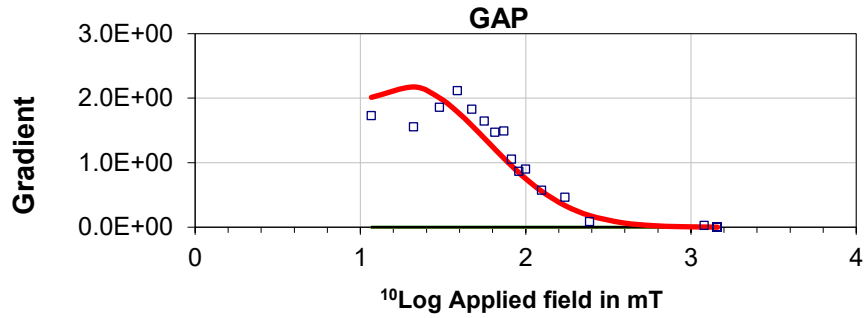

c)

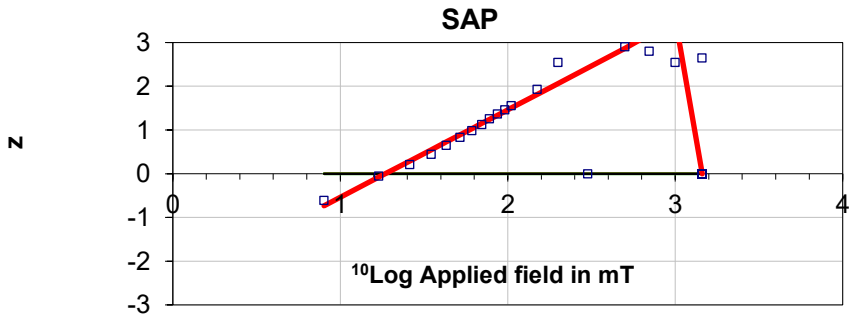

Figure 49: Results of the IRM analysis of Specimen P01_5. (a) Linear Acquisition plot (b) Gradient acquisition plot (c) standardized acquisition plot. The three different fitting curves are generated by an excel sheet published by Kruiver et al. (2001).

Table 8: Results of the laboratory measurements. SIRM: saturation IRM, B1/2: coercivity force, Hcr: backfield coercivity force, NM: not measured NO: no orientation found.

Sample point		**SP_01**	**SP_02**	**SP_03**			**SP_04**	**SP_05**			
Specimen ID		P08_1	P05_3	P06_4	P11_6	P14_4	P10_3	P01_5	P02_2	P03_2	P04_2
Bulk susceptibility [SI]		0.0001	0.0060	0.0168	0.0332	0.0002	0.0039	0.1416	0.1123	0.0860	0.0924
Curie Point [°C]	Heating curve	354	330	550	330	580	590	607	607	630	612
	Cooling curve	520	580	564	335	600	607	623	622	642	622
NRM	Magnitude [A/m]	-	0.317	0.659		0.00104	0.1887	0.74	0.4163	0.872	2.665
	Orientation Dec/Inc [°]	137/-7	NO	NM			NM	312.7/37.2			
	Alpha 95 [°]	5.9						8.9			
IRM	SIRM 1 [A/m]	0.061	3.15			0.034	1.43	2.74		1.54	
	B ½ 1 [mT]	23.4	6			44.7	17.8	18.6		25.1	
	SIRM 2 [A/m]	0.0145				0.01					
	B ½ 2 [mT]	1778.3				1000					
	Contribution [%]	81/19				77/23					
	Mmax [A/m]	6.50E-02	3.1			4.10E-02	1.44	2.7		1.54	
	Hcr [A/m]	13	<8			40	13	9		13	

9 Discussion and Interpretation

9.1 Paleomagnetic measurements

For the identification of the magnetic minerals in the samples, typical values for the Curie point and Coercivity forces were taken from Tauxe (2005) and are summarized in Table 9.

Table 9:Typical values for the Curie point and Coercivity forces after Tauxe (2005).

Mineral	Curie point [°C]	Coercivity force [mT]
Pyrrhotite	270~325	Vary widely
Magnetite	580	< 50
Maghemite	590-675	between 50 and 500
Hematite	675	>500

Sampling point 1, 3 and 4

The three specimens P08_1, P14_4 and P10_3 of these sampling points show a very similar behavior during the heating and cooling process (Figure 50). The susceptibility is enhanced for point 4 but still all values are below 0.004 SI. During the heating, the mineral content changes and the curves are not reversible. The increase of susceptibility at around 280°C can be described through the transition from pyrite to pyrrhotite. Due to the further increase of the temperature, pyrrhotite transforms to magnetite at around 500 °C (Tauxe, 2005). After cooling down the specimens again to room temperature, they show a higher susceptibility than before, which is mostly due to the artificial generated magnetite. The Curie points for specimens P14_4 and P10_3 are at 580 °C, what represents the artificial produced magnetite and differences in the specimens can be related to the different amount of magnetite. According to the IRM analysis, specimens P08_1 and P14_4 contain also a second magnetic component, which is, due to the high coercivity values, hematite. In both, hematite contributes around 20 % to the magnetic saturation magnetization. A slightly enhanced back field coercivity, which indicates the presence of higher coercive minerals, was also found for specimen P14_4. Only at sampling point 1, an orientated sample could be taken, where the measured orientation of the natural remanence has a declination of 137 ° and an inclination of -7 °.

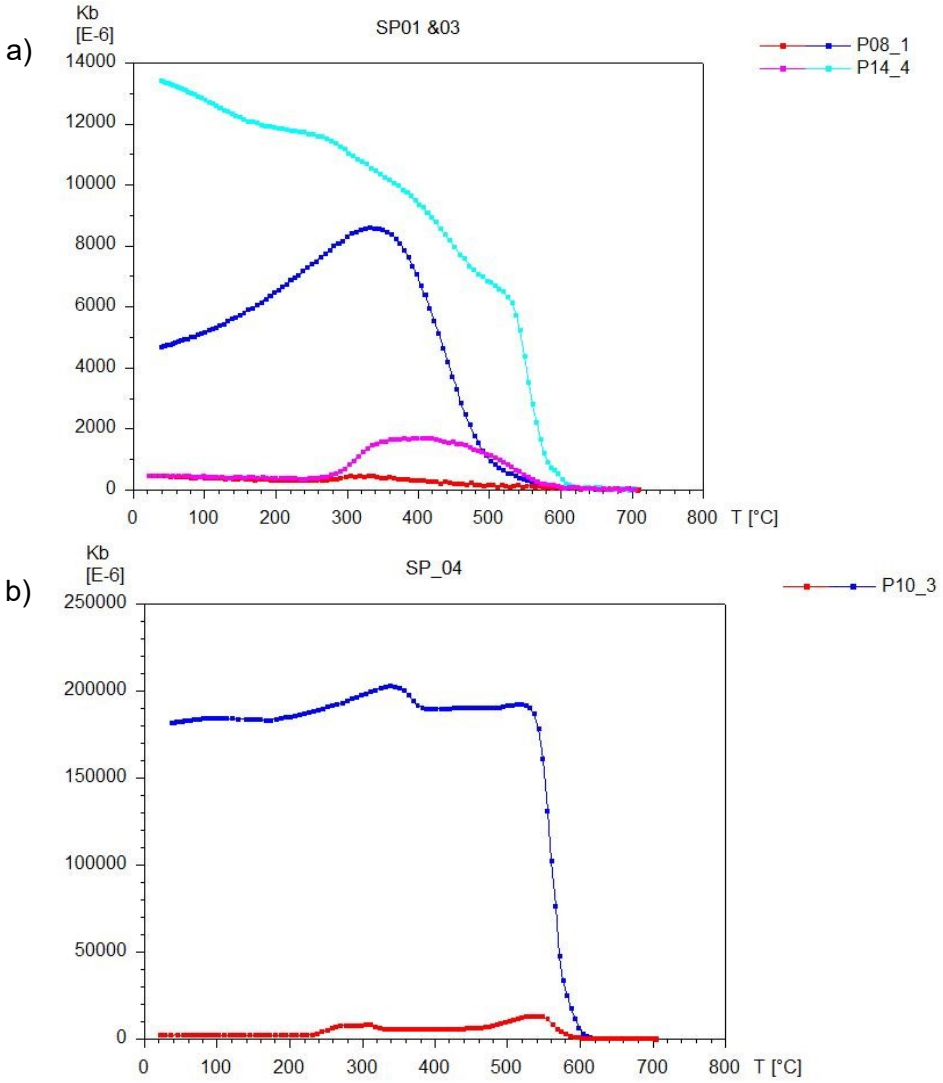

Figure 50: Result of the Curie temperature analysis for specimen (a) P08_1, P14_4 (b) P10_3.

Sampling point 2

Susceptibility values of this point show a high variability. This can be explained because some specimens contain visible mineralized zones and others mostly surrounding rock (mostly quartz) with low susceptibility values. Specimens P11_6 and P05_3 show similar behavior in the heating curve, but the susceptibility values of P11_6 are 10 times higher (Figure 51). This is associated with mineralizations in P11_6 and finely disseminated magnetic minerals in P05_3, what can also be seen in Figure 52, where the whole sample 5 is obviously much darker. From the heating curve both specimens show a Curie point of 330 °C, which is typical for pyrrhotite. During the heating, at around 500 °C, pyrrhotite breaks down again to magnetite. In addition, in specimen P11_6 hematite is also generated above 620 °C. The behavior of the cooling curve is also slightly different for the two specimens. While the cooling curve of P11_6 is reversible, except for the area where magnetite developed, the cooling curve of P05_3 is nonreversible and shows lower susceptibility values after the heating and cooling again. Even if also in sample 6 mineralizations are clearly visible, they could not be measured, because they break out during the cutting of the specimens.

Therefore, the surrounding quartz was mainly measured with only a low amount of magnetic minerals. The orientation of the remanence was measured, but the specimens show a high variability and no direction.

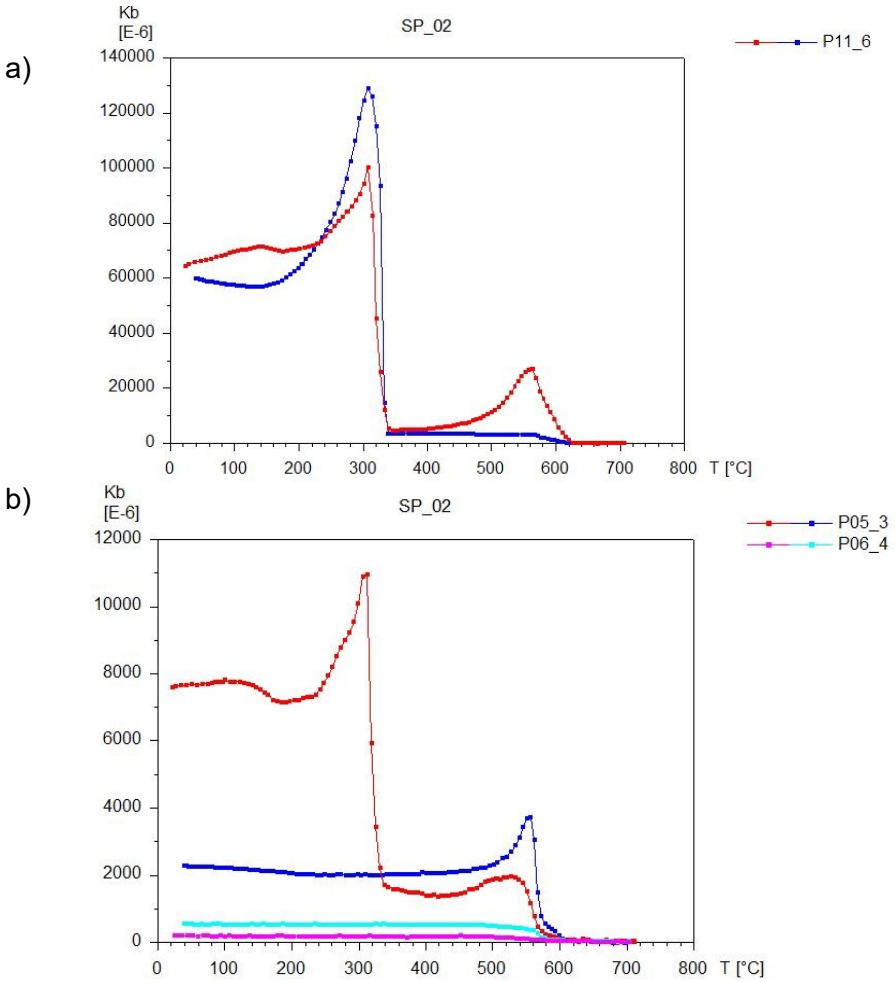

Figure 51: Result of the Curie temperature analysis for specimen (a) P11_6 (b) P05_3, P06_4.

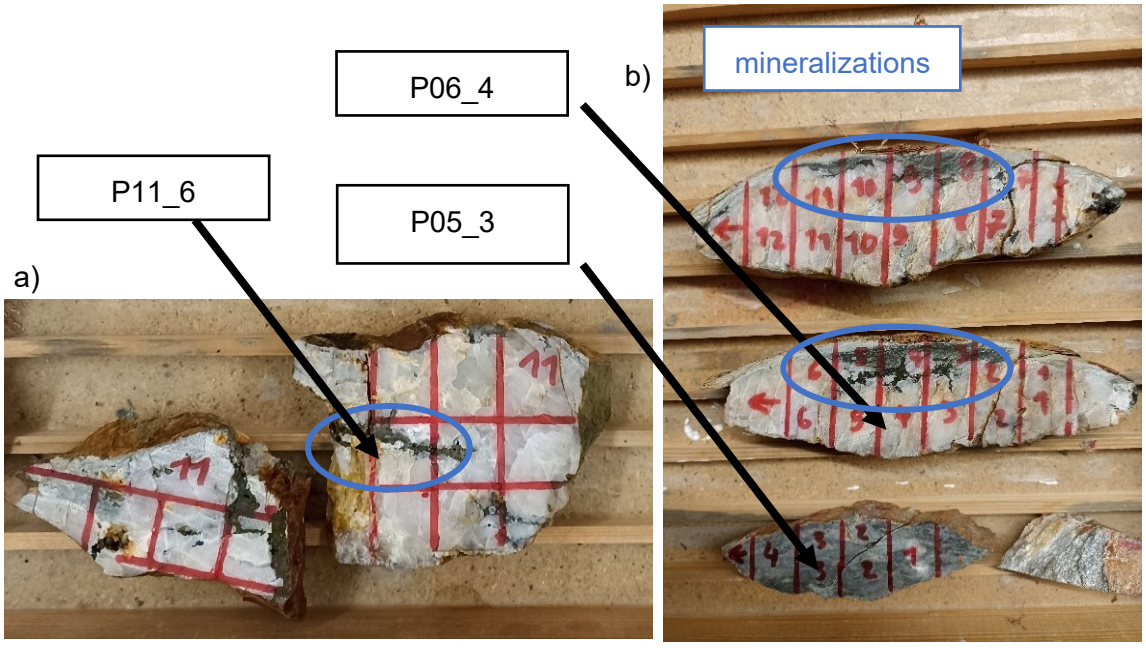

Figure 52: (a) Samples of sampling point 2 with mineralized zones (blue circles). (a) Sample 11, specimen 6 (b) Samples 5 and 6 with specimens 3 and 4.

Sampling point 5

The highest susceptibility values were found in specimens of this sampling point. The heating and cooling curves of the four measured specimens are reversible and only differ slightly in the susceptibility values and therefore in the concentration of magnetic minerals (Figure 53). A Curie point of 620 °C was found, which indicates maghemite. The orientation of the remanence has a declination of 312.7 ° and an inclination of 37.2°.

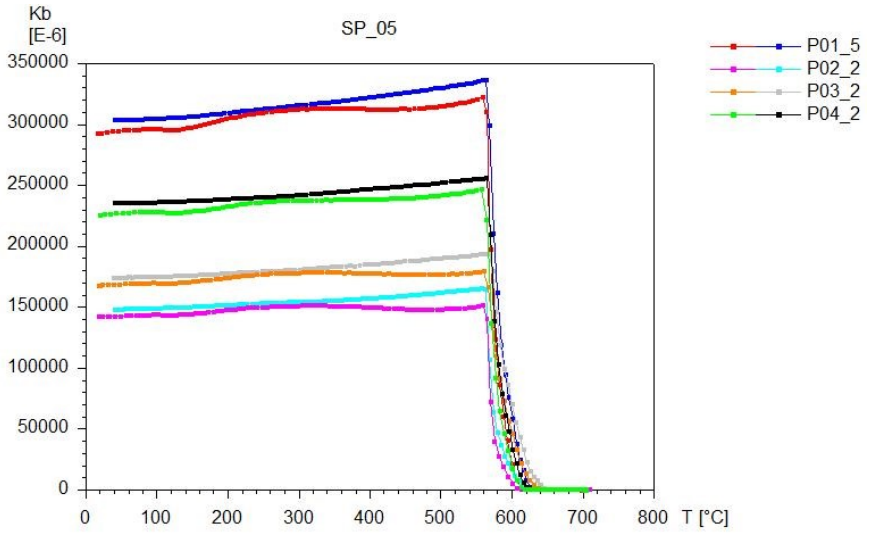

Figure 53: Result of the Curie temperature analysis for sampling point 5 with the specimens P01_5, P02_2, P03_2, P04_2.

9.2 Geomagnetic measurements

Around 70 % of the magnetic data show values between minus and plus 200 nT. Therefore, these values were excluded for anomaly detection because they can be seen as background. The remaining anomalies were combined to magnetic zones, according to their location, geometry and intensity (Figure 54). To achieve a better result, not only the absolute values were considered, but also the magnetic curves were analyzed. For the model, only anomalies which can be related to other ones on neighboring profiles were considered. Smaller anomalies or isolated ones were not modelled, because the focus is clear on the detection of mineralizations. The general strike of the geological formations was also considered for combining anomalies. In total, three magnetic zones and three deeper magnetic bodies could be identified. The susceptibility values mostly range between 0.007 and 0.025 SI and the amount of overburden is in general small. Detailed information about the modeled bodies can be found in Appendix C1. The individual profiles with the measured but also with the calculated data according to the model from POTENT can be found in Appendix C2.

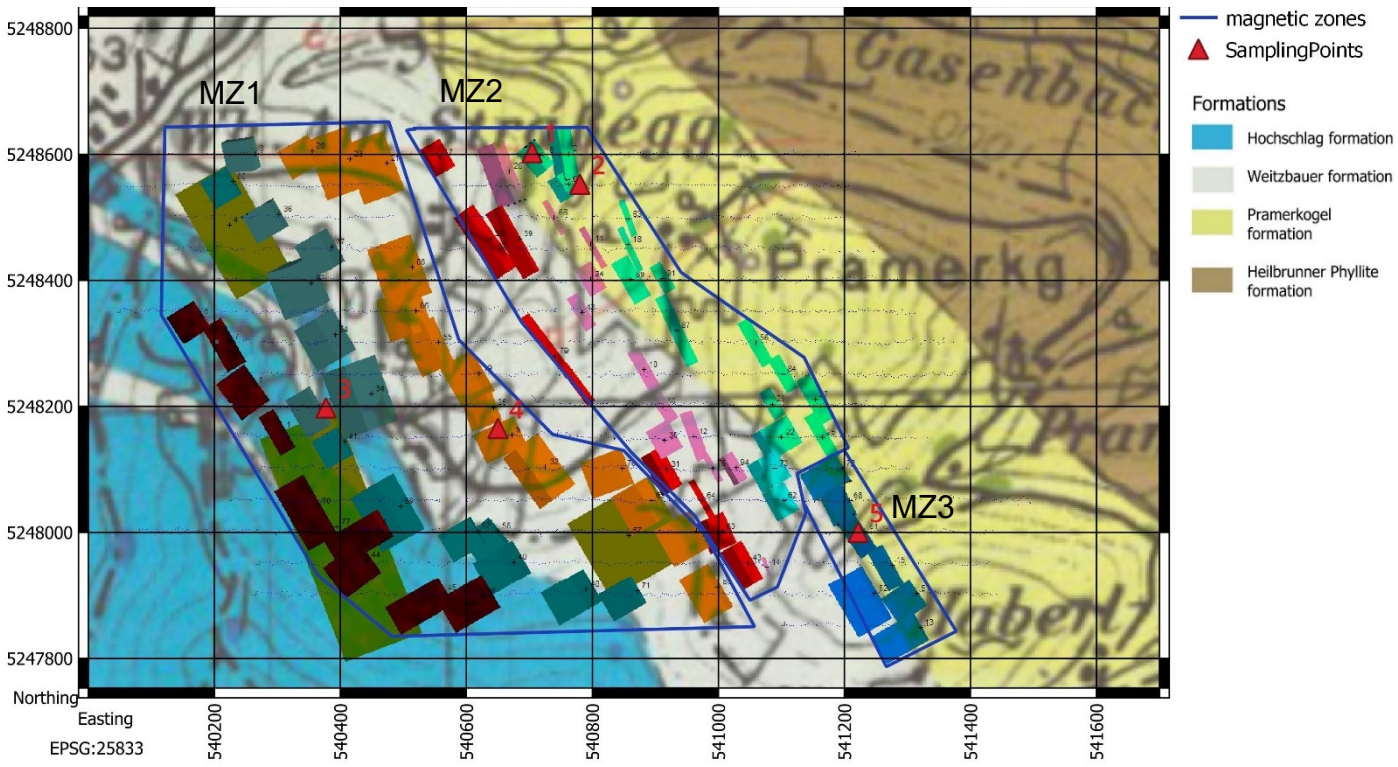

Figure 54: Magnetic anomaly zones based on the magnetic model constructed in POTENT. Magnetic anomalies which belong together are marked with the same color. dark red: MZ1-1, petrol: MZ1-2, orange: MZ1-2, red: MZ2-1, pink: MZ2-2, green: MZ2-3, blue: MZ3. The geological map was taken from Antes (1998).

Magnetic zone 1 (MZ1)

This zone is in the western part of the profiles in the Hochschlag and Weitzbauer formation, whereby three independent anomalies can be identified. For each anomaly, at least one magnetic body with a thickness of 20 to 60 m can be followed across the whole survey area, where the average dip is 30° towards south-west. The first anomaly MZ1-1 is characterized by thin bodies in the north, where towards south the bodies become thicker, with up to 60 m. In anomaly MZ1-2, rectangular magnetic bodies with a thickness of 50 m prevail. In the very north of anomaly MZ1-3, three bodies could be modelled with only a small spatial distance. Due to the farm buildings, the observations of the area were deleted and therefore no bodies could be modelled. South of the buildings only one magnetic body is remaining. This body continues towards south-east with minor differences in dip and size. Within this zone, three deep larger magnetic bodies (DMB-1, DMB2, DMB-3) could be identified in a depth of around 120 to 200 m below surface. To verify, if the individual magnetic bodies are connected, a 3D topography model was created and one single plate inserted. For all anomalies, a correlation between the individual bodies and the plate can be seen, where the individual bodies occur roughly at the position at which the plate intersects the surface (Figure 55). It must be pointed out that one single plate is an idealization and therefore small deviations between the plate and the individual bodies are expected. However, anomaly MZ1-1 can be described by a plate with a strike and dip of 145°/30°, MZ1-2 shows a strike and dip of 147°/20° and MZ1-3 140°/30°. After Antes (1998), the average dip of the formations is between 30° and 50°. Therefore, it can be concluded that the magnetic bodies from anomaly zone 1 are stratiform in the Hochschlag and Weitzbauer formation.

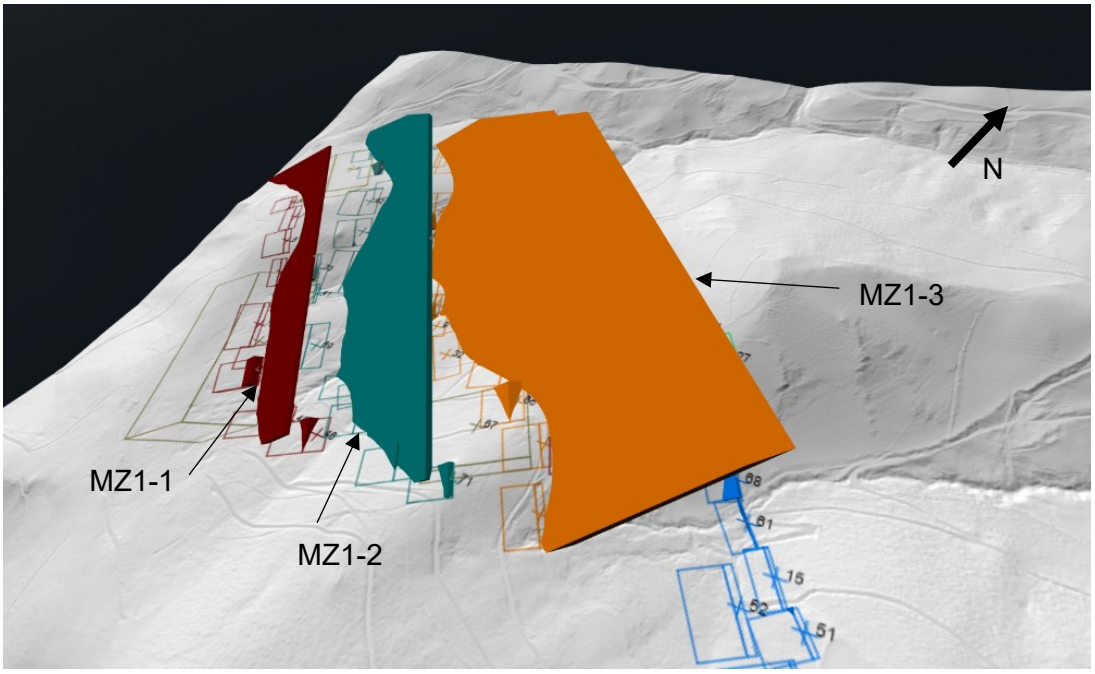

Figure 55: 3D topography model with the individual bodies as cross sections and idealized plates, which represent the three anomalies of the magnetic zone 1. The dip of the plates lies between 20° and 30° towards south-west. Background: digital elevation model (GIS Steiermark, 2023).

Deep magnetic bodies (DMB)

In the magnetic data towards the western end of the survey area, three deeper and larger magnetic bodies can be modeled. This is also supported according to aeromagnetic data gathered by the Geological Survey of Austria in 1992 (Seiberl, 1993). A big positive anomaly with up to 160 nT was observed in the survey area, which belongs to the Straßegg anomaly (Figure 56). However, Antes (1998) interpreted the source of the Straßegg anomaly as magnetite bearing lenses in the greenschists of the Pramerkogel formation in a depth of about 500 m. In the survey area itself no depth points were calculated and the calculation of these bodies was done without a topography correction. By using a susceptibility of 0.05 SI for magnetic bodies, what was suggested by Stadelhofen (1994) for magnetite, the center of the rectangular bodies are located in about 200 m below surface. The bodies are characterized by a strike of 155° and a plunge of 10° towards north-west. This geometry is also in agreement with Antes (1998), where the deeper anomalous bodies occur more in the north-west. The highest values from the aeromagnetic data in the survey area are located exactly above the center of DMB-2. Here the uppermost corner is in a depth of about 130 m below the surface. For bodies DMB-1 and DMB-3, a clear correlation to the aeromagnetic data cannot be seen, what could be related to the smaller geometry of the bodies. However, the aeromagnetic data is still showing enhanced reduced magnetic intensities in those areas. Differences according to the depth of the magnetic body can be related to the topography and the different resolutions.

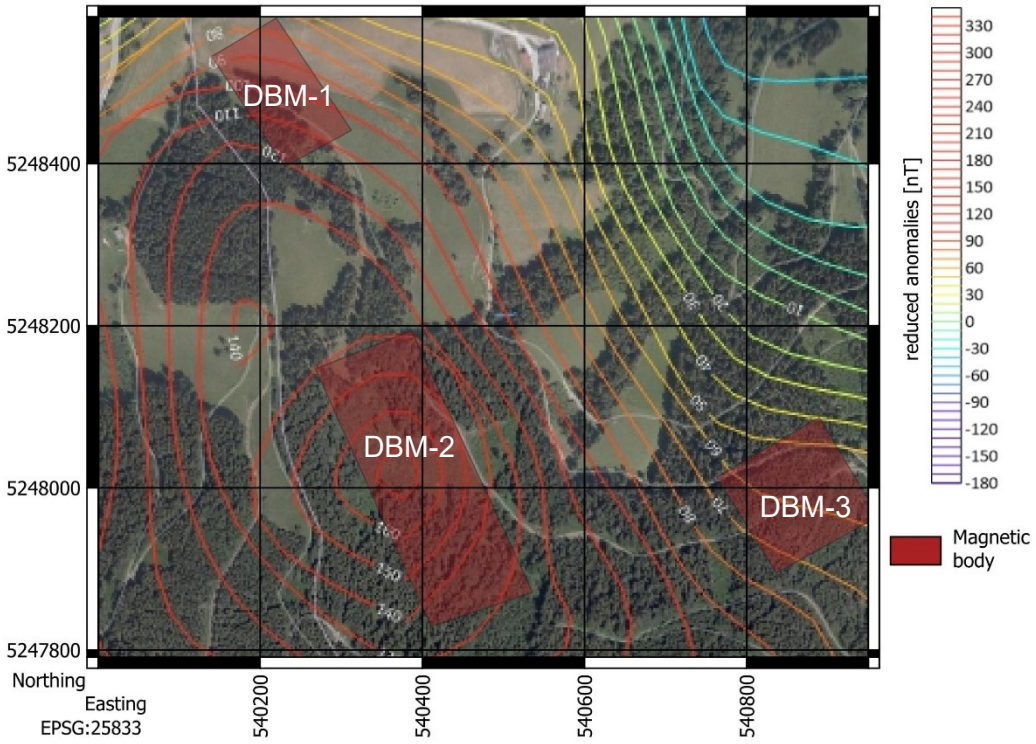

Figure 56: Deeper magnetic bodies (red) and isolines from the aeromagnetic survey done by the Geological Survey of Austria in 1992. Background: Orthophoto (GIS Steiermark, 2023).

Magnetic zone 2 (MZ2)

In this zone not only the farm buildings were affecting the measurements but also a lack of data due to the crossing of the trenches. Therefore, a consistent magnetic body could not be modelled in this area. However, in difference to the above-mentioned zone 1, the bodies of this zone are thinner, show a different orientation and are steeply inclined. At least three magnetic structures occur in this zone, where two possibly merge in the south to one single one. A fourth anomaly can be seen in the east of this zone, which shows only a small spatial expansion. The intersection of a plate with the surface, which is dipping 30° towards south-west (Figure 57a) confirms that the magnetic bodies must be steeper. A 30° dip would result in an arc towards north-east, which cannot be observed in the data. By introducing three plates with a dip of 70° (Figure 57b), the individual bodies can be described better. The steep alignment can also be confirmed by the observed dip in sampling point 2 of 70 °. Since these bodies are much steeper than the formations and pass through formation boundaries, a vein character can be assumed.

a)

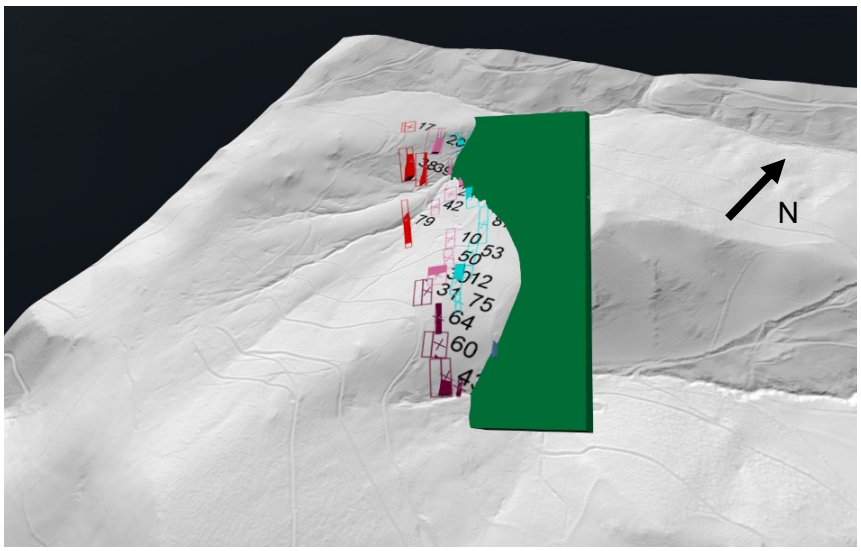

b)

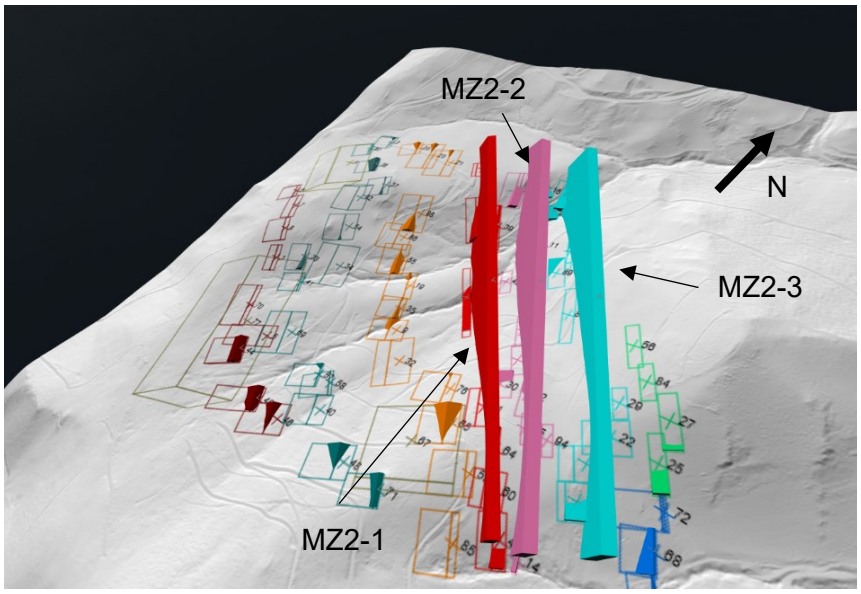

Figure 57: 3D topography model with the individual bodies as cross sections and idealized plates, which represent the anomalies of the magnetic zone 2. (a) plate with a dip of 30° (b) dip of the plates between 60° and 70°. Background: digital elevation model (GIS Steiermark, 2023).

Magnetic zone 3 (MZ3)

This zone is characterized by only one magnetic anomaly, which is restricted to a small area south of the Pramerkogel. The modelled bodies are thin with about 7 m, but due to the high susceptibilities of 0.1 SI, the magnetic response is strong. This is also because the bodies are very close to the surface. For sampling point 5, which is in the middle of zone 3, an azimuth of 257° with a dip of 21° could be determined, which is also confirmed by the magnetic data. At least three 0.7 m to 1 m thick layers could be identified in the field with a nonmagnetic gab of around 1 m. Due to the model block size of 7 m, most likely some more magnetic layers are present.

9.3 SP measurements

In general, the location of the lowest potential of an anomaly also indicates the shallowest position of the oxidization zone. Therefore, these positions were used for connecting anomalies across the survey area, whereby only anomalies which can be followed over multiple profiles were considered. As already seen in the magnetic measurements, the SP anomalies are also following the geological strike. Altogether 13 anomalies could be identified, where most of them are crossing the whole survey area. Even if the curves were used for the identification of the anomalies, for better visualization only the relative values of the SP data are shown in Figure 58, whereby values above -50 mV are blanked out. This is because these values can be seen mostly as background values and do not indicate any anomaly.

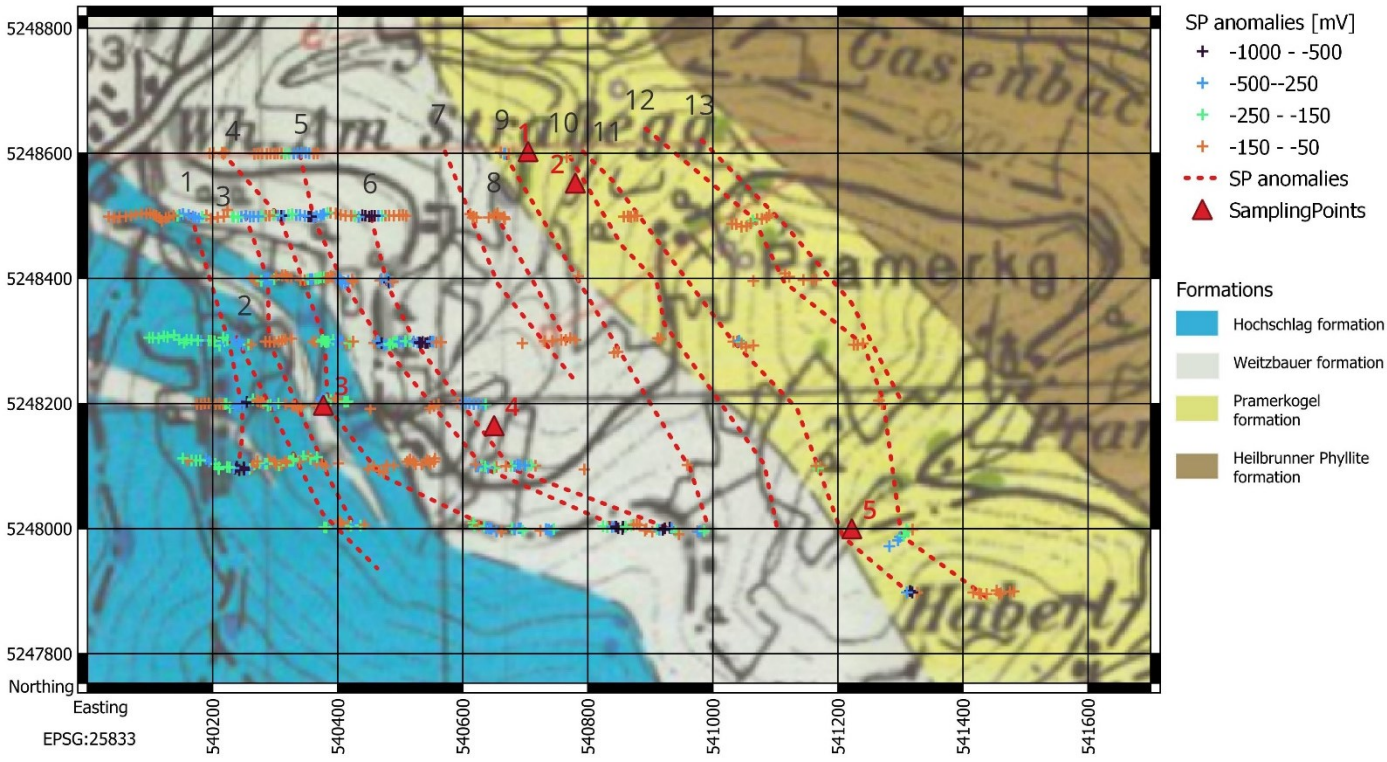

Figure 58: Connected Self-potential anomalies in the survey area. The geological map was taken from Antes (1998).

Anomalies 1 to 6 are in the foot wall of the Hochschlag formation and the hanging wall of the Weitzbauer formation. They are very similar in the orientation parallel to the formation boundary, where small differences in the orientation can be explained by the topography effect. This can be seen especially at anomalies 3 and 4, which cross a trench with a high elevation difference. Anomalies 5 and 6 show the greatest potential drop, which can be partly related to the flow potential of the water. Numerous drainage pipes could be observed during the field measurements in the north-west of the study area, indicating that a large amount of water from the carbonates is flowing down the slope and leaving the ground at the boundary to the underlaying Weitzbauer formation. Nevertheless, due to the strength and the large extension of the anomalies, this cannot be the only reason for their occurrence. However, in the northern profiles the anomalies are clearly separated from each other by 50 to 100 m and show an expansion of around 50 m. Further south, an additional anomaly appears and the spatial distance between the anomalies becomes smaller. As a result, the anomaly curves partly overlap each other and it is more difficult to clearly distinguish between them. Anomalies 7 to 13 are characterized mostly by a small drop in the potential, with values up to -150 mV. Only in the southernmost profile, potentials lower than -500 mV can be observed. Also, the orientation is slightly different, where the anomalies do not follow the geological formations and cross formation boundaries. Anomalies 7 and 8 are visible in the area of the trench where they are closer to the surface and due to the greater amount of overburden towards south, they cannot be followed further. Therefore, only a small oxidization potential can be related to them. Anomalies 9 and 10 show stronger self-potential values, especially in the very north and south. In between, some minor changes in the potential can be seen. The northern part of the anomalies is in the Pramerkogel formation. Towards south, they are crossing the formation boundary to the Weitzbauer formation. Some greater changes in the potential across the whole survey area can be observed for anomaly 11 where in the north it could possibly merge with anomaly 10. Anomaly 12 can be described as a broad one with only low SP values, what would indicate a deeper oxidization zone. At two points, the anomaly is close to the surface (Figure 59), what can be seen due to a narrow and strong potential drop. At the northern point also a second narrowly defined anomaly can be observed, which can be followed further north. The geoelectrical profile conducted during the geophysical field workshop in April 2022 (GGFW) crosses the SP anomalies 10, 11 and 12 in the north and confirms the location of these anomalies. In addition, it was also stated out, that anomalies 10 and 11 are very close to each other and overlapping in the SP response, what would support the idea that these anomalies merge in the northern part. In the south, geoelectric profile 1 and the profile conducted during the geophysical field workshop in October 2022 (GGÜ) crossing SP anomaly 11 and 12, where the two SP anomalies can also be observed. Based on that data of the GGÜ, the bend towards south-east was drawn. The last discussed anomalies are in the Pramerkogel formation and by comparing the location of sulfidic mineralizations found by MINREX (1987) and the SP anomalies (Figure 59), a possible correlation can be seen, if one also considers the age of the map and the GPS deviations.

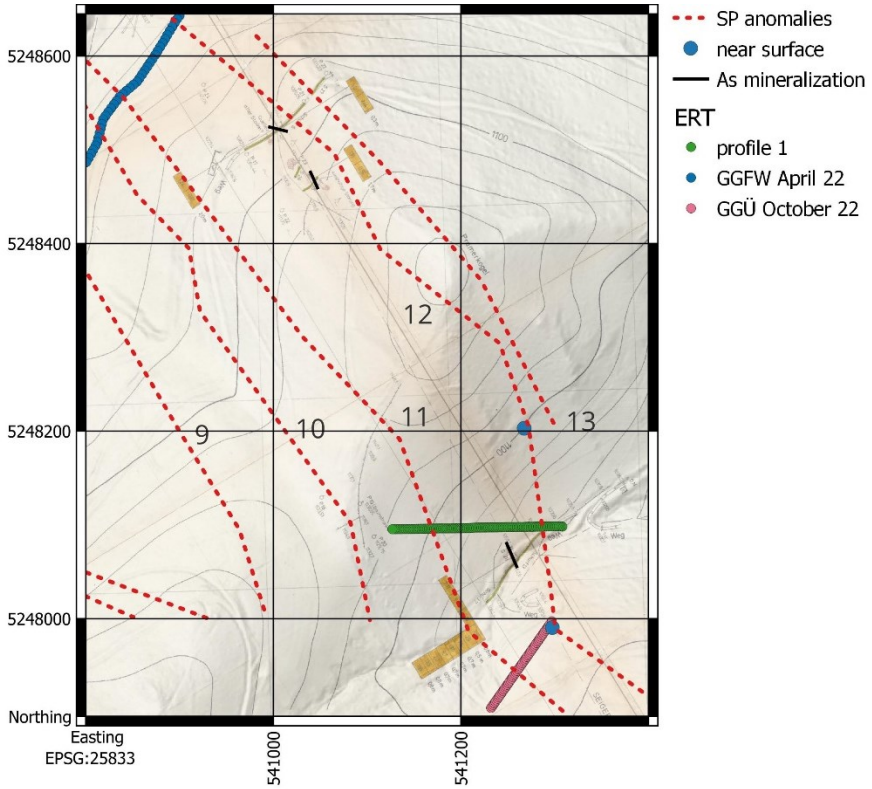

Figure 59: Comparison of the SP anomalies with the sulfidic mineralizations found by MINREX in 1987 and the location of the ERT profiles.

9.4 Data comparison

9.4.1 Magnetic and SP

By overlaying SP anomalies with the reduced magnetic intensities, some correlations can be found (Figure 60). In general, a clear distinction between magnetic and SP anomalies is difficult due to the high magnetic activity in the Weitzbauer formation and the variations in the GPS accuracy. However, while anomalies 2 and 4 can be clearly seen as magnetic, anomalies 1, 3 and 5 show a non-magnetic behavior. Even if these anomalies occasionally cross magnetic anomalies, most parts are of non-magnetic nature. The same is true for SP anomaly 6. It must be pointed out that magnetic and non-magnetic anomalies are alternating in this area. After a non-magnetic SP anomaly, a magnetic one and again a non-magnetic one appears. As they also follow the magnetic anomalies from zone 1, for which a stratiform behavior could be defined, the SP anomalies can also be described as stratiform. SP anomalies 7 and 8 are again close to magnetic anomalies. Due to the lack in magnetic data because of the trench and the farm buildings, the magnetic behavior of SP anomalies 7 and 8 can neither be fully confirmed nor excluded. Concerning the magnetic model, these anomalies are at the same location as the modelled plate MZ2-1. As a result, magnetic behavior will be assumed.

A clearer correlation between SP and magnetic data can be seen in SP anomalies 9 and 10, which correlate with magnetic anomalies MZ2-2 and MZ2-3, where only in the middle part of anomaly 10 a lack of magnetic activity is present. This could be due to the higher overburden in that area. Due to the overlap with the magnetic anomalies from zone 2, the vein character is assumed. In the magnetic data gathered by the two groups from the geophysical field workshop in April 2022, a series of magnetic anomalies can be seen, where the location fits with the location of SP anomaly 10. This also supports the magnetic behavior of SP anomaly 10. SP anomaly 11 to 13 can be again seen as non-magnetic. Only in the southern area, they are near a magnetic anomaly zone.

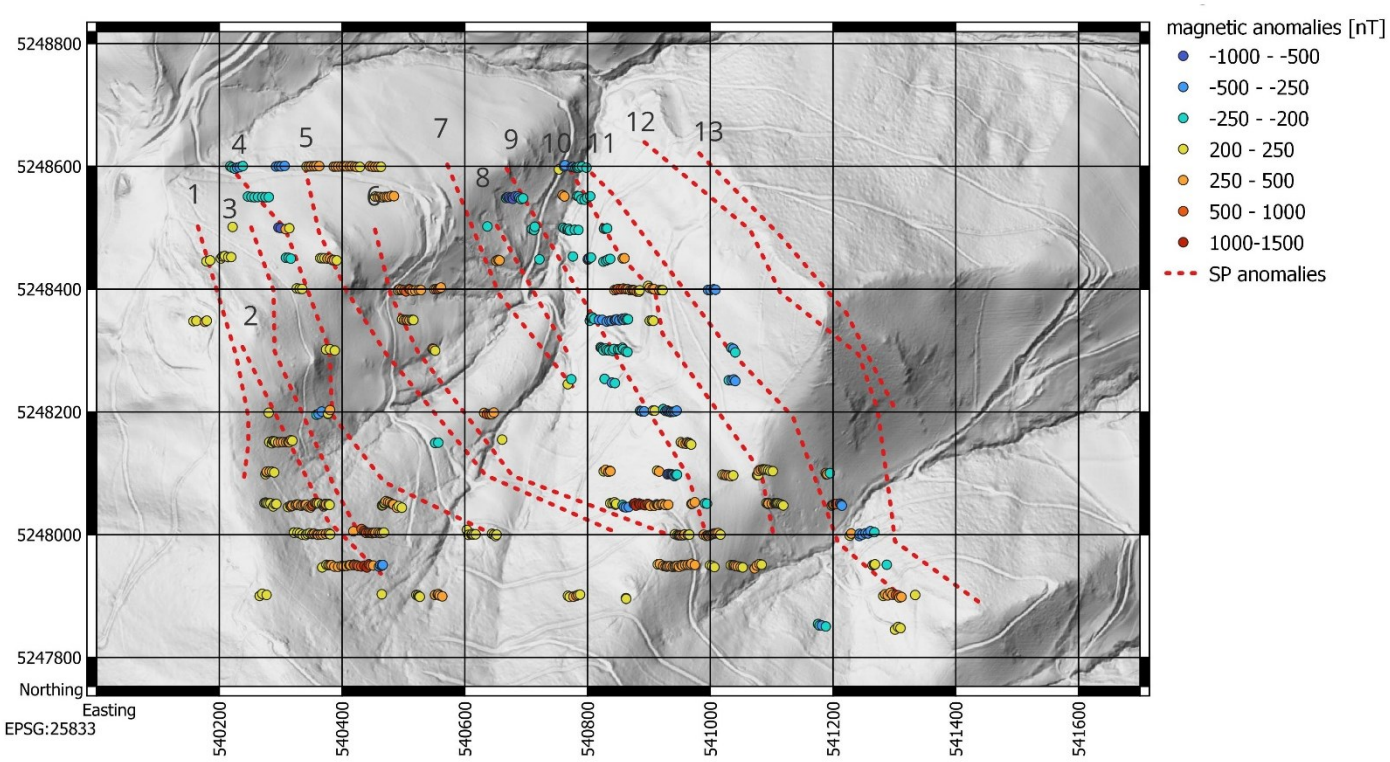

Figure 60: Comparison of the SP and magnetic anomalies. Background: elevation relief (basemap.at, 2023).

9.4.2 IP, ERT, Magnetic and SP

Profile 1

Figure 61 illustrates the overlap of geoelectric profile 1, which is in the Pramerkogel formation, with the corresponding magnetic and SP data. The first IP anomaly zone at 64 m profile distance cannot be detected by using magnetic data, but in the SP data a light depression can be seen between profile distance 0 and 77 m, which belongs to SP anomaly 12. From the IP data as well as from the SP data, a larger overburden of the anomalous zone can be expected. As already discussed, measurements with 1 Hz instead of 4 Hz show higher phase angles. If one considers that the profile was measured with 4 Hz and additionally the measured depth and strength of the IP anomaly, a much higher polarization effect can be assumed for this area. Another influence of the large overburden is that the location of the anomaly was varying depending on the inversion parameters. Therefore, a possible relation between SP and IP is likely. The second steeply inclined zone of high IP values shows a very little overburden and can be followed till a depth of about 35 m. This anomaly correlates very well with the SP anomaly 11. A drop in the potential of about -250 mV can be observed above the highest phase angles, which is also the shallowest position of the anomalous body. Due to the little overburden, the phase angles are higher than in the before mentioned anomaly and the already suggested non-magnetic behavior of this anomaly can also be confirmed. Both IP anomalies appear in areas where the resistivity is low. Especially for the latter mentioned IP anomaly, the resistivity values in the upper part are lower 10 Ωm. At profile distance 125 m, a significant magnetic anomaly was measured which belongs to the magnetic anomaly zone 3. Neither in the resistivity nor in the IP an anomaly can be related to the magnetic one. To verify if the magnetic anomaly is already in the low resistivities or still in the higher resistivities, the shorter profile w2_1ss was used. Here, the location of the magnetic anomalies is clear in the higher resistivities and no IP effect can be related to this anomaly. The overall lower resistivities in the western part of the profile compared to the eastern part would indicate a lithological change from the Pramerkogel to the Weitzbauer formation. Since this area is also the location of the low resistivity anomaly, a clear border between the formations cannot be defined.

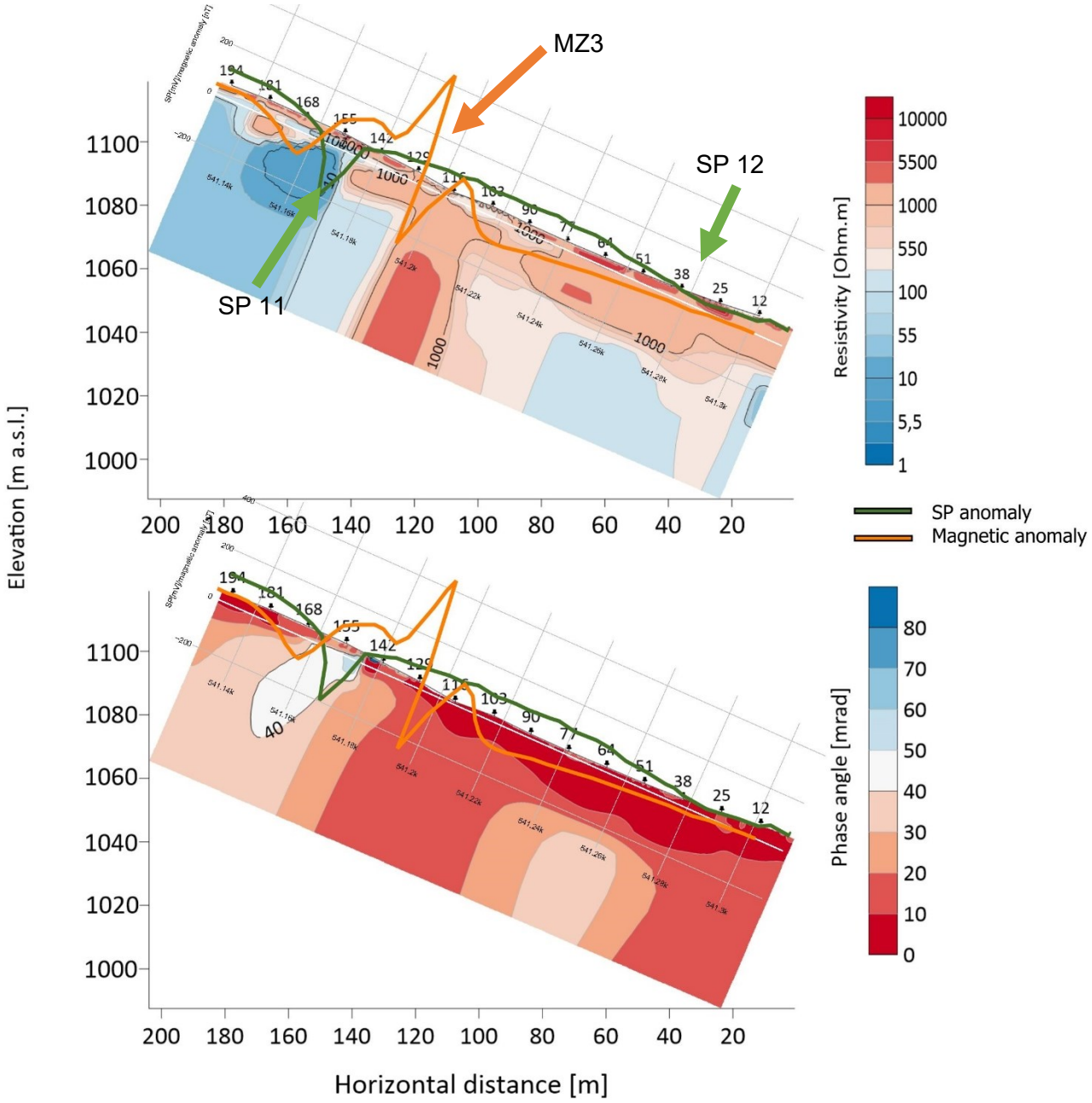

Figure 61:Comparison of geoelectric profile 1 with the magnetic and SP measurements.

Profile 2

The second IP profile is located in the hanging wall of the Weitzbauer formation close to the carbonatic Hochschlag formation, where several SP anomalies and one magnetic anomaly can be seen (Figure 62). At the beginning of the profile in the east, the magnetic data shows a significant drop, which can be mostly related to the farm buildings and not to a natural structure. Still, anomaly MZ1-3 is crossing the geoelectric profile in this area. The eastern part of the first IP anomaly, which shows resistivity values of around 100 Ωm could be related to this magnetic anomaly. The western center of the IP anomaly can be related to SP anomaly 6, which shows a potential drop of about -900 mV at the location where the resistivities are below 10 Ωm. In difference to the IP anomaly, the resistivities lower 10 Ωm continue in depth and show a dip towards west. SP anomaly 5 between 135 and 193 m profile distance is in agreement with high IP values and low resistivities, but again a continuation of the resistivities towards greater depths can be seen. These differences between IP and resistivity can be possibly related to the model resolution, which decreases towards greater depths and to the sides of the inversion model. In addition, the water can also contribute to the differences, especially for the first mentioned zone. The farm buildings next to the beginning of the profile can act as a dam for the water which is coming from the carbonates in the west. The small IP anomaly at 115 m profile distance can be related neither to the SP nor to the resistivity values. In difference to the before mentioned SP anomalies, SP anomaly 4 shows a non-symmetric behavior, which indicates a structure dipping towards west. Between 200 m and 230 m profile distance, the second magnetic anomaly MZ1-2 appears. A differentiation, if the SP and magnetic anomaly belong to the same structure cannot be done according to this profile, but due to the already mentioned magnetic and SP comparison, SP anomaly 4 can be seen as magnetic. Therefore, it will be assumed that the eastern center of the IP anomaly at 213 m profile distance is related to the magnetic SP anomaly 4. The western part of the IP anomaly at 240 m profile distance will be assigned to SP anomaly 3. In this profile, it can be furthermore seen, that the SP values are related to the size of the oxidization zone. The greatest potential drop in the east belongs to the greatest IP anomaly and the lowest one is related to the smallest one in the west. High resistivity anomalies between 76 and 140 m and between 190 and 213 m profile distance do not show any IP, SP or magnetic effect. This could be related to intercalated carbonates in the black shales.

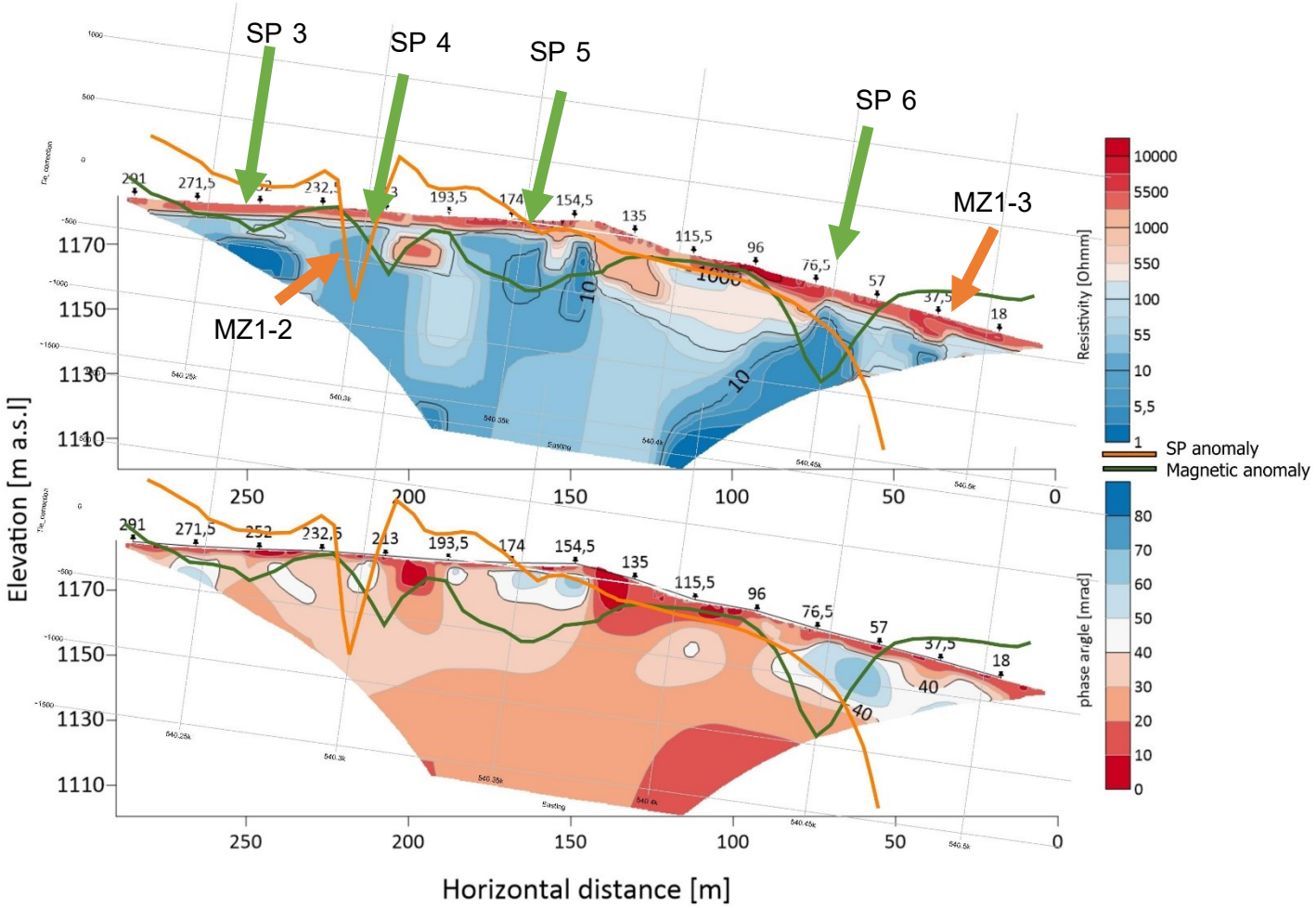

Figure 62: Comparison of geoelectric profile 2 with the magnetic and SP measurements.

9.5 Formation boundaries

For the survey area different geological maps are available, where the GIS Steiermark map (Figure 63a) stays in contrast to the map of Antes (1998) which is based on the work of Weber (1990) (Figure 63b). Both show the same formations, but the boundaries are different. Especially the Pramerkogel and Weitzbauer formation boundary (PWFB) differ a lot. This is also because of the fault in the north-east of the survey area, which is not visible on the map of Antes (1998). It must be mentioned that the differences are also a problem of resolution. While the GIS map is more focused on the big overview, the map of Antes (1998) is more locally. To prove which map is more precise the gathered geophysical data and field observations can be used. In the magnetic data a relatively clear boundary between magnetic activity and non-magnetic activity can be seen, which is close to PWFB in the GIS map. This would suggest that the Pramerkogel formation does not contain any magnetic minerals, which contrasts with the literature. Bojar et al. (2001) found pyrrhotite in the hanging wall of the Pramerkogel formation and after Antes (1998) the metavolcanites of the Pramerkogel formation also bear magnetite. Therefore, at least in the hanging wall of the Pramerkogel formation, magnetic anomalies can be present. Altogether, three ERT profiles across the PWFB suggested by GIS Steiermark are available. In all three profiles, resistivities are in general high with values above 700 Ωm, where towards the eastern ends, a trend to lower resistivities (< 500 Ωm) can be observed. For comparison, in profile 2, which is in the Weitzbauer formation, resistivity values are mostly below 100 Ωm. From electromagnetic resistivity data, Antes (1998) concluded that the Weitzbauer formation shows resistivities lower 150 Ωm at lower frequencies and lower 500 Ωm at high frequencies. The differences occur due to the different penetration depth, which is higher for lower frequencies. Not only the geophysical data, but also field observations from the different field workshops concluded, that a lithological change along the profile was not visible, but indications for a change are present close to the eastern end of the profiles. Due to the above-mentioned reasons, the lithological border between Pramerkogel and Weitzbauer formation interpreted by Antes (1998) seems to be realistic. As a result, the fault in the north of the survey area is questionable. The lithological boundary between Hochschlag and Weitzbauer formation is also differing slightly. While the ERT profile 2 is clearly in the Weitzbauer formation after Antes (1998), the western end is also in the Hochschlag formation after the GIS map. Most of the profile shows resistivities lower 100 Ωm what can be related to the black shales, whereas two high resistivity zones can be seen, which could be related to the carbonates of the Hochschlag formation. After Bojar et al. (2001) around 10 percent of the Hochschlag formation consists of intercalations of Black shale composed of quartz-chlorite-illite, muscovite-carbonate-organics and graphite with a thickness up to tens of meters. Therefore, a clear boundary between the formations cannot be given due to the variations between carbonates and black shales. However, since carbonates do not show any oxidization potential, it will be assumed that the SP anomalies in the Hochschlag formation also indicate the position of the black shale intercalations.

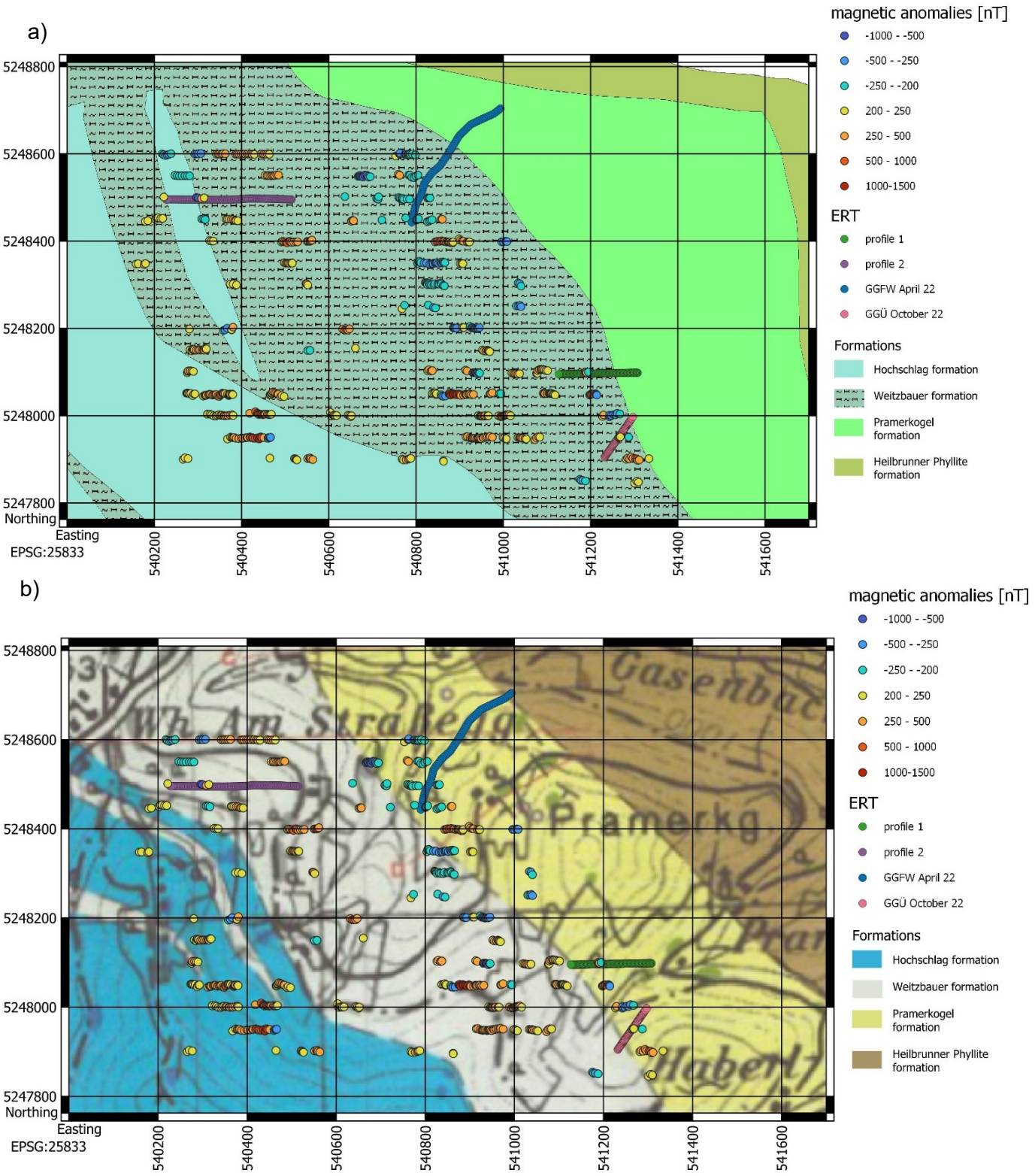

Figure 63: Geological Map of (a) GIS Steiermark, 2023 (b) Antes,1998.

9.6 Joint interpretation

According to the geophysical characteristics, geometry and location in the survey area five groups of anomalies can be defined (Table 10 & Figure 64).

Table 10: Groups according to the geophysical behavior.

Group	Magnetic anomaly	Self-potential [mV]	Phase angle [mrad]	Resistivity [Ωm]	Geometry	Formation
A	no	-300 - -1000	40 - 70	1 - 50	flat	Hochschlag Weitzbauer
B	yes	-100 - -500	30 - 45	50 - 100	flat	Hochschlag Weitzbauer
C	yes	< -200	20 - 40	100 - 400	steep	Weitzbauer Pramerkogel
D	no	-50 - -500	35 - 60	10 - 250	steep	Pramerkogel
E	yes	--	< 15	> 1000	flat	Pramerkogel

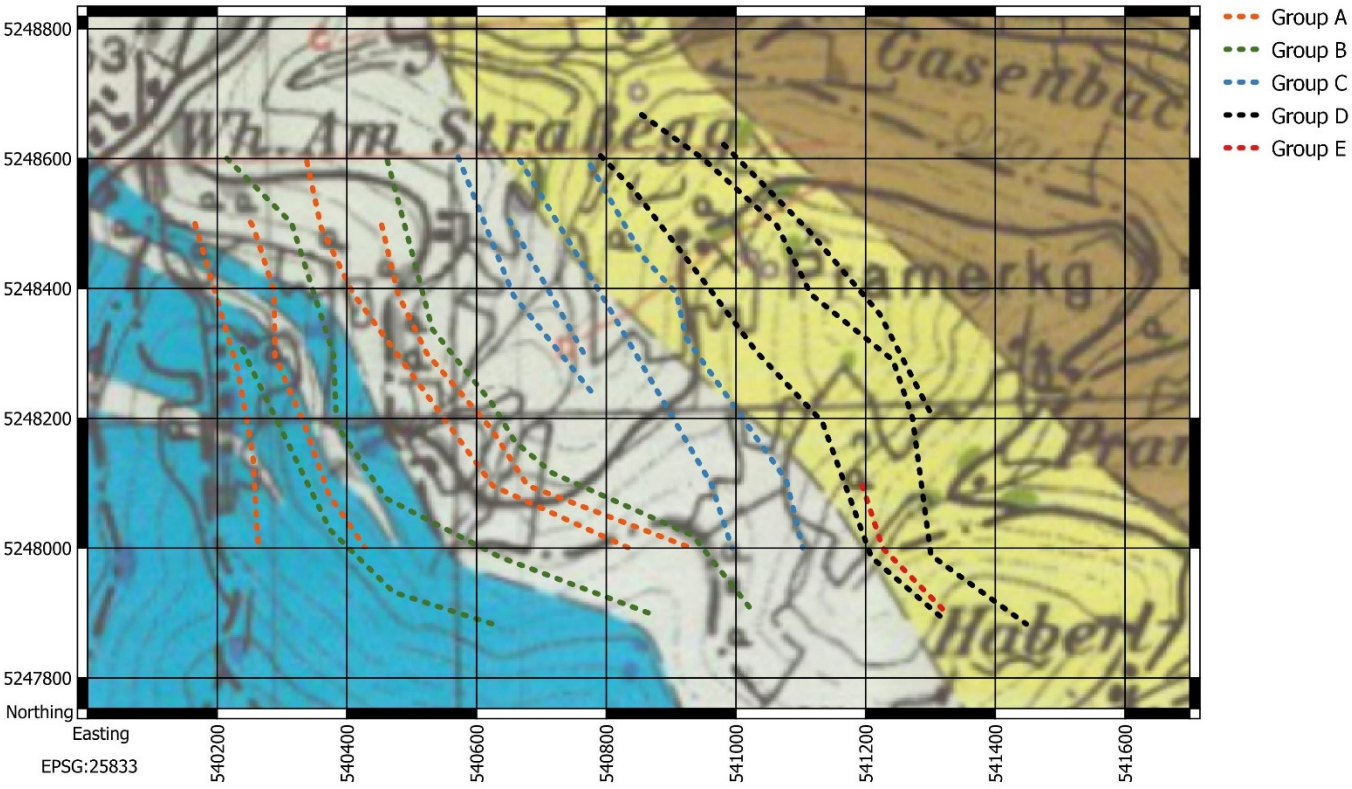

Figure 64: Group classification according to geophysical characteristics and location in the survey area. The geological map was taken from Antes (1998).

Group A

SP anomalies 1, 3, 5 and 6 belong to this group, which is characterized by great SP anomalies, high IP values, very low resistivities and no magnetic signature. The strength of the SP anomalies must be pointed out in this group, since here the highest potential drops could be measured. A similar behavior was already observed by Meschik (2016). During a bachelor thesis in Arzberg, which is a locality close to Straßegg and shows a similar geology, a general rise in the potential towards the carbonatic sequence could be found. Even if the maximum potential drop was not reached, values up to -700 mV were measured. Graphite and sulfidic mineralizations were suggested as possible sources of anomalies. However, after Bojar et al. (2001) graphite and pyrrhotite can be also found in Straßegg close to the Hochschlag formation. Due to the non-magnetic behavior of the anomalies and the very low resistivities, pyrrhotite can be excluded as source of the anomalies. By comparing the literature values presented by Weber et al. (1984) and Stoll & Gurk (2014) for a graphitic body (< 10 Ωm, up to -1000 mV) and the measured values, a clear correlation can be seen. In addition, after Jalete (1997), graphitic bodies show a significant IP effect. Therefore, for this group shallow stratiform graphite lenses with an expansion of 50 m are interpreted as the main source of the anomalies.

Group B

Magnetic anomalies from zone 1 belong to this group. As discussed, the three anomalies can be described through a 30 - 50 m thick 20° to 30° dipping plate, which follows the formation boundary and corresponds to the general dip of the area. Therefore, a stratiform character is assumed. Two samples were taken, where only low susceptibility values could be determined. Pyrrhotite with a small amount of hematite was found to be the reason for the magnetic behavior at the sampling points. For the first two magnetic anomalies MZ1-1 and MZ1-2, a clear correlation with the self-potential data can be seen, whereas for MZ1-3, no SP anomaly could be identified. This was most likely suppressed by the strong SP anomaly 6, which is very close to the magnetic anomaly. From the geoelectric profile 2, resistivities around 100 Ωm and IP values up to 45 mrad can be correlated with the magnetic anomalies. After Horo et al. (2020) and Han et al. (2016), resistivities lower than 100 Ωm and SP values of around -90 mV are common for sulfidic mineralizations. After Eppelbaum (2021), SP values of sulfidic and polymetallic deposits range between -60 and -500 mV, whereas -500 mV is rarely observed for SP values of ore origin and indicates a larger deposit. Due to the defined geometry, a large deposit can be excluded as the source of the high SP values with up to -500 mV. Therefore, it will be assumed that beside pyrrhotite, intercalations of graphite are present, which cause the partly high potential drops. This will be supported due to the location of the anomalies, which are close to the graphitic anomalies from group A.

Group C

In this group magnetic and low SP responses could be observed. Anomalies from magnetic zone 2 and SP anomalies 7 to 10 belong to this group. Since the anomalies occur in both, the Weitzbauer and the Pramerkogel formation, and the steep alignment of the anomalies, a vein character can be assumed. This is also supported by field observations, where small mineralizations could be identified in the taken samples. North of anomaly 10, a geoelectric profile was conducted during the geophysical field workshop in April 2022. Enhanced IP values and resistivities below 400 Ωm could be measured at this location. Graphite as the reason for the anomalies can be excluded due to the resistivity values, but also due to the magnetic behavior of the anomalies. In addition, in sampling points 1 and 2, which are also in the north of the anomalies, pyrrhotite was found to be the main magnetic component. For sampling point 1, hematite was also found as a second magnetic component. The enhanced IP values can therefore be related to the pyrite, which is in association with pyrrhotite, what can be seen as the source of the magnetic and SP anomalies. In difference to group B anomalies, which are also based on pyrrhotite, higher resistivities and lower SP values could be observed. This is because of the smaller geometry but also due to the different character of the mineralizations. While in Group B, magnetic minerals are distributed in the whole sample, here the mineralizations are concentrated in a small area and surrounded by quartz, what could explain the higher resistivities. Even if the association between arsenopyrite and pyrite is more common, after Bojar et al. (1998), pyrrhotite can also be associated with arsenopyrite. Since some anomalies are close to, or in the Pramerkogel formation, where arsenopyrite is known, a possible relation cannot be excluded.

Group D

SP anomalies 11 to 13 belong to this group, where only for anomalies 11 and 12 ERT and IP data is available. Due to the similar behavior in SP and magnetic and due to the spatial closeness, anomaly 13 can also be listed in this group. Comparing the general measured SP values with the literature, a graphite body as the main driver of the anomalies is not very likely, because a higher potential drop can be expected. Even if the SP values depend on the size and depth of the anomalous bodies, a body with an expansion of 20 m and an overburden of only a few meters, which is the case for anomaly 11, would result in much higher SP values. Anomaly 12 is in greater depths what would explain low SP values, but the resistivities are above 100 Ωm, what contrasts with resistivity values for a graphitic body from literature. Furthermore, the anomalies are in the greenschist, where graphite is only present in small intercalations of black shale. In addition, the steep orientation of the anomalous bodies seen in the IP data speaks against a stratiform mineralization, what can be expected for graphite. Nevertheless, some graphite intercalations, especially in the south, where the SP values reach -500 mV are likely. This can also be seen in the resistivity data of profile 1, which shows partly values below 10 Ωm for anomaly 11. Profiles of the Geophysical field workshops are crossing these anomalies in the north and in the south. In all profiles low resistivities and an enhanced polarization values can be observed for anomaly 11. For anomaly 12 the polarization effects are not that strong, but indications for enhanced phase angles are present and again the resistivities are low.

Geochemical data taken in the north of anomaly 11 and 12 during the field workshop indicate that at the location of both anomalies enhanced arsenic and sulfur concentrations are present. In addition, also in the south of the anomalies, enhanced sulfur and arsenic concentrations but also enhanced gold concentration with around 15 ppb could be determined in soil samples taken by Brunner in 2023. By also concerning the closeness to the gold bearing arsenopyrite mineralizations found by MINREX (1987), it is likely that this group is related to them. Due to the above-mentioned reasons, sulfidic mineralizations will be interpreted as reasons for the occurrence of the anomalies. Anomaly 11 is in close contact with the black shales of the Weitzbauer formation and can be related to the arsenopyrite mineralization which is after Bojar et al. (1998) bound to mylonite.

Group E

Magnetic zone 3 belongs to this group, which is in the Pramerkogel formation. According to the paleomagnetic measurements, maghemite could be defined as the main magnetic component with high susceptibility values. Based on geoelectric profile 1, resistivities are above 1000 Ωm and an IP effect cannot be associated with this anomaly. These values correspond to the overall values of the greenschists. Furthermore, an SP effect can also be excluded. In difference to the other groups, this group cannot be followed across the whole survey area, what can be related to the steep topography of the Pramerkogel. Due to the flat dip of the anomaly, a stratiform character is assumed.

10 Conclusion

Overall, the applied geophysical methods yielded interpretable results which can be compared well with each other. Due to the steep topography in the survey area, magnetic and self-potential data are partly strongly varying in the strength of the anomalies. As a result, the traceability of anomalies across profiles is difficult. In addition, the sometimes high vegetation leads to differences in the GPS accuracy, so that one must accept a certain offset when comparing the different methods. However, resistivities, phase angles and self-potential data usually show a high correlation. Graphite as well as sulfidic mineralizations can be characterized by low resistivities, enhanced IP values and a SP anomaly, what is also in agreement with literature. Due to the lower resistivities (1-10 Ωm) and stronger SP anomalies (-500 to -1000 mV) for graphite, these minerals could be distinguished geophysicallly. For the differentiation, if an identified sulfidic mineralization is related to pyrrhotite or arsenopyrite, the magnetic method was crucial. Using observations from the literature and additional geochemical data, a distinction between arsenopyrite and pyrite was also possible. It has been shown that all applied geophysical methods were needed to describe the origin of the anomalies and therefore how important it is to also combine them. Furthermore, the availability of geochemical data is a major advantage for defining the sources of anomalies. Since the polarization measurements seem to be good applicable to define the overburden and extension in the depth of mineralizations, further investigations should be aimed. Especially along the boundary between the Pramerkogel and Weitzbauer formation, more profiles would better define the gold bearing arsenopyrite mineralization. Due to the comparison of the IP measurements conducted with different frequencies and electrodes, a general increase of the IP effect by reducing the measurement frequency was observed. This leads to the assumption that the presented phase angles are slightly underestimated. Possible following IP measurements should take this into account. The areal SP measurements delivered important results about the spatial extension of the mineralizations. While in the northern profiles, a clear connection between the profiles can be seen, in the southern profiles a high number of anomalies occur in short distances and not all of them could be related to the other profiles. A reduction of the SP line spacing to 50 m in the southern part of the survey area should give additional information on the relationship between the profiles.

11 References

Antes G. 1998: Geochemische und Geophysikalische Anomalies im Bereich des Arsenkies-Goldvorkommens Strassegg,Steiermark (Die „Straßeger Anomalie“). Unveröff. Diss., Formal-und Naturwiss. Fak. Univ. Wien, Wien, 92 pp.

Barrett D. & Dentith M. 2003: Geophysical exploration for graphite at Uley, South Australia. ASEG Extended Abstracts 3, 47-58.

Basemap, Am Straßegg, o.J. 2023,15. January. https:/www.basemap.at

Bojar H.P., Bojar A.V., Mogessie A., Fritz H. & Thalhammer O.A.R. 2001: Evolution of veins and sub-economic ore at Strassegg, Paleozoic of Graz, Eastern Alps, Austria: evidence for local fluid transport during metamorphism. Chemical Geology 175, 757–777.

Bojar H.P., Mogessie A. & Thalhammer O. 1998: Die Mineralogie und Genese der Elektrum Arsenopyrit Vererzung am Straßegg, Breitenau am Hochlantsch/Gasen (Steiermark, Österreich). Mitteilung naturwissenschaftlicher Verein Steiermark 128, 57-76.

Butler R.F.,1992: Paleomagnetism: Magnetic Domains to Geologic Terranes. Blackwell Sciences Inc., Boston, 319 pp.

Czermak F. & Schadler J. 1933: Vorkommen des Elementes Arsen in den Ostalpen. Mineralogische und Petrographische Mitteilungen 44, 1-67.

Dentith M. & Mudge S.T. 2014: Geophysics for the Mineral Exploration Geoscientist, Cambridge University Press, Cambridge, 438 pp.

Ebner F., Fritz H. & Hubmann B. 2001: Das Grazer Paläozoikum: Ein Überblick. Ber. Inst. Geol. Paläont. K.F.Univ. Graz, Band 3, Graz, 25 pp.

Ebner F. & Rantitsch G. 2000: Das Gosaubecken von Kainach-ein Überblick. Mitt.Ges. Geol. Bergbaustud.Österr. 44, 157-172.

Ebner F., Hubmann B. & Weber L. 2000: Die Rannach- und Schöckel-Decke des Grazer Paleozoikums. Mitt.Ges. Geol. Bergbaustud.Österr. 44, 1-44.

Eppelbaum L.V. 2021: Review of Processing and Interpretation of Self-Potential Anomalies: Transfer of Methodologies Developed in Magnetic Prospecting. Geosciences 11, 194.

Fritz H., Ebner F. & Neubauer F. 1992: The Graz thrust complex (Paleozoic of Graz). Alpaca field guide, KFU Graz, 83–92.

Fritz H. & Neubauer F. 1988: Geodynamic aspects of the Silurian and Early Devonian Sedimentation in the Paleozoic of Graz (Eastern Alps). Schweizer Mineralogische und Petrographische Mitteilungen 68/3, 359-367.

Flügel H.W. & Hubmann B. 2000: Das Paläozoikum von Graz: Stratigraphie und Bibliographie.- Schriftenreihe der Erdwissenschaftlichen Kommissionen 13, Verlag der Österreichischen Akademie der Wissenschaften, Wien, 118 pp

Gautneb H., Ronning J.S., Engvik A.K., Henderson I.H.C., Larsen B.E., Solberg J.K., Ofstad F., Gellein J., Elvebakk H. & Davidsen B. 2020: The Graphite Occurences of Northern Norway, a Review of Geology, Geophysics, and Resources. Minerals 10, 626.

Gasser D., Stüwe K. & Fritz H. 2010: Internal structural geometry of the Paleozoic of Graz. Int. J. Earth. Sci. 99, 1067–1081.

GIS Steiermark, Am Straßegg, o.J. 2023, 06.March. https:/www.gis.stmk.gv.at

Gsellmann H. 1987: Zur Geologie am Nordostrand des Grazer Paläozoikum (im Bereich Hochschlag — Plankogel — Heilbrunn). (unveröff.) Diss. naturwiss. Fak. Univ. Graz, Graz, 202 pp.

GSM-19 v7.0 Instruction Manual. Manual release 7.4 March 2008, GEM Systems Inc.,149pp. 2022, 14. October. https:/gemsys.ca

Han M.H., Shin S.W., Park S., Cho S.J. & Kim J.H. 2016: Induced polarization imaging applied to exploration for low-sulfidation epithermal Au–Ag deposits, Seongsan mineralized district, South Korea. Journal of Geophysics and Engineering 13, 817-823.

Hasenhüttl C. & Russegger B. 1992: Niedriggradige Metamorphose im Grazer Paläozoikum. Jb. Geol. Bundesanst. 135, Heft 1, 287- 297.

Heritiana A., Riva R., Rajaomahefasoa R., Razafiarisera R. & Razafindrakoto B. 2019: Evaluation of flake graphite ore using self-potential (SP), electrical resistivity tomography (ERT) and induced polarization (IP) methods in east coast of Madagascar. Journal of Applied Geophysics 169, 134-141.

Horo D., Pal S.K. & Singh S. 2020: Mapping of Gold Mineralization in Ichadih, North Singhbhum Mobile Belt, India Using Electrical Resistivity Tomography and Self-Potential Methods. Mining, Metallurgy & Exploration 38, 397–411.

Hubmann B. 1993: Ablagerungsraum, Mikrofazies und Paläoökologie der Barrandeikalk-Formation (Eifelium) des Grazer Paläozoikums. Jb. Geol. Bundesanst. 136/2, 393-461.

Jalete A. 1997: Application of Integrated Geophysical Methods for Graphite Exploration in Gara-Gedemsa Area, South Ethiopa. Unpublished M.Sc Thesis, Addis-Ababa University, Ethiopia, 86pp.

Knödel K., Krummel H. & Lange G. 1997: Handbuch zur Erkundung des Untergrundes von Deponien und Altlasten, Band 3. Springer Verlag, Berlin Heidelberg,1102 pp

Kruiver P.P., Dekkers M.J. & Heslop D. 2001: Quantification of magnetic coercivity components by the analysis of acquisition curves of isothermal remanent magnetization. Earth Planet. Sci.Lett. 189, 269–276.

Krenn K., Fritz H. & Mogessi A. 2007: Late Cretaceous exhumation history of an extensional extruding wedge (Graz Paleozoic Nappe Complex, Austria). Int. J. Earth. Sci. 97,1331-1352.

Madhusudan I.C., Tapojyoti P. & Balaram D. 1990: Geophysical surveys for the Sargipalli graphite, Sambalpur, Orissa. Indian Minerals 44, 325–334.

Meschik P.M. 2016: Untersuchung der Eigenpotentialvariationen im Gebiet Arzberg-Haufenreith. Unveröff. Bachelorarbeit, Montanuniversität Leoben,42pp.

MINEREX Mineral Explorationsgesellschaft m.b.H. 1987: Statusbericht - Projekt: Gold-Straßegg Berichtszeitraum VII-XII/1986 (unveröff.), 13 pp.

Modl D., Grundmann G. & Bojar H.P. 2022: Der Arsenbergbau Zuckenhut/Straßegg (Breitenau/Gasen, Steiermark, Österreich) – Archäologische und mineralogische Untersuchungen zur Herstellung von künstlichen Arsensulfiden. res montanarum 62, 107-123.

Neubauer F. 1981: Untersuchungen zur Geologie, Tektonik und Metamorphose des „Angerkristallins" und des E-Randes des Grazer Paläozoikums. Jahresbericht 1980, Hochschulschwerpunkt S 15, 2, 114-121.

Park J.O., You Y.J. & Kim J.H. 2009: Electrical resistivity surveys for gold-bearing veins in the Yongjang mine, Korea. Journal of Geophysics and Engineering 6, 73-81.

Ronning J. S., Gautneb H., Larsen B. E., Knezevic J., Baranwal V., Elvebakk H., Gellein J., Ofstad F. & Bronner M. 2017: Geophysical and geological investigations of graphite occurrences in Vesterålen and Lofoten, Northern NGU rapport 2018.011.

Sato M. & Mooney H.M. 1960: The electrochemical mechanism of sulfide self-potentials. Geophysics 25, 226–249.

Seiberl W. 1993: Aerogeophysikalische Vermessung im Bereich Birkfeld. Unveröff.Ber. Wien (Geol. B.-A.), pp 61.

Stoll J.B. & Gurk M. 2014: GEOPHYSIKALISCHE UNTERSUCHUNGEN IN DER STEIERMARK/ÖSTERREICH „PLETTENKAR-PROJEKT“, Abschlussbericht (unveröff.), 33 pp.

Tauxe L. 2005: Inclination flattening and the geocentric axial dipole hypothesis. Earth Planet. Sci. Lett. 233, 247-261.

Weber F., Schmid C., Aigner H. & Mayer R. 1984: Bericht über die geophysikalische Prospektion in Pusterwald/Plättenkar. Literaturarchiv Geologisch-Mineralogischer Landesdienst Steiermark 183,1-16.

Weber L. 1990: Die Blei-Zinkerzlagerstätten des Grazer Paläozoikums und ihr geologischer Rahmen. Archiv für Lagerstättenforschung der geologischen Bundesanstalt 12, Vienna ,289 pp.

ZAMG online declination Inclination calculator. o.J. 2023,15. Feburary. https://www.zamg.ac.at

12 List of Figures

13 List of Tables

14 Appendix

A1: Inversion parameter

Restoring inversion parameters from file C:\Users\biedermann\Documents\ERT\CounInterval\Final_Inversion_Wenner.ivp.
Initial damping factor is 0.1500.
Minimum damping factor is 0.0200.
Local optimization is not used.
Convergence limit is 5.0000.
Minimum change in RMS error is 0.5000.
Number of iterations is 6.
Vertical to horizontal flatness filter ratio is 1.0000.
User defined increase in layer thickness.
Number of nodes between adjacent electrodes is 4.
Smoothness constrain is only used directly on model resistivity values.
Number of topographical data points is not reduced.
Topographical modeling is to be carried out.
End-to-end linear topographical trend to be removed.
Jacobian matrix is recalculated after each iteration.
Increase of damping factor with depth is 1.0500.
Finite element method with damped grid is used for topographic modeling.
Robust data inversion constrain is used with cutoff factor 0.0500.
Robust model inversion constrain is used with cutoff factor 0.0050.
Extended model is not used.
Effect of side blocks is slightly reduced.
Normal mesh is used.
Damping factor is optimised at each iteration.
Blocky constraint is used in time-lapse inversion.
Thickness of first layer is 0.5000.
Factor to increase thickness layer with depth is 1.1000.
Finite element method is used
Width of blocks used is 1 times the unit electrode spacing
All models blocks must have the same width
RMS convergence limit is 0.1 percent
Logarithm of apparent resistivity values are used for the inversion
Resistivity/IP data are inverted concurrently
Do not proceed automatically in sequential IP inversion
IP damping factor is 0.2500
Automatic IP damping factor is not used
Cutoff factor for borehole data is 0.00010
Standard cross-borehole model is used.
Upper resistivity cutoff limit is 50.00000
Lower resistivity cutoff limit is 0.02000
Average resistivity used.
Model refinement used.
Incomplete Gauss-Newton method used with convergence limit of 0.0050
Reference model with damping factor of 0.010 used.
Factor to increase model depth range is 1.050.
Borehole damping not used
Limit range of data weights from error estimates not used.
Different data weights from error estimates used for different time series.
Model resolution not calculated.
L curve method not used
Different norms used in L curve method.
Damping factor allowed to increase in L curve method.
Borehole damping using horizontal distance from nearest borehole
Fast Jacobian calculation for dense data sets not used.
Higher damping factors at sides are used.
Damping factors are adjusted for distances between blocks in model.
Length of segment in sparse inversion method is 250 electrodes.
Time-lapse damping factor is 0.25.
Time-lapse damping factor is reduced after each iteration.

A2: IP Comparison with different frequencies and electrodes at the beginning of profile 2.

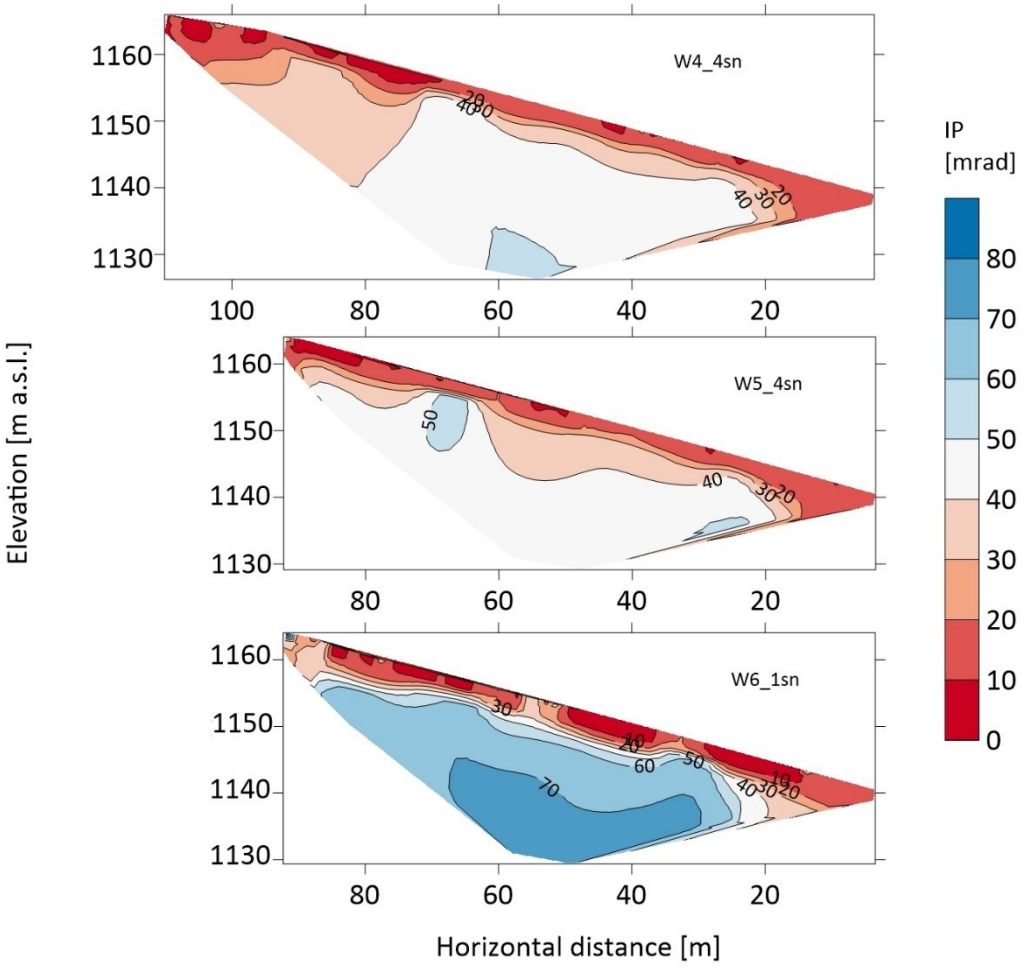

A3: Geoelectric Profile fw_03 (GGÜ October 2022) with the corresponding magnetic and SP values.

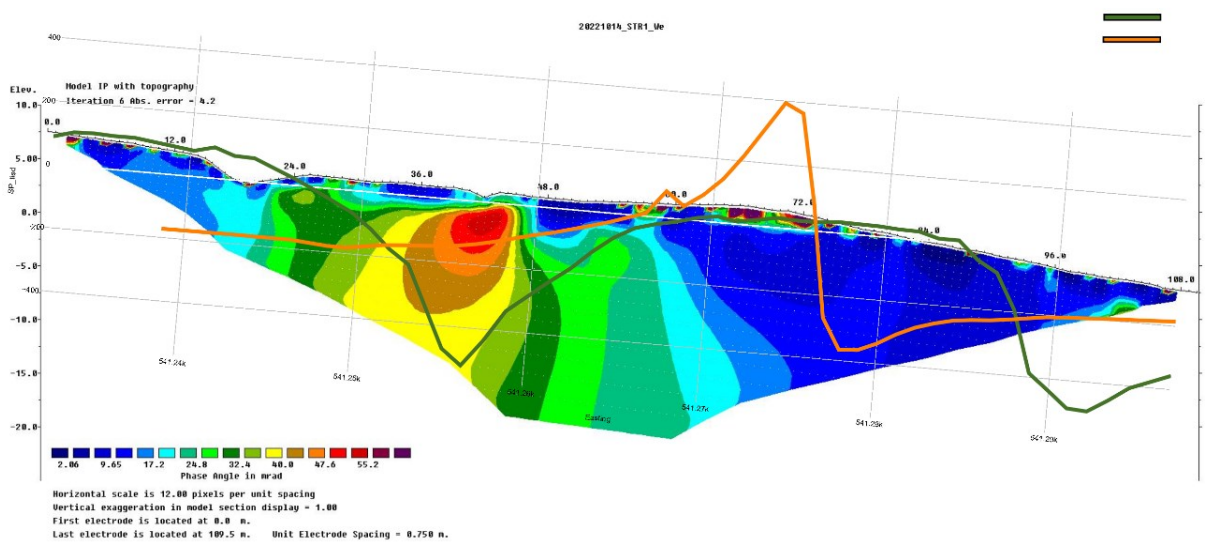

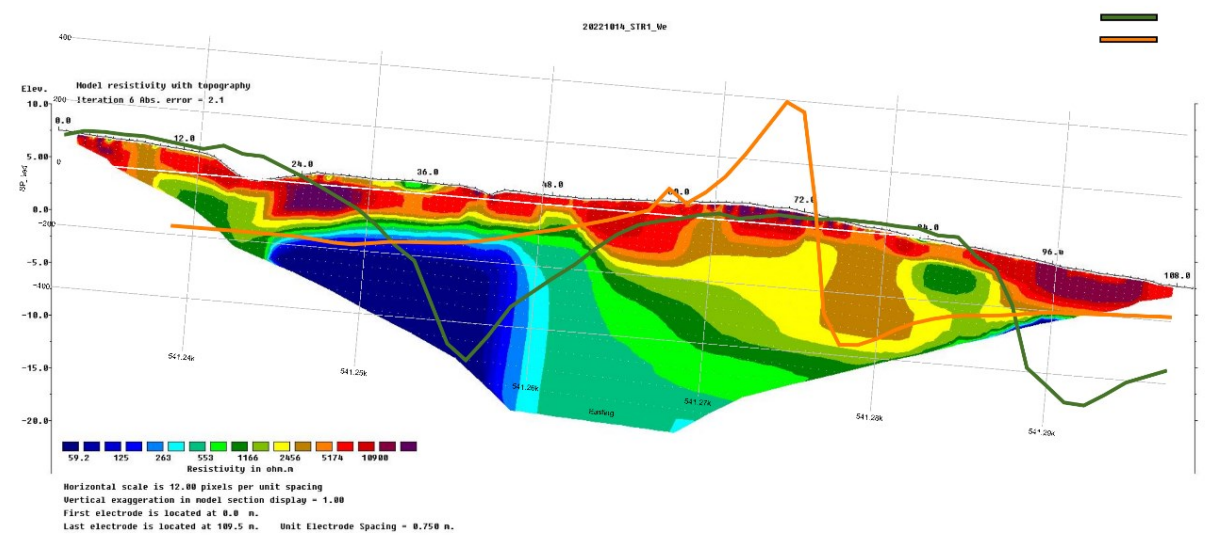

A4: Geoelectric profile fw_01 (GGFW April 2022) with the corresponding magnetic and SP values.

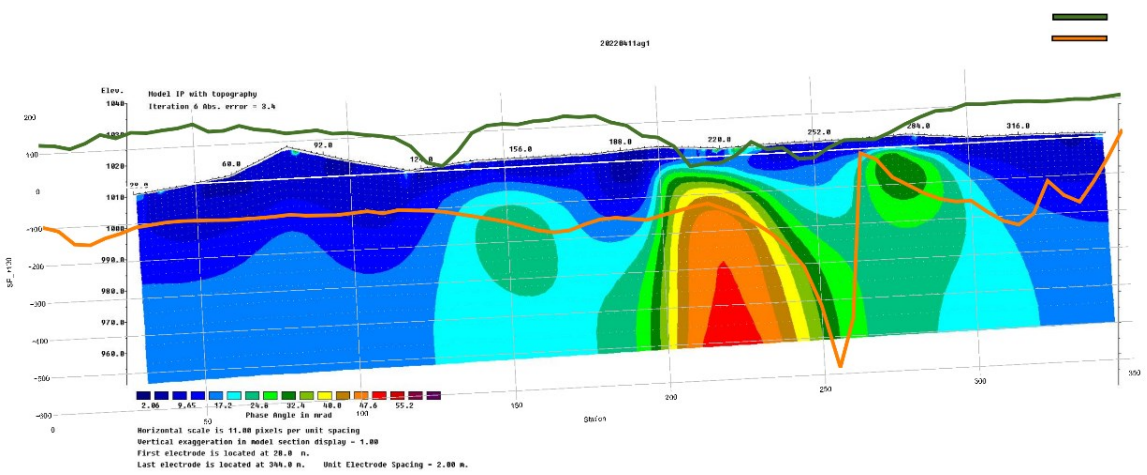

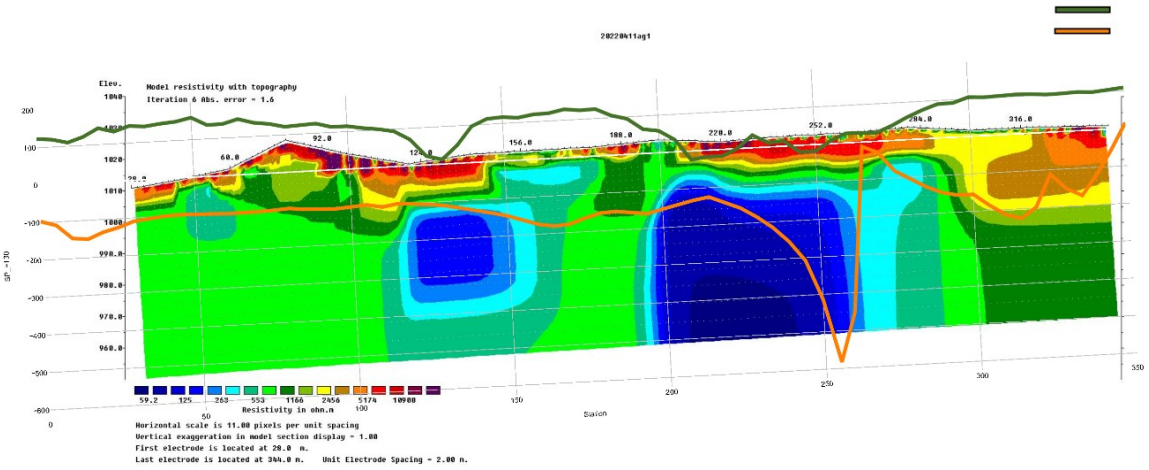

B1: Table of the measured susceptibility values and magnitude of the natural remanence for each specimen.

Sample point	Sample	Specimen	Bulk susceptibility [SI]	NRM magnitude [A/m]
SP01	P08	P08_1	0.000138521	-
		P08_2	0.000210017	0.00645
		P08_3	5.6434E-05	0.0062
		P08_4	0.000320083	0.0066
		P08_5	0.000156845	0.0066
SP02	P05	P05_1	0.008008965	0.244
		P05_2	0.007572	0.192
		P05_3	0.005972612	0.317
		P05_4	0.005910428	0.146
	P06	P06_1	0.000226147	0.0564
		P06_2	0.00105436	0.185

		P06_3	0.00135149	0.052
		P06_4	0.016805047	0.659
		P06_5	0.007367063	0.593
		P06_6	0.000714796	0.283
		P06_8	0.000392087	0.0916
		P06_9	0.000381096	0.0567
		P06_10	0.002082758	0.3358
		P06_11	0.001181989	0.048
		P06_12	0.000591331	0.119
	P11	P11_1	0.022073594	-
		P11_2	0.002373481	0.305
		P11_3	0.057658094	0.49
		P11_4	0.000347826	0.04
		P11_5	0.001444206	1.13
		P11_6	0.033208919	-
		P11_7	0.002891336	0.16
		P11_8	0.000316934	0.0051
		P11_9	0.000370993	0.11
		P11_10	-4.46794E-06	0.0075
		P11_11	0.00187612	0.495
	P16	P16_1	0.000135197	0.0125
		P16_2	0.000277551	0.0084
		P16_3	0.000221048	0.015
		P16_4	0.001328329	0.58
		P16_5	6.4952E-05	0.0086
		P16_6	-1.33877E-05	0.00009
		P16_7	0.000199853	0.0097
		P16_8	0.002795528	0.099
SP03	P09	P09_1	0.000170182	0.00093
		P09_2	7.48147E-05	0.00202
		P09_3	5.49331E-05	0.00467
		P09_4	0.000113008	0.00666
	P14	P14_1	0.000300342	0.00186
		P14_2	0.000263995	-
		P14_3	7.26529E-05	-
		P14_4	**0.000237014**	0.00104
		P14_5	0.000326541	0.00133
SP04	P10	P10_1	0.00136053	0.02
		P10_2	0.00617439	0.154
		P10_3	0.003889808	0.1887
		P10_4	0.007450594	0.128
		P10_5	0.001151548	-
		P10_6	0.00403191	0.187
		P10_7	0.003870055	
	P13	P13_1	0.002580185	0.057

		P13_2	0.005827686	0.383
		P13_3	0.007928051	0.947
SP05	P01	P01_1	0.081293853	1.73
		P01_2	0.132345609	1.027
		P01_3	0.107102691	0.425
		P01_4	0.193259655	0.803
		P01_5	0.141620575	0.74
		P01_6	0.210417627	0.637
		P01_7	0.174895	0.654
	P02	P02_1	0.116901109	0.8428
		P02_2	0.112268207	0.4163
		P02_3	0.093428813	0.4703
		P02_4	0.074195583	0.704
		P02_5	0.103955776	0.588
		P02_6	0.191897428	0.6566
		P02_7	0.176248198	-
	P03	P03_2	0.085973751	0.872
		P03_3	0.065572321	0.9278
		P03_4	0.12934053	1.638
		P03_5	0.152633172	1.178
		P03_6	0.166899708	1.21
		P03_7	0.073176564	0.887
		P03_8	0.06989026	0.871
		P03_9	0.078499155	1.045
		P03_10	0.063397034	0.294
		P03_11	0.069346693	0.695
		P03_12	0.074518505	0.776
		P03_13	0.064146586	0.6023
	P04	P04_1	0.085360836	3.153
		P04_2	0.092382426	2.665
		P04_3	0.10159422	2.305
		P04_4	0.125794043	2.19
		P04_5	0.105806624	3.72
		P04_6	0.107954082	3.33
		P04_7	0.102020686	2.97
SP06	P12	P12_1	0.000192674	0.00056
		P12_2	0.000652894	0.00159
		P12_3	0.000880727	0.0003
		P12_4	0.000388179	0.00038
		P12_5	0.000686322	0.00027
		P12_6	0.00035497	0.00027
		P12_7	0.000664829	0.00049

C1: Table of the modelled bodies in potent.

Id	Type	X	Y	Z	Strike	Dip	Plunge	Susc	A	B	C	Slope
		m	m	m	deg	deg	deg	SI	m	m	m	deg
1	RectPrism	540309	5248161	1203	150	-60	0	0.02	20	70	20	
2	Dyke	540762.9	5248600	1029.78	170	0	0	0.015	20	80	57	74
3	RectPrism	540266	5248600	1124	150	-60	20	0.015	20	50	50	
4	RectPrism	540225.4	5248487	1060	150	0	-10	0.05	100	170	150	
5	RectPrism	540461	5248006	1176	150	-60	0	0.025	60	50	80	
6	RectPrism	540179	5248342	1214	147	-60	0	0.015	17	50	49.15	
7	RectPrism	540226.8	5248300	1215	150	-60	0	0.019	27	80	23.79	
8	RectPrism	540264.9	5248233	1215	145	-60	-1	0.013	22.73	70	50.1	
9	RectPrism	540673	5248152	1085	155	-50	0	0.02	50	50	50	
10	RectPrism	540882.3	5248257	1075	150	0	0	0.014	20	70	80	
11	RectPrism	540797.7	5248457	1035	150	0	-18	0.025	10	60	50	
12	RectPrism	540962.2	5248151	1133.47	160	0	0	0.015	20	80	100	
13	RectPrism	541320.7	5247847	1077	150	-65	0	0.1	10	50	80	
14	RectPrism	541077	5247943	1112	160	0	1	0.023	5.76	30	61.17	
15	RectPrism	541276	5247946	1065	150	-50	-2	0.1	7	71	30	
16	Dyke	540719	5248598	1041	140	-20	0	0.014	17	50	57	90
17	RectPrism	540559	5248594	1087	150	-10	0	0.017	30	50	50	
18	RectPrism	540857.2	5248456	1054	155	0	-10	0.025	10	60	100	
19	RectPrism	540622	5248251	1069	150	-60	0	0.009	30	75	50	
20	RectPrism	540356.9	5248605	1124.81	150	-60	0	0.022	25	50	50	
21	RectPrism	540475	5248584	1099	160	-60	0	0.02	50	100	50	
22	RectPrism	541100.1	5248150	1121	150	-8	0	0.014	50	50	100	
23	RectPrism	540416.6	5248591	1106.32	160	-60	0	0.02	50	100	50	
24	RectPrism	540798	5248400	1030.9	150	0	0	0.016	30	50	100	
25	RectPrism	541165.4	5248150	1106	150	0	0	0.013	20	80	100	
26	RectPrism	540762.6	5248551	1018.96	-31	20	0	0.02	17	40	49.99	
27	RectPrism	541154.1	5248209	1123	150	0	0	0.013	25	80	100	
28	Dyke	540669.4	5248572	1067	160	-30	0	0.012	19.91	100	56.01	90
29	RectPrism	541086	5248202	1127	150	0	0	0.01	20	50	100	
30	RectPrism	540915	5248145	1129	150	0	0	0.015	40	50	100	
31	RectPrism	540918	5248099	1127	150	-10	0	0.02	20	70	100	
32	RectPrism	540727	5248102	1081	144	-30	0	0.024	50	100	50	
33	RectPrism	540368	5248198	1188	150	-50	0	-0.023	10	70	50	
34	RectPrism	540451.1	5248219	1096	160	-50	0	0.016	80	110	50	
35	RectPrism	540645	5248197	1094	160	-53	0	0.024	18	50	50	
36	Dyke	540304	5248505	1178	150	-60	0	0.022	17	50	57	91
37	RectPrism	540388	5248452	1166	150	-60	0	0.02	30	60	50	
38	RectPrism	540640.2	5248465	1085.07	145	-25	0	0.018	18	120	51	
39	RectPrism	540686.2	5248465	1064	150	-30	0	0.022	5	120	51	
40	RectPrism	540677	5247952	1131	150	-60	0	0.02	60	60	50	
41	RectPrism	540408.2	5248142	1145	150	-60	0	0.017	10	50	50	
42	RectPrism	540783.6	5248348	1025	150	0	0	0.015	20	60	100	
43	RectPrism	541047	5247950	1122	150	-20	0	0.019	18	70	60	
44	RectPrism	540444	5247955	1226	150	-60	-6	0.025	27	60	67	
45	RectPrism	540565	5247902	1212	150	-60	0	0.016	20	50	100	
46	RectPrism	540628	5247897	1181	150	-60	0	0.014	60	60	60	
48	RectPrism	540790.4	5247908	1177	150	-60	0	0.023	50	60	60	
50	RectPrism	540912	5248199	1104	145	0	0	0.01	20	60	100	
51	RectPrism	541315	5247900	1094	145	-53	0	0.07	10	50	60	
52	RectPrism	541248	5247900	1051	150	-60	0	0.073	20	97	60	
54	RectPrism	540394	5248312	1150	150	-50	0	0.015	50	75	50	
55	RectPrism	540558	5248300	1089	155	-50	0	0.02	28	80	50	
56	RectPrism	541059.1	5248299	1117	150	0	0	0.013	20	80	100	
57	RectPrism	540619.4	5248001	1147	150	-70	0	0.025	10	50	60	
58	RectPrism	540651	5248001	1144	140	-60	0	0.022	12	50	60	
59	RectPrism	540965	5248000	1143	150	-60	0	0.02	25	66	60	
60	RectPrism	541006	5248000	1143	156	-20	0	0.025	30	53	50	
61	Dyke	541233	5248000	1059	146	-60	0	0.09	5	66	50	120
62	RectPrism	541104	5248049	1118	150	-10	0	0.021	30	50	60	
63	RectPrism	540857.2	5248497	1050.08	160	0	0	0.02	10	60	50	
64	RectPrism	540975	5248049	1156.16	150	0	0	0.025	10	70	60	
65	RectPrism	540894	5248050	1157	150	-46	0	0.027	30	70	60	
66	RectPrism	540741.2	5248499	1020.08	150	0	0	0.02	10	60	100	
67	RectPrism	540857.8	5247994	1060	150	0	-10	0.05	150	130	60	
68	RectPrism	541207.6	5248049	1082	154	-50	0	0.1	5	55	50	
69	RectPrism	540497	5248040	1146	150	-50	0	0.02	50	100	60	
70	RectPrism	540366	5248040	1205	150	60	0	0.02	20	109	50	
71	RectPrism	540871.6	5247905	1201	150	-50	0	0.02	10	50	70	
72	Dyke	541196	5248100	1071	150	-50	0	0.09	10	47	60	70
73	RectPrism	541090	5248100	1121	150	-20	0	0.02	35	50	60	
75	RectPrism	540991.4	5248100	1135.89	150	0	0	0.02	10	50	60	
76	RectPrism	540848.2	5248100	1104	160	-60	0	0.021	35	60	60	
77	RectPrism	540396.4	5248008	1080	159	0	-10	0.05	130	350	200	
79	RectPrism	540742	5248279	1065	143	0	-9	0.013	15	160	100	
80	RectPrism	540231	5248556	1140	149	-60	0	0.012	10	50	50	
84	RectPrism	541103.3	5248249	1138.77	150	0	0	0.01	20	60	100	
85	RectPrism	541000	5247912	1120	150	-60	0	0.028	20	80	50	
86	RectPrism	540521	5248350	1090	160	-50	0	0.021	50	70	50	
87	RectPrism	540934.4	5248318	1072.58	155	0	0	0.023	20	120	100	
88	RectPrism	540516	5248420	1095	160	-60	0	0.018	60	100	50	
89	RectPrism	540862	5248399	1057	150	0	0	0.027	30	75	100	
91	RectPrism	540912	5248402	1077.6	150	0	0	0.018	20	50	100	
92	RectPrism	540356	5248394	1148	150	-60	10	0.017	70	80	50	
94	RectPrism	541027.8	5248101	1132	150	-10	0	0.02	16	50	50	

C2: Profiles of the reduced total magnetic intensity (TMI) and the gradient (z). Observed data is marked in blue and the calculated data according to the modelled bodies in POTENT in red.

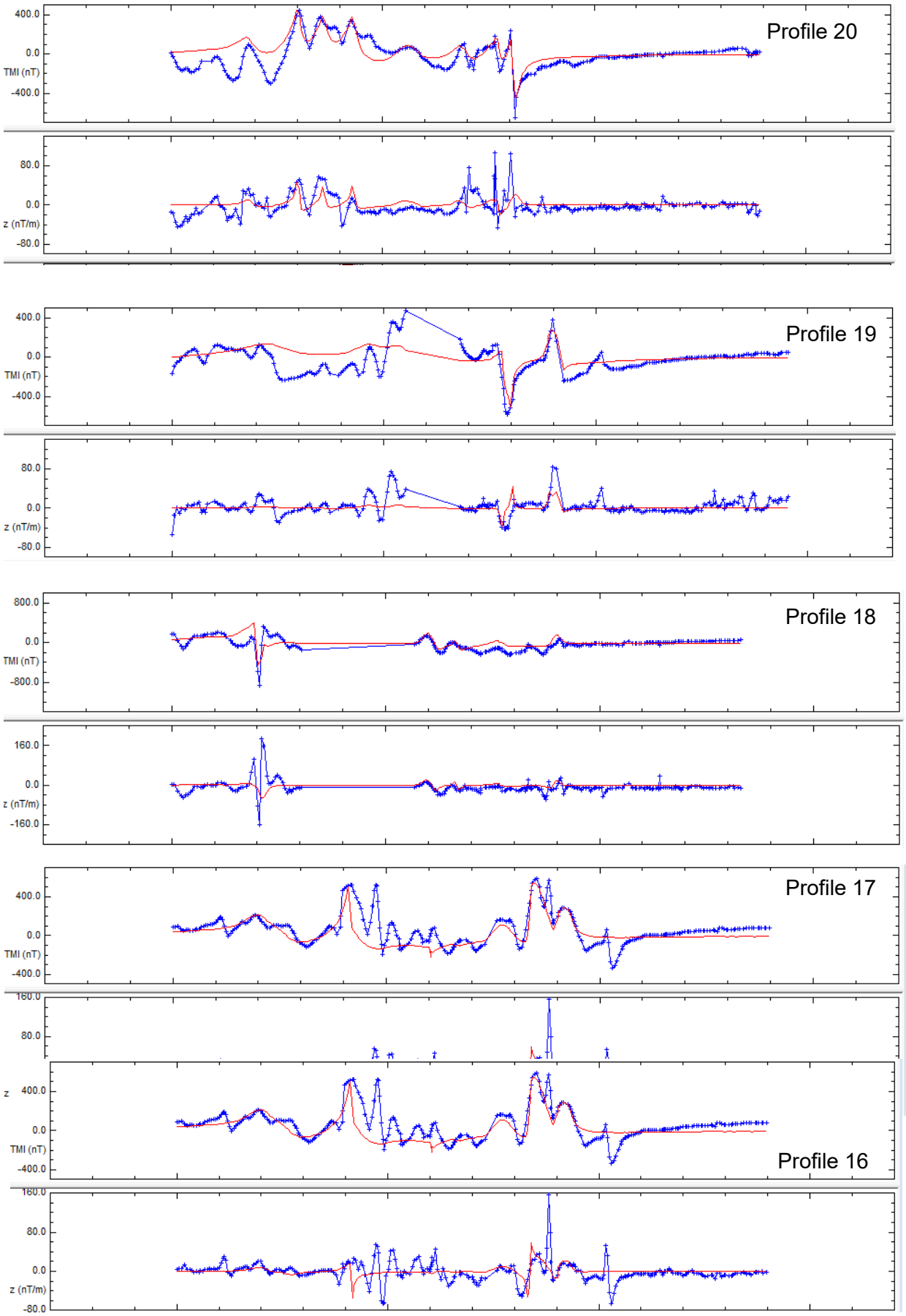

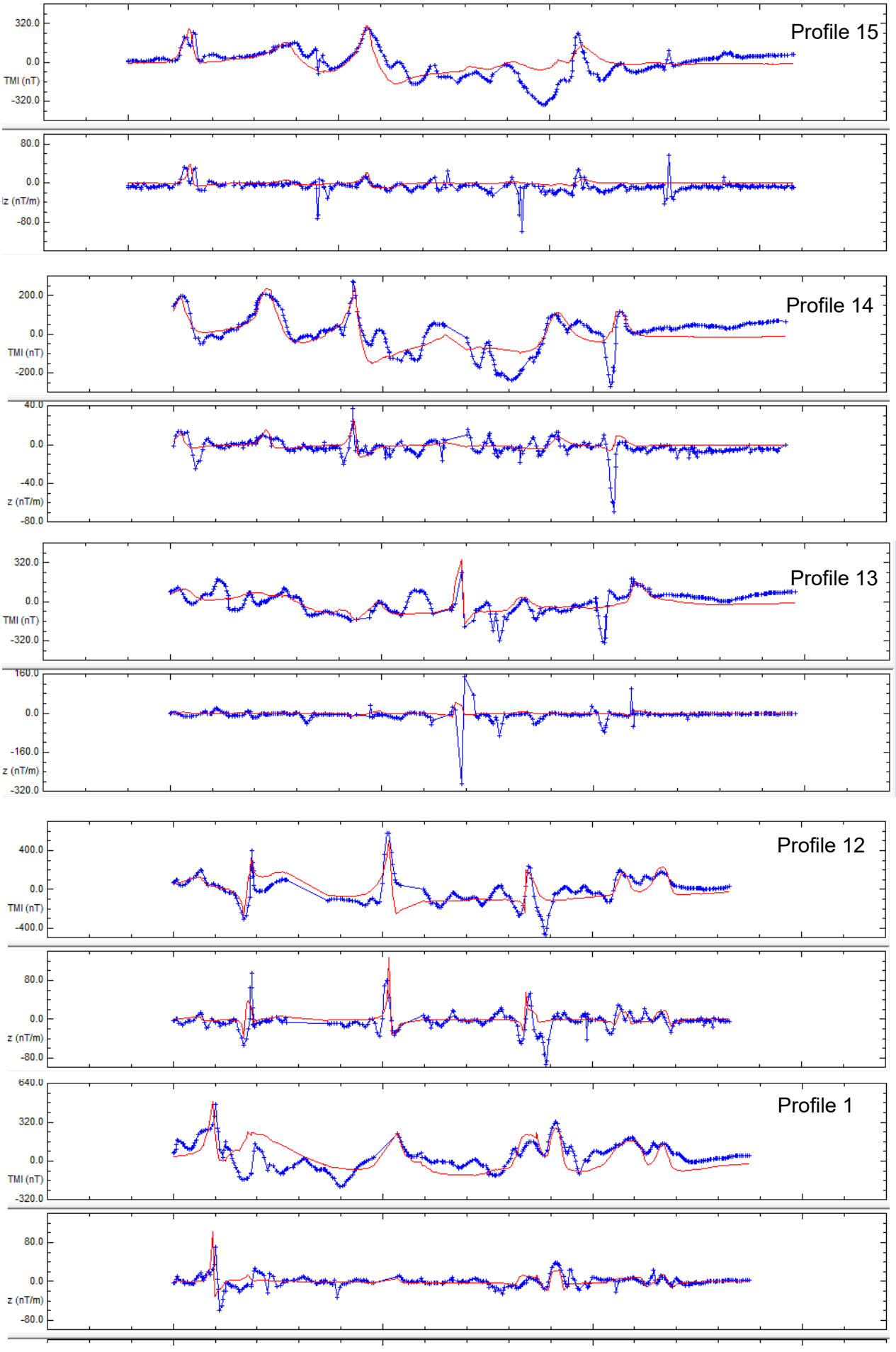
Profile 15
320.0
0.0
TMI (nT)
-320.0
80.0
0.0
z (nT/m)
-80.0
Profile 14
200.0
0.0
TMI (nT)
-200.0
40.0
0.0
-40.0
z (nT/m)
-80.0
Profile 13
320.0
0.0
TMI (nT)
-320.0
160.0
0.0
-160.0
z (nT/m)
-320.0
Profile 12
400.0
0.0
TMI (nT)
-400.0
80.0
0.0
z (nT/m)
-80.0
Profile 1
320.0
0.0
TMI (nT)
-320.0
80.0
0.0
z (nT/m)
-80.0

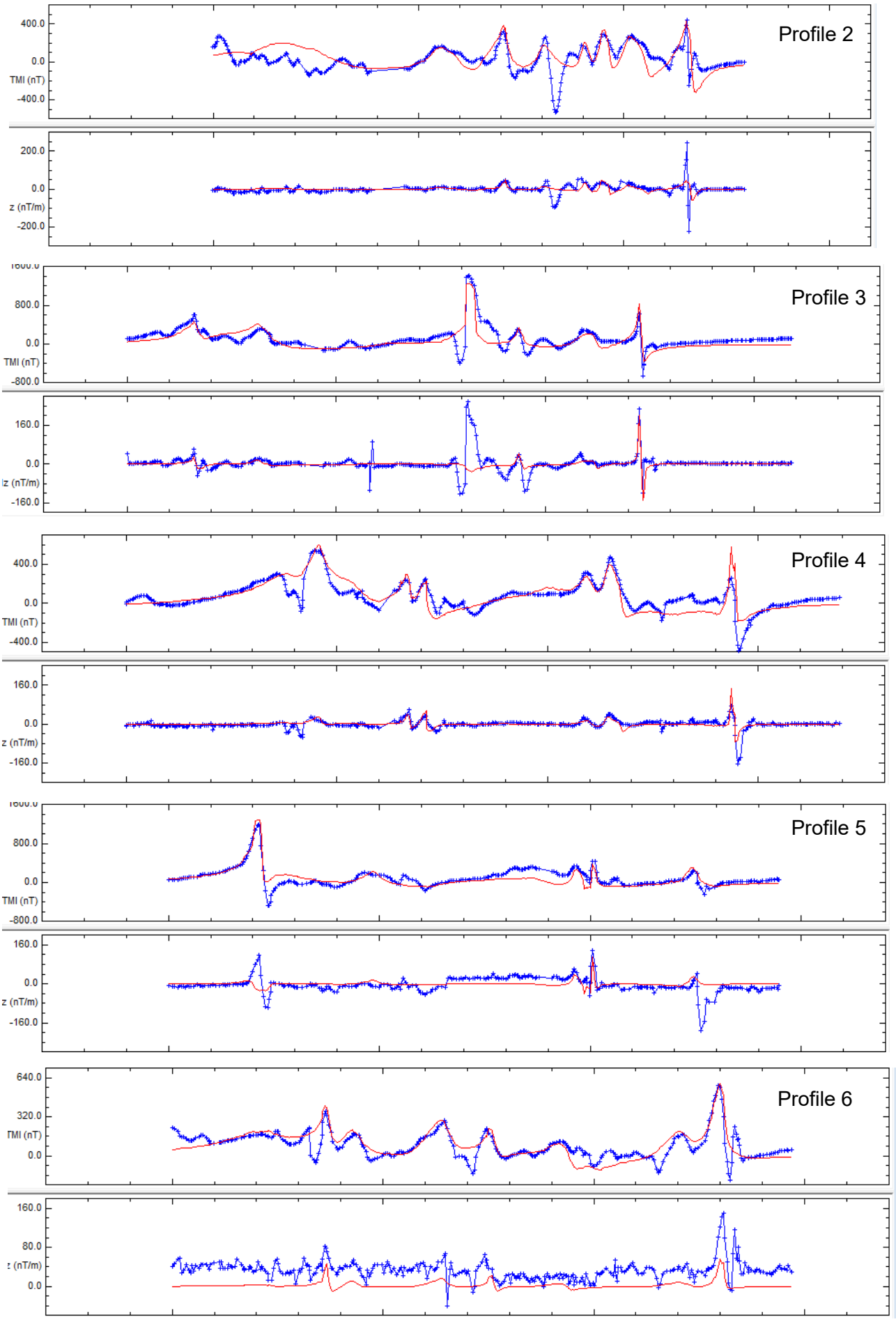
Profile 2
400.0
0.0
TMI (nT)
-400.0
200.0
0.0
z (nT/m)
-200.0
Profile 3
800.0
0.0
TMI (nT)
-800.0
160.0
0.0
z (nT/m)
-160.0
Profile 4
400.0
0.0
TMI (nT)
-400.0
160.0
0.0
z (nT/m)
-160.0
Profile 5
800.0
0.0
TMI (nT)
-800.0
160.0
0.0
z (nT/m)
-160.0
Profile 6
640.0
320.0
TMI (nT)
0.0
160.0
80.0
z (nT/m)
0.0

15 Electronic Appendix

The electronic Appendix is in the folder “Masterarbeit_Biedermann_Appendix”.

Subfolders:

“ Geochemistry”: contains an excel sheet of the analyzed soil samples in the area around the Pramerkogel.

“Kappameter”: contains an excel sheet of the measured susceptibility values along the trenches.

“ProcData”: contains already processed data files from geoelectric, laboratory, magnetic and SP measurements.

“RawData”: contains the raw data of the carried-out measurements.